AN ABSTRACT OF THE THESIS OF

Stephen D. Pierce for the degree of Doctor of Philosophy in Oceanography presented on May 6, 1998. Title: Equatorward Jets and Poleward Undercurrents Along the Eastern Boundary of the Mid-Latitude North Pacific.

Abstract approved: _____

Robert L. Smith

We sharpen our view of an eastern boundary current region during the upwelling season through the analysis of several data sets. We focus on the mesoscale flow field off of northern California, observed during the Coastal Transition Zone (CTZ) experiment of 1988. First, we estimate tidal currents in the region by least-squares harmonic analysis of both shipboard acoustic Doppler current profiler (ADCP) and moored data. The tide is predominantly M_2 and varies from 1-4 cm/s across the region, consistent with previous tidal studies. Next, we use detided ADCP together with conductivity-temperature-depth data to infer absolute geostrophic velocities during each of the five surveys in July-August 1988. Referencing geostrophy with the ADCP reveals a stronger equatorward jet than previously reported; southward volume transport from 0-500 m through a 200 km onshore-offshore line is as high as $8.0 \times 10^6 m^3 s^{-1}$, with a mean over the five surveys of $6.3 \pm 1.3 \times 10^6 m^3 s^{-1}$. The jet was about 50 km wide, with core velocities > 0.6 m/s. During a two-week period in July 1988, horizontal velocity shears were sufficient to shift the effective local inertial frequency 10% higher on the cold (inshore) side and 5% lower on the warm (offshore) side of the jet. Observed near-inertial currents have amplified energy in the region with lower effective inertial frequency, consistent with theoretical predictions. Next, the basic instability mechanism leading to a meandering CTZ jet is analyzed using a linear quasi-geostrophic model applied to observed basic state velocity profiles. The jet is subject to

both barotropic and baroclinic instability processes, and meander wavelengths of 260-265 km are the fastest growing. Growth periods of 7-11 days and along-jet phase speeds of 4-8 km/d are predicted. Finally, the poleward undercurrent which was observed during the 1988 CTZ experiment is also investigated with a series of shipboard ADCP sections collected from 33-51°N during July-August 1995. Subsurface poleward flow occurred in 91% of the sections, with a mean undercurrent core velocity of 17±1 cm/s and transport in a 140-325 m layer of $0.9\pm0.1\times10^{6}m^{3}s^{-1}$. One portion of the undercurrent is continuous over a 440 km length.

Equatorward Jets and Poleward Undercurrents Along the Eastern Boundary of the Mid-Latitude North Pacific

by

Stephen D. Pierce

A THESIS

submitted to

Oregon State University

in partial fulfillment of
the requirements for the
degree of

Doctor of Philosophy

Presented 6 May 1998
Commencement June 1998

Doctor of Philosophy thesis of Stephen D. Pierce presented on May 6, 1998

APPROVED:

Major professor, representing Oceanography

Dean of the College of Oceanic and Atmospheric Sciences

Dean of Graduate School

I understand that my thesis will become part of the permanent collection of Oregon State University libraries. My signature below authorizes release of my thesis to any reader upon request.

Stephen D. Pierce, author

Acknowledgments

I thank Bob Smith for his support, advice, and enthusiasm. Thank you also to committee members Jane Huyer, Mike Kosro, and Murray Levine. Special thanks to Jack Barth for support and encouragement during the quasi-research associate phase of my career, and thanks to John Allen for inspiration and collaboration on Chapter 5. Thank you to the Office of Naval Research and the National Science Foundation for support.

Friends and colleagues too numerous to mention have helped me in various ways. A small sampling: Fred Bahr, Lisa Brown, Karen Casciotti, Lee Christie, Tim Cowles, Irma Delson, Richard Dewey, Jane Fleischbein, Jeff Gonor, David Gow, Leon Gunther, Peter Morse, Sarah Myslis, Priscilla Newberger, Arthur Pike, Henry Pittock, Dennis Root, Leslie Rosenfeld, Tina Saal, Rich Schramm, Kipp Shearman, Libby Smith, Karen Snyder, Rachel Somerville, Pam Stevens, Bob Still, Andy VanBrocklin, Betsy Vicksell, Leonard Walstad, Lorene Wapotich, Chris Wilson, Donna Witter, and Sarah Zimmermann. I thank countless Beanery employees for good coffee. Thank you to the officers and crews of the R/V *Wecoma*, R/V *Pt. Sur*, R/V *Miller Freeman*, and other research vessels. Thanks to Dan Kelley for offering the excellent *gri* graphics software freely to the world. I am grateful to the members of the OSU-Corvallis symphony for the pleasure of making both joyful and sorrowful noises with them over the years.

Thank you to my family and especially my parents Alice and Norton Pierce. Thanks to Biko and Luff for their unwavering canine love, loyalty, and devotion. And most of all thank you to my spouse/spice and partner-in-mischief Anne Minnich.

Contribution of authors

For Chapter 5 (Pierce *et al.*, 1991), coauthor Walstad provided the objectively analyzed velocity sections from the 1987 CTZ experiment, which I then analyzed for instability. Coauthor Allen provided expert supervision and close scrutiny of the formulations. Both coauthors provided editing of the text.

For Chapter 6 (a submitted publication), coauthors Smith, Kosro, Barth, and Wilson all provided data sets and editing of the text.

Table of contents

Table of contents (continued)

Table of contents (continued)

List of figures

List of figures (continued)

List of figures (continued)

List of tables

Equatorward Jets and Poleward Undercurrents Along the Eastern Boundary of the Mid-Latitude North Pacific

I. General introduction

The mesoscale flow fields of oceanic eastern boundary current regions are complex, with significant time-dependence and spatial structure (Wooster and Reid, 1963). Although the California Current system has been the best-observed and most studied of all eastern boundary current regions, many kinematic and dynamic issues remain unresolved. One outstanding question involves the nature of the jets or filaments which are frequently seen in satellite imagery in the region just offshore of the continental shelf, the coastal transition zone. During the upwelling season, the coastal transition zone separates relatively warm offshore water from cool freshly upwelled water. Satellite sea-surface temperature has shown tongues of cool water extending offshore across this zone (Bernstein *et al.*, 1977; Flament *et al.*, 1985; Ikeda and Emery, 1984). Mesoscale surveys of the region have confirmed that the cold tongues are associated with narrow and intense currents (Rienecker *et al.*, 1985; Kosro and Huyer, 1986; Rienecker and Mooers, 1989). To better understand these features in a region off of northern California, the Coastal Transition Zone (CTZ) program was launched in the late 1980s by the Office of Naval Research (Brink and Cowles, 1991).

The 1987 CTZ field program was designed to study the seasonal occurrence of jets in the region from about 37−42°N and 60−150 km offshore. Four physical/biological surveys were conducted in February, March, May, and June 1987. The results show a dramatic seasonal change (Kosro *et al.*, 1991). During the winter surveys, no obvious jets or coherent flow patterns were present. The spring surveys however show a strong, meandering, equatorward jet with significant volume transport (2-3 $\times 10^6 m^3 s^{-1}$). The jet forms along the boundary between

freshly upwelled cooler and more saline water inshore and warmer and fresher water offshore.

The CTZ program continued in 1988 with five successive surveys from mid-June to early August, in a region from 37−39°N and 200 km offshore. These mesoscale grids observed an evolving coastal transition zone jet over 3 months during the summer upwelling season (Huyer *et al.*, 1991). The 1988 experiment also included an array of 3 current meter moorings which effectively captured time-series of the jet core velocity.

The set of initial results from the CTZ program is contained in a special issue of the *Journal of Geophysical Research*; Brink and Cowles (1991) provide a good introduction to the set of papers and overview of the findings. The present study builds directly upon these results.

In Chapter II, we investigate tidal currents in the CTZ region off northern California. We apply least-squares harmonic analysis to estimate tidal currents from both historical current meter data and the CTZ 1988 current meter and shipboard acoustic Doppler current profiler (ADCP) data. The tide is dominated by the semi-diurnal $M2$ constituent, which contains 83% of the tidal variance. The $M2$ tidal ellipses have semi-major axes which vary from 1-4 cm/s across the region, largest over the continental slope. The tidal component of the flow field has the potential to contaminate our view of the subtidal CTZ jet; part of the motivation for this study is to remove the tidal part of the flow from our measurements.

In Chapter III, we build upon the initial presentation of the hydrographic and shipboard ADCP data from the five 1988 surveys found in Huyer *et al.* (1991). We estimate absolutely referenced geostrophic currents throughout the three-dimensional volume enclosed by each survey grid, by combining detided shipboard ADCP and hydrographic data and assuming quasi-geostrophy and mass conservation. The combination of ADCP and CTD data sharpens our view of the strong equatorward velocity jet, breaking the constraint of any level-of-no-motion assumption. The jet volume transport is larger than previously reported, with as much as 8.0

$\times 10^6 m^3 s^{-1}$ equatorward transport from 0-500 m. We also derive vertical velocity *w* assuming no cross-isopycnal flow, and we observe 10-20 m/d *w* in patches of 20-30 km size, consistent with previous isolated observations and modeling studies.

In Chapter IV, we focus on near-inertial oscillations within the CTZ jet, as measured by the moored current meter array. Near-inertial amplitudes are about 15 cm/s close to the surface and 5 cm/s at 450 m depth. We find enhancement of near-inertial energy along the warm flank of the jet, where the effective inertial frequency is shifted down by 5%.

Chapter V (Pierce *et al.*, 1991) explores the basic instability process of a CTZ jet in detail. The tendency for such a jet to develop a meander and become unstable is investigated using a six-layer linear quasi-geostrophic model. We obtain observed velocity profiles from the 1987 CTZ experiment and test them for both barotropic and baroclinic instability. Along-jet wavelengths of 260-265 km are found to be the most unstable, and barotropic and baroclinic instability processes are both important.

Finally, Chapter VI (submitted publication) describes some more recent ADCP observations of another prominent mesoscale feature seen during the CTZ study: the poleward undercurrent over the continental slope. These July-August 1995 observations are unusually extensive, a series of sections across the shelf break from 33-51°N at about 18 km meridional spacing, and they complement the intensive CTZ experiment within the smaller 37-39°N region. Subsurface poleward flow occurred in 91% of the sections, with a mean undercurrent core velocity of 17±1 cm/s and transport in a 140-325 m layer of $0.9 \pm 0.1 \times 10^6 m^3 s^{-1}$. These data confirm the ubiquity of the poleward undercurrent along the eastern boundary of the mid-latitude north Pacific. Besides being important aspects of eastern boundary current systems, the continuity and significant transports which we observe imply that poleward undercurrents may be important oceanic features in a global circulation context.

REFERENCES

Bernstein, R. L., L. Breaker, and R. Whritner, 1977: California Current eddy formation: ship, air and satellite results. *Science*, **195**, 353-359.

Brink, K. H. and T. J. Cowles, 1991: The coastal transition zone program. *J. Geophys. Res.*, **96**, 14637-14647.

Flament, P., L. Armi, and L. Washburn, 1985: The evolving structure of an upwelling filament. *J. Geophys. Res.*, **90**, 11765-11778.

Huyer, A., P. M. Kosro, J. Fleischbein, S. R. Ramp, T. Stanton, L. Washburn, F. P. Chavez, T. J. Cowles, S. D. Pierce, and R. L. Smith, 1991: Currents and water masses of the coastal transition zone off northern California, June to August 1988. *J. Geophys. Res.*, **96**, 14809-14831.

Ikeda, M. and W. J. Emery, 1984: Satellite observations and modeling of meanders in the California Current system off Oregon and northern California. *J. Phys. Oceanogr.*, **14**, 1434-1450.

Kosro, P. M. and A. Huyer, 1986: CTD and velocity surveys of seaward jets off northern California., July 1981 and 1982. *J. Geophys. Res.*, **91**, 7680-7690.

Kosro, P. M., A. Huyer, S. R. Ramp, R. L. Smith, F. P. Chavez, T. J. Cowles, M. R. Abbott, P. T. Strub, R. T. Barber, P. Jessen, and L. F. Small, 1991: The structure of the transition zone between coastal waters and the open ocean off northern California, winter and spring 1987. *J. Geophys. Res.*, **96**, 14707-14730.

Pierce, S. D., J. S. Allen, and L. J. Walstad, 1991: Dynamics of the coastal transition zone jet: 1. linear stability analysis. *J. Geophys. Res.*, **96**, 14979-14993.

Rienecker, M. M., C. N. K. Mooers, D. E. Hagan, and A. R. Robinson, 1985: A cool anomaly off northern California: an investigation using IR imagery and in situ data. *J. Geophys. Res.*, **90**, 4807-4818.

Rienecker, M. M. and C. N. K. Mooers, 1989: Mesoscale eddies, jets, and fronts off Point Arena, California, July 1986. *J. Geophys. Res.*, **94**, C9, 12555-12569.

Wooster, W. S. and J. L. Reid, 1963: Eastern boundary currents, in *The Sea*, ed. M. N. Hill, **2**, 253-280, Interscience Publishers, New York.

II. Tidal currents off northern California

II.1 Abstract

We estimate barotropic tidal currents in a region off northern California using an empirical model fit to a combination of moored current meter and shipboard acoustic Doppler current profiler (ADCP) measurements. The data set includes regional historical current meter records from the last few decades as well as the 1988 Coastal Transition Zone experiment moorings and shipboard ADCP. A least-squares harmonic method is applied, where the tidal parameters are fit in time and also allowed to vary spatially through polynomial surface trend interpolation. Both the relatively accurate current meter data at scattered locations and the less accurate shipboard data with wide spatial coverage are important to the solution. The tide is dominated by the M_2 constituent, which contains 83% of the tidal variance. The M_2 tidal ellipses have semi-major axes which vary from 1-4 cm/s across the region, largest over the continental slope. Ellipse orientation is roughly alongshore, rotation counter-clockwise, and poleward phase speed is 130 ± 30 ms^{-1}, consistent with previous coarser studies.

II.2 Introduction

Although tidal elevations are well-measured along the coast off northern California, direct observations of tidal currents are relatively sparse, particularly offshore of the continental shelf. Even where current meters have been deployed, estimates of tidal ellipse parameters have not always been made, since the primary interest of the field study was usually the subtidal signal.

Tidal currents offshore have been inferred using sea level and bottom pressure measurements and models of how the tide propagates along the coast. Munk *et al.* (1970) modeled diurnal and semi-diurnal barotropic tides in a large region off California as a combination of Kelvin, Poincare, and forced coastal waves. They fit the unknown amplitudes and phases of the free waves to coastal sea level and an offshore pressure record. They predicted poleward propagation of the tide and located an amphidrome in the northeast Pacific at about 135°E, 27°N. Diurnal currents were found to be about 1 cm/s and the semi-diurnal about 2 cm/s, with ellipses oriented approximately alongshore. Various global numerical tide models have roughly reproduced the features of Munk *et al.* (1970), and Irish *et al.* (1971) provided a few deep-sea pressure and current measurements which confirmed the model.

Battisti and Clarke (1982) provided a relatively straightforward improved method of estimating barotropic tidal currents in the vicinity of the coast, given sea level data. They developed a first-order analytic model to explain how a barotropic Kelvin wave is modified by varying bottom topography in the direction normal to the coast and by friction on the continental shelf; the latter is only significant for wide shelves. In a coordinate system with the y-axis alongshore, the onshore u velocity tends to be proportional to x/H and the alongshore v component proportional to xf/H, where x is distance to the coast, f is the Coriolis parameter, and H is the local bottom depth. They apply the method to predict M_2 tidal currents along the coast from 33-45°N and up to 300 km offshore. They find good agreement with current meter

observations, with comparisons made at two sites close to San Diego and one site off of Oregon.

The results of the Coastal Ocean Dynamics Experiment (CODE) include two studies, the first ones to focus on tidal analysis of current meter observations in the region off of Northern California. Noble *et al.* (1987) analyze records at four locations seaward of the shelf break, and Rosenfeld and Beardsley (1987) focus on the shelf (Figure II.1). Noble *et al.* (1987) find that the slope and basin tidal currents are mostly M_2, with semi-major axes 2-4 cm/s. The axes tend to be aligned with the local topography. They find reasonable agreement with the Battisti and Clarke (1982) prediction, supporting the assumption that the M_2 tide travels predominantly as a barotropic Kelvin wave. Rosenfeld and Beardsley (1987) obtain similar results in general, but

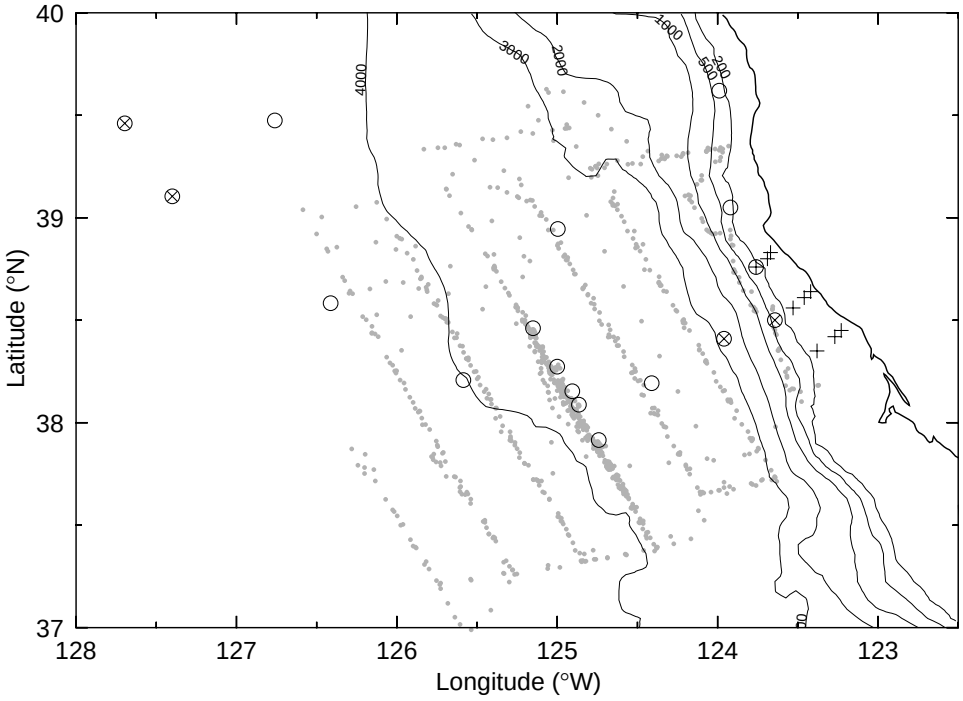

Fig. II.1 Current meter moorings used by Rosenfeld and Beardsley (+), Noble *et al.* (X), and the present study (O). Small gray dots are locations of hourly shipboard ADCP during CTZ 1988, also used in the present study. See Table II.1 for data set details. Bottom topography in meters.

also find significant alongshore variations in the size of the barotropic M_2 tidal current. These variations are attributed to small capes along the coast which can cause perturbations in the Kelvin wave amplitude. The perturbations decay offshore with a length scale similar to the alongshore size of the bump in the coastline.

The present study is to some degree a sequel to Noble *et al.* (1987), which was based on a sparser data set. We estimate the barotropic tide with additional historical current meter records as well as data from the 1988 Coastal Transition Zone (CTZ) experiment. We also use a different method; rather than analyze moorings separately and make comparisons, we use a least-squares harmonic method where all data are included in a single calculation.

The method fits to the tidal frequencies in time and to a polynomial surface in space, with a normalization which tends to favor a Battisti and Clarke (1982) type solution. This is a minor variation on the method of Candela *et al.* (1992). We find the Candela method to be effective and flexible, in that time series data collected from a platform which moves in space, such as shipboard ADCP, can be readily included within an analysis of fixed current meter data.

Part of the motivation for estimating tidal currents in this region is for the subsequent subtraction of the tide from the shipboard ADCP. Chapter III of the thesis makes use of this detided ADCP for referencing geostrophic calculations. The detiding will help sharpen our view of the subtidal mesoscale jet velocity structure.

II.3 Data

We gather together historical data from different years and even decades (Table II.1) and convert to a common time base, time increment (hourly), and spatial grid. It is a good assumption that any long-period variations in the tidal signal are extremely small compared to the M_2

Table II.1 Data sets

Name	Location	Instrument depths(m)	Time Period	Data source
LLWOD-10	127.70W 39.46N	150,615,1250,3000,3800	23-Sep-82 to 1-Sep-83	[1]
LLWOD-11	127.70W 39.46N	200,600,1250,3800,4200	5-Sep-83 to 27-Dec-83	[1]
LLWOD-6	126.76W 39.48N	2930,3750,4140	5-Sep-81 to 9-Jul-82	[1]
LLWOD-7	126.41W 38.58N	2950,3740,4260	3-Sep-81 to 23-Sep-82	[1]
LLWOD-3	127.40W 39.11N	2910,3800,4200	27-Jun-80 to 13-Mar-81	[1]
LLWOD-8	127.40W 39.11N	3000	4-Sep-81 to 21-Sep-82	[1]
OPTOMA M-1	125.00W 38.95N	175,375,1220,3250	27-Sep-84 to 11-Feb-85	[2]
OPTOMA M-2	124.41W 38.19N	145,340,800,1190,3560	3-Oct-84 to 12-Jul-85	[2]
OPTOMA M-3	125.59W 38.21N	350,800,1185,3810	28-Sep-84 to 8-Mar-85	[2]
OBS III	124.91W 38.15N	3902	24-May-66 to 6-Jul-66	[3]
RR(USGS)	123.96W 38.41N	1931	18-Sep-80 to 12-Oct-81	[4]
NCCCS C4	123.64W 38.50N	300	29-May-88 to 6-Sep-88	[5]
NCCCS V4	123.99W 39.62N	300	29-May-88 11-Sep-88	[5]
CODE2 N4	123.99W 38.51N	10,20,35,55,70,90,110,121	25-Mar-82 to 20-Aug-82	[6]
CODE2 I4	123.99W 38.51N	10,20,53	11-Mar-82 to 5-Aug-82	[6]
CTZ D4/5	125.15W 38.46N	785	26-Jun-88 to 27-Jul-88	[7]
CTZ D5/6	125.00W 38.27N	447	26-Jun-88 to 27-Jul-88	[7]
CTZ D6/7	124.87W 38.09N	434	26-Jun-88 to 27-Jul-88	[7]
CTZ D7/8	124.74W 37.92N	459	26-Jun-88 to 27-Jul-88	[7]
CTZ shipboard ADCP	126.59−123.37W 36.99−39.63N	100−200	20-Jun-88 to 5-Aug-88	[7]

[1] Heath *et al.* (1984), [2] Smith *et al.* (1986), [3] Fliegel and Nowroozi (1970), [4] Noble *et al.* (1987), [5] Magnell *et al.* (1991), [6] Limeburner (1985), [7] Huyer *et al.* (1991)

constituent, so we are free to combine data from different eras. Hourly raw data are used throughout.

In preparation for the tidal analysis, if a mooring has fairly good vertical sampling of the water column, we combine all available depths using trapezoidal integration Rosenfeld and Beardsley (1987). This single depth-averaged record is then used in the least-squares harmonic analysis. With sufficient resolution in the vertical and with several simplifying assumptions, theory indicates that this method should eliminate most of the internal tide signal. The OPTOMA M-2 (Table II.1) is an example of a mooring where this method should be effective at eliminating the baroclinic tide. If, however, a mooring does not sample a good portion of the water column, we take the deepest available record as being our best estimate of barotropic flow at that location. The CTZ D5/6 mooring is an example of the latter case, since the deepest available record is at 450 m but ocean depth is 3800 m.

All available shipboard ADCP from the 1988 CTZ experiment was filtered to hourly and averaged from 100−200 m. As *a priori* information for the least-squares technique, we use uncertainties of ±1 cm/s for an hourly moored current measurement and ±2 cm/s for an hourly shipboard ADCP value. These values are incorporated into the least-squares fitting method and used to help derive solution uncertainties.

II.4 Method

A least-squares harmonic method was first used in a tidal estimation problem by Horn (1960), using a room-sized computer. By now such methods applied to stationary current meter data are routine. The method represents the tide in the form:

$$u(t) = u_0 + \sum_{i=1}^{N} [b_i \cos(\omega_i t) + c_i \sin(\omega_i t)] \,, \tag{1}$$

where ω_i is the frequency of the i_{th} tidal constituent. Observed currents are then regressed onto (1) using least-squares methods to find the coefficients b_i and c_i which minimize the residuals. The other component, $v(t)$, is treated similarly. We use the 5 primary tidal constituents [$N = 5$ in (1)]: M_2, S_2, K_1, O_1, and N_2. A few runs using up to 21 constituents were tried; differences between these and the 5 constituent results were negligible.

Candela *et al.* (1992) recognized the inherent flexibility of least-squares methods when they suggested that b_i, c_i in (1) need not be constants. Tidal spatial variability can be modeled by allowing b_i, c_i to be spatially-varying functions, whose unknown coefficients are determined by regression onto the observations, as before. The specific form of the functions might reflect some dynamical knowledge of how the tidal currents vary in space, or they might be sets of arbitrary functions which will hopefully do well at fitting themselves to the spatial structure at hand. Candela *et al.* (1992) successfully use a combination of these two approaches, since they make use of arbitrary polynomials and splines but they also normalize by $1/H$, where $H(x, y)$ is a local bottom depth. This normalization is appropriate in the shallow East China Sea and Amazon Basin (they also estimate the subtidal mean background flow, small in their case, by simultaneous least-squares fitting to spatial functions with no time dependence; we do not attempt this since it is inappropriate for our region).

We take a similar approach but normalize u by x_c/H and v by $x_c f/H$, where x_c is the x-distance from the observation to the coast and the y-axis points towards 330°T, approximately alongshore. The Battisti and Clarke (1982) model solutions for u and v contain these terms as well. We are not applying the Battisti and Clarke (1982) model directly (it makes use of sea level; we only use velocity data here), but we predispose our least-squares solution to have the form predicted by their model.

The surface-fitting polynomials take the form:

$$m_1 + m_2 x + m_3 y + m_4 xy + m_5 x^2 + m_6 y^2 + \ldots \quad (2)$$

We expand b_i, c_i in these and then solve (1) for each velocity component u and v. Tidal ellipse parameters are then calculated from u, v using standard methods, e.g. Rosenfeld (1987). The number of terms of (2) which can be included and successfully determined will in general vary depending on the structure and quality of the data. We use the machinery of the singular value decomposition (SVD) to determine how many unknown terms we able to solve for (e.g. Press *et al.*, 1992). In our case, we use only the first four terms of the sequence (2) for M_2 and only the first term for the other constituents. Experimentation with adding higher degree terms led to non-physical solutions which were also difficult for the solution machinery to produce (solution was rank-deficient).

II.5 Results

The M_2 solution dominates the tidal signal, with 83% of the tidal variance. M_2 semi-major axes vary from 1−4 cm/s across the region, ellipse orientations roughly follow the bathymetry, and rotation sense is CCW, consistent with previous studies (Figure II.2). Uncertainties in the semi-major and minor axes vary from 0.2-0.4 cm/s. Other tidal constituents (no spatially varying solutions attempted) all have semi-major axes less than 1 cm/s (Table II.2).

We also find good agreement with estimates of poleward phase speed of the M_2 tide up the coast Noble *et al.* (1987). calculate a phase speed of 140 m/s from coastal sea level data; Munk *et al.* (1970) report a similar speed. We do a linear fit to our phase values at the coast (Figure II.2), weighted according to our confidence in any particular phase value, obtaining 130±29 m/s (95%). This agreement is useful as an independent check, since different data sets are involved.

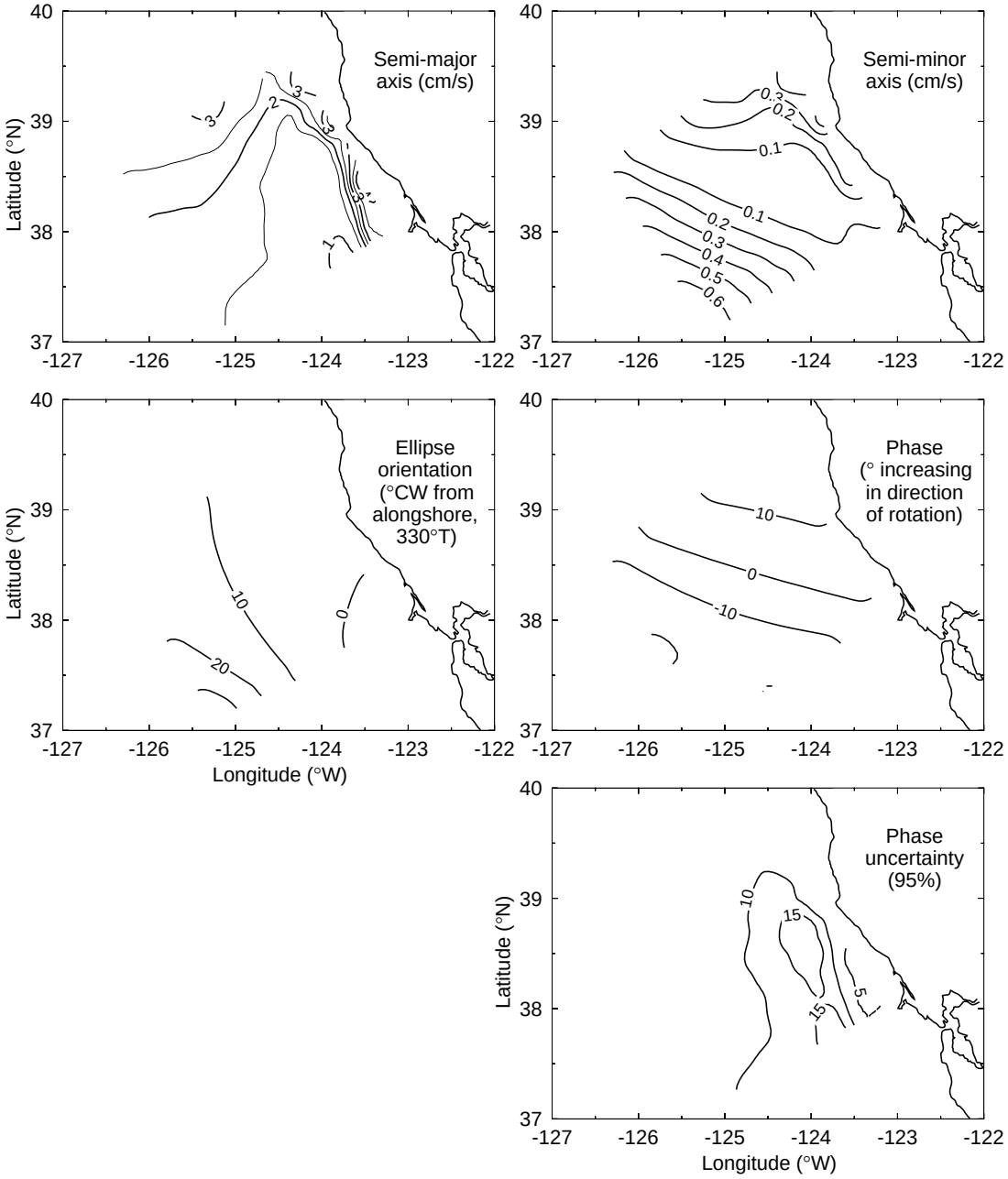

Fig. II.2 M_2 barotropic tidal ellipse parameters estimated using combined CTZ shipboard and moored data and historical moored data.

Table II.2

Name	Period (hours)	Semi-major(minor) axes(cm/s)*	Orient	Phase
S2	12.00	0.9(0.1)	5	4
K1	23.93	0.7(0.1)	34	55
O1	25.82	0.5(0.1)	33	-61
N2	12.66	0.6(0.0)	22	-1

* rotation is CCW for all constituents

We also analyzed the moored data in Table II.1 separately, applying conventional harmonic tidal analysis to each mooring. These results are the gray ones of Figure II.3, while the black ellipses are from the combined fit results using all of the data. Without exception on this figure, the obvious disagreements are at locations where good vertical resolution of the water

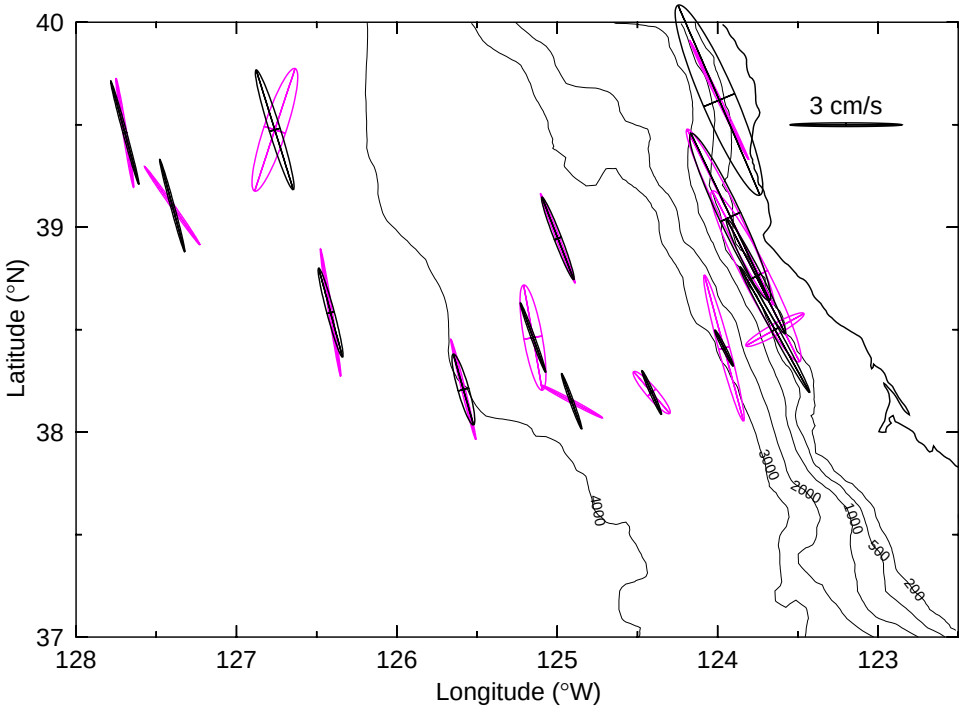

Fig. II.3. Separate harmonic M_2 tidal analysis at each mooring (gray) and combined analysis results at the mooring locations (black). Bottom topography in meters.

column was not available from the mooring. This serves as a a warning against attempts to estimate the true barotropic tidal current from a single mooring which does not have sufficient vertical resolution. The smaller differences in ellipse orientation are probably caused by inaccurate knowledge of bottom topography, since orientation tends to follow local bottom contours.

Finally, a reminder that although we have resolved the barotropic tidal currents, internal tides can be significant as well. Following removal of the barotropic solution, conventional harmonic analysis applied to the CTZ moored data, divided into five time periods of six days each, reveals an M_2 internal signal of 5-10 cm/s (Figure II.4). The complex horizontal and vertical spatial structure and time variability of the M_2 internal tide is related to the movement of strong

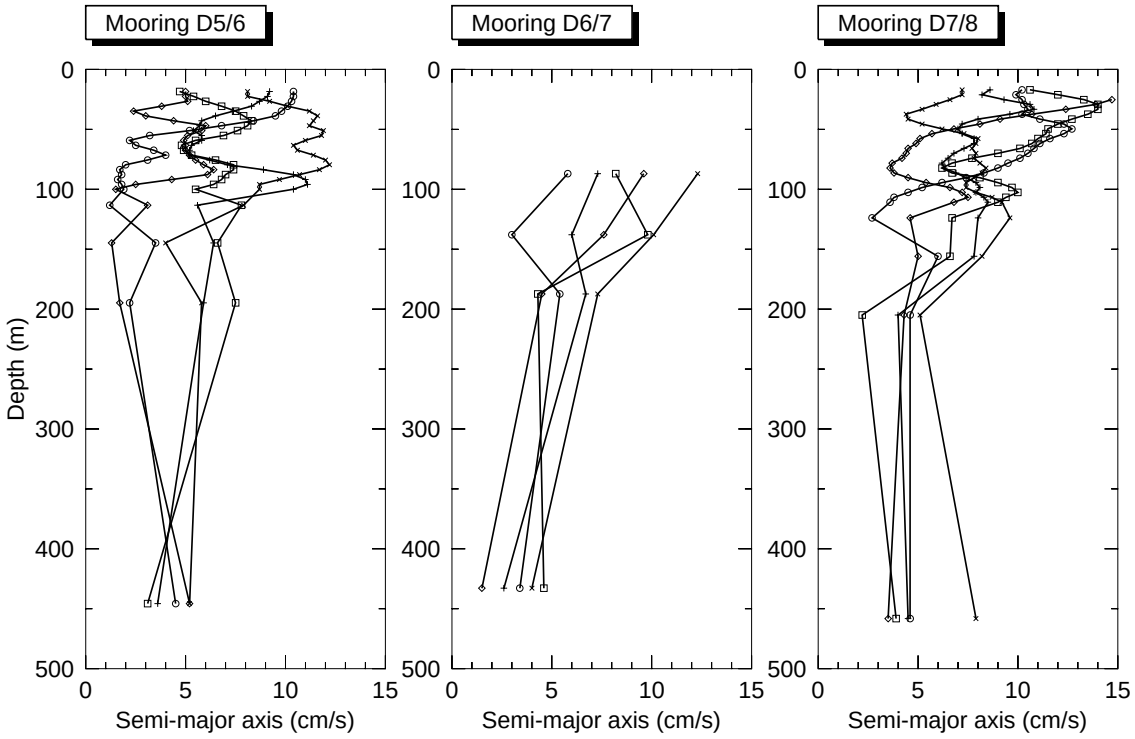

Fig. II.4. M_2 internal tide semi-major axes from least-squares harmonic analysis of the CTZ moored array, during five consecutive time periods of six days each. The estimated M_2 barotropic tide was subtracted from each record prior to analysis.

density gradients associated with the CTZ mesoscale jet, as it flows and meanders past the mooring locations. We do not have sufficient quantities of CTZ shipboard data to attempt to estimate this varying internal tide across the entire region.

II.6 Summary

We successfully estimate the barotropic tide in a region off northern California using an empirical fit to several velocity data sets, including shipboard ADCP collected during the 1988 CTZ experiment. The tide is dominated by the M_2 constituent, which contains 83% of the tidal variance. The M_2 tidal ellipses have semi-major axes which vary from 1-4 cm/s across the region, largest over the continental slope. Ellipse orientation is roughly alongshore, rotation counter-clockwise, and poleward phase speed is 130 ± 30 ms^{-1}, consistent with previous, less-detailed studies.

II.7 References

Battisti, D. S. and A. J. Clarke, 1982: A simple method for estimating barotropic tidal currents on continental margins with specific application to the M2 tide off the Atlantic and Pacific coasts of the United States. *J. Phys. Oceanogr.*, **12**, 8-16.

Candela, J., R. C. Beardsley, and R. Limeburner, 1992: Separation of tidal and subtidal currents in ship-mounted acoustic doppler current profiler observations. *J. Geophys. Res.*, **97**, 769-788.

Fliegel, M. and A. A. Nowroozi, 1970: Tides and bottom currents off the coast of northern California. *Limnol. Oceanogr.*, **15**, 615-624.

Heath, G. R., D. K. Rea, G. Ness, R. D. Pillsbury, T. M. Beasley, C. Lopez, and D. M. Talbert, 1984: Oceanographic studies supporting the assessment of deep-sea disposal of defueled decommissioned nuclear submarines. *Environ. Geol. Water Sci.*, **6**, 189-199.

Horn, W., 1960: Some recent approaches to tidal problems. *Int. Hydrogr. Rev.*, **38**, 28-105.

Huyer, A., P. M. Kosro, J. Fleischbein, S. R. Ramp, T. Stanton, L. Washburn, F. P. Chavez, T. J. Cowles, S. D. Pierce, and R. L. Smith, 1991: Currents and water masses of the coastal transition zone off northern California, June to August 1988. *J. Geophys. Res.*, **96**, 14809-14831.

Irish, J., W. Munk, and F. Snodgrass, 1971: M2 amphidrome in the northeast Pacific. *Geophys. Fluid. Dyn.*, **2**, 355-360.

Limeburner, R., (ed), 1985: Code-2: moored array and large-scale data report, WHOI Tech. Rep. 85-35, p. 234, Woods Hole Oceanographic Institution.

Magnell, B. A., C. D. Winant, N. A. Bray, C. L. Greengrove, J. F. Borchardt, J. M. Federiuk, C. E. Dorman, R. L. Bernstein, and J. Largier, 1991: Circulation on the northern California shelf and slope: final report of the northern California coastal circulation study, OCS Study MMS 91-0023, p. 543, Miner. Manage. Serv., U.S. Dept. of the Inter..

Munk, W., F. Snodgrass, and M. Wimbush, 1970: Tides offshore, transition from California coastal to deep-sea waters. *Geophys. Fluid Dyn.*, **1**, 161-235.

Noble, M., L. K. Rosenfeld, R. L. Smith, J. V. Gardner, and R. C. Beardsley, 1987: Tidal currents seaward of the northern California continental shelf. *J. Geophys. Res.*, **92**, 1733-1744.

Press, W. H., S. A. Teukolsky, W. T. Vetterling, and B. P. Flannery, 1992: *Numerical Recipes, 2nd edition,* Cambridge, Cambridge.

Rosenfeld, L. K. and R. C. Beardsley, 1987: Barotropic and semidiurnal tidal currents off northern California during the Coastal Ocean Dynamics Experiment (CODE). *J. Geophys. Res.*, 1721-1732.

Rosenfeld, L. K., 1987: Tidal Band Current Variability Over the Northern California Continental Shelf. *WHOI Tech. Report,* **87-11**.

Smith, R. L., G. Pittock, J. Fleischbein, and R. Still, 1986: Current measurements from moorings off northern California: September 1984 - July 1985, 121, p. 211, College of Oceanography - Oregon State University.

III. Absolute Geostrophic Flow in a Coastal Transition Zone

III.1 Abstract

The coastal transition zone program in July-August 1988 repeatedly sampled a region off northern California, collecting shipboard acoustic Doppler current profiler and conductivity-temperature-depth data at stations 25 km apart on alongshore sections spaced 40 km apart. After gridding the fields using objective analysis, we derive absolute referenced geostrophic flow for each survey through a two step method: least-squares fitting of depth-ranges of ADCP to the geostrophic velocity profiles, and adjustment to remove noise in the form of divergence. The resulting field is in geostrophic balance and conserves mass. The combination of ADCP and CTD data sharpens our view of the strong equatorward velocity jet, breaking the constraint of any level-of-no-motion assumption. Mean equatorward volume transport through an onshore-offshore line over the five surveys was $6.3 \pm 1.3 \times 10^6 m^3 s^{-1}$. We also derive vertical velocity *w* assuming no cross-isopycnal flow, and we observe 10-20 m/d *w* in patches of 20-30 km size, consistent with previous isolated observations and modeling studies.

III.2 Introduction

During the summer upwelling season, complex and energetic mesoscale flow fields can form in oceanic eastern boundary regions. Off northern California, within the past decade or so, several sets of observations have shown intense, meandering, equatorward-tending jets with core velocities >0.5 ms^{-1} and widths >50 km (Huyer *et al.*, 1998). One of the observational programs designed to study these features was the Coastal Transition Zone (CTZ) program of 1988. In a region from 37−39° and extending 200 km offshore, five successive surveys were undertaken from mid-June to early August (Brink and Cowles, 1991). These mesoscale surveys included continuous acoustic Doppler current profiler (ADCP) data and conductivity-temperature-depth (CTD) data at standard stations at 25(40) km spacing alongshore(offshore).

Initial results from these five standard 1988 surveys are reported by (Huyer *et al.*, 1991) and other papers in the same issue. All of the surveys showed a strong baroclinic equatorward jet with core surface velocities >0.5 ms^{-1}, decreasing to about 0.1 ms^{-1} at 200 m. The width of the jet was 50-75 km and transport relative to 500 dbar was about $4 \times 10^{6} m^{3} s^{-1}$. The jet flowed along a front separating relatively cool and recently upwelled productive water from warmer offshore water.

Although Huyer *et al.* (1991) include some geostrophic velocity calculations relative to 500 m, no study to date has combined the 1988 hydrographic and ADCP data sets to yield absolute referenced geostrophic velocities. We develop and apply a method for combining these data throughout the three-dimensional survey volume.

Walstad *et al.* (1991) used the 1987 CTZ May and June hydrographic/ADCP survey data in a quasi-geostrophic data assimilation study. They apply ADCP data at single levels to reference geostrophy, and they assimilate these fields into a quasi-geostrophic model of a portion of the 1987 grid. One of their important results is that inclusion of the ADCP data helps reveal the

true nature and vertical extent of the CTZ jet; at 500 m a clear jet signature of about 0.2 ms^{-1} exists. The success of the Walstad *et al.* (1991) study helps motivate the present work with the 1988 data set.

In a different region, off southern California, Chereskin and Trunnell (1996) have also combined hydrographic and ADCP survey data to determine absolute quasi-geostrophic streamfunction. They also find substantial departures from a 500 m lnm. Other examples of combining hydrographic and shipboard ADCP data to estimate absolute geostrophic fields in a three-dimensional survey region include Pollard and Regier (1992), Allen and Smeed (1996), Shearman *et al.* (1998), and Rudnick (1996).

The method here is closest to the one used by Rudnick (1996), although developed independently. In both cases, a depth range of ADCP data are used to reference geostrophic velocities throughout the grid, non-divergence is enforced on this result to solve for streamfunction at a reference depth, and then absolute geostrophic streamfunction is determined at all depths.

III.3 Observations

From mid-June to early August, a standard grid of CTD stations off northern California was occupied five times (Figure III.1). The station spacing was 25 km, focusing on six alongshore sections 40 km apart (A-F, Figure III.1), and the maximum sampling depth was 500 m. CTD measurements were made with Neil Brown Instrument System CTDs [see Huyer *et al.* (1991) for more details].

An RD Instruments shipboard ADCP operated continuously during the five cruises. The 20-27 June and 29 July - 3 August surveys by the R/V *Wecoma* used a 307-kHz transducer with a bin width of 8 m and nominal depth range of 240 m, while the 6-12, 13-18, and 22-26 July

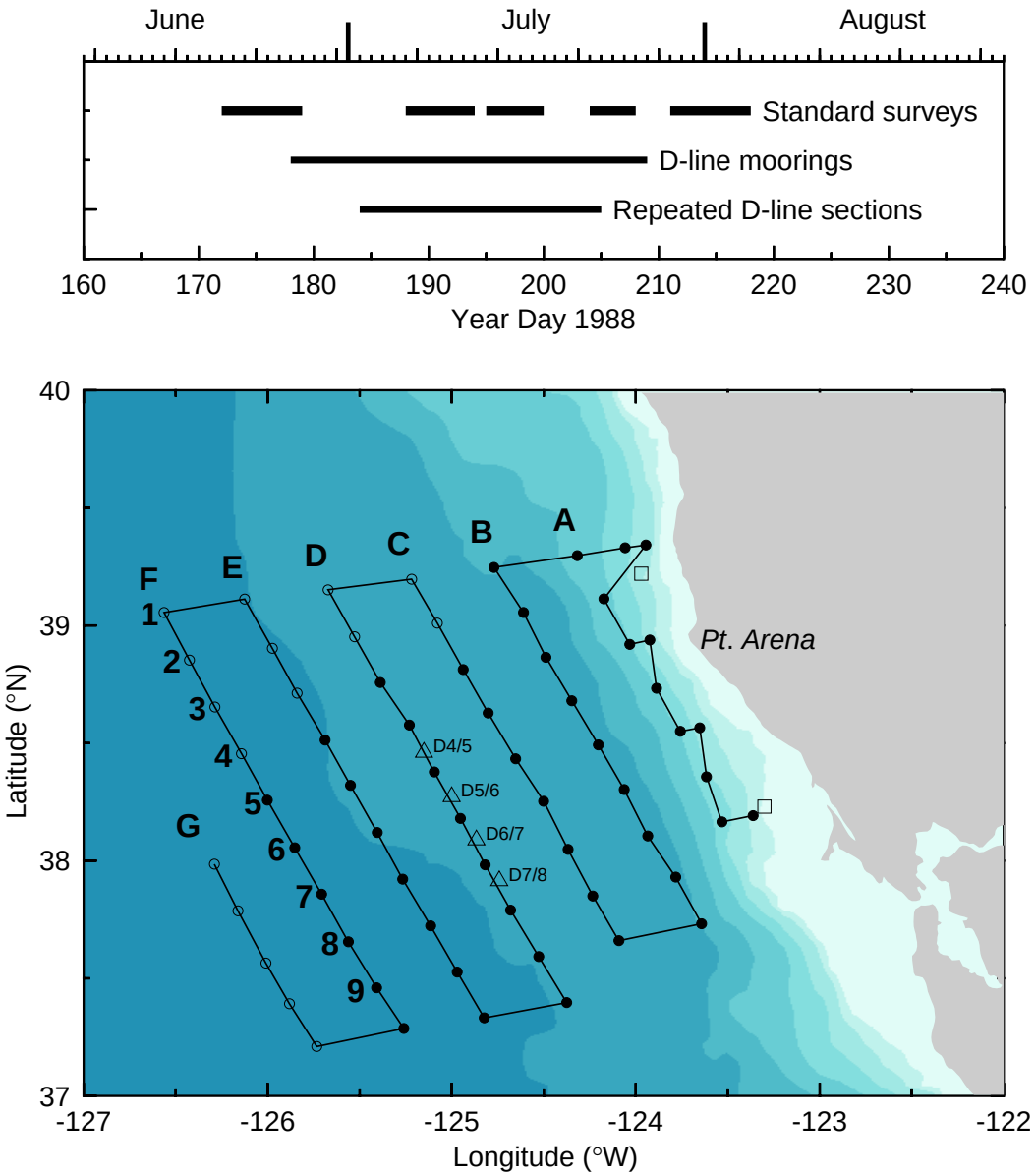

Fig. III.1. The station grid for the July-August 1988 CTZ experiment. Solid circles are locations occupied on all five complete surveys. Letters denote alongshore sections; numbers denote offshore-onshore lines. Triangles represent the D-line current meter moorings, and squares are the NDBC meteorological buoys. The 100, 200, 500, 1000, 2000, 3000, and 4000m isobaths are shown.

surveys by the R/V *Pt. Sur* used a 150-kHz transducer with a bin width of 4 m and a range of 350 m. The depth range of consistently good data was 25−200 m in both cases. LORAN-C navigation was available, and Huyer *et al.* (1991) do careful processing using the methods of Kosro (1985), resulting in absolute currents with rms errors of 0.05 ms^{-1}, low-pass filtered to suppress signals with periods less than 30 min. In the present study we use hourly ADCP from 25-200 m interpolated to 25 m intervals, similar to the 12.5 km spatially averaged data presented in Huyer *et al.* (1991).

The CTZ 1988 three primary current meter moorings were deployed 21-26 June and recovered 27-29 July. One mooring (D6/7) had Aanderaa currents meters at nominal 90, 140, 190, and 430 m depths. Two moorings (D5/6 and D7/8) had 307 kHz upward-looking RDI ADCPs at about 120 m (20-115 m range) and Aanderaas at 120, 150, 200, and 450 m. Here we make use of low-pass filtered (Kaiser window with half-power at 35 h) versions of the time series, as in Huyer *et al.* (1991).

Hourly wind measurements were made by the *Wecoma* and by the National Data Buoy Center (NDBC) buoys off Pt. Arena and Bodega Bay (Figure III.2). The *Wecoma* series includes the 2-23 July time period, when the ship was making repeated microstructure/ADCP sections up and down the D-line (not discussed here but thoroughly analyzed in Dewey *et al.* (1991)). The wind data were low-pass filtered (half-power at 40 h) to remove diurnal and shorter-period signals, and wind stress was calculated using the formulae of Large and Pond (1981). Wind stress was upwelling-favorable over most of the time period.

III.4 Methods

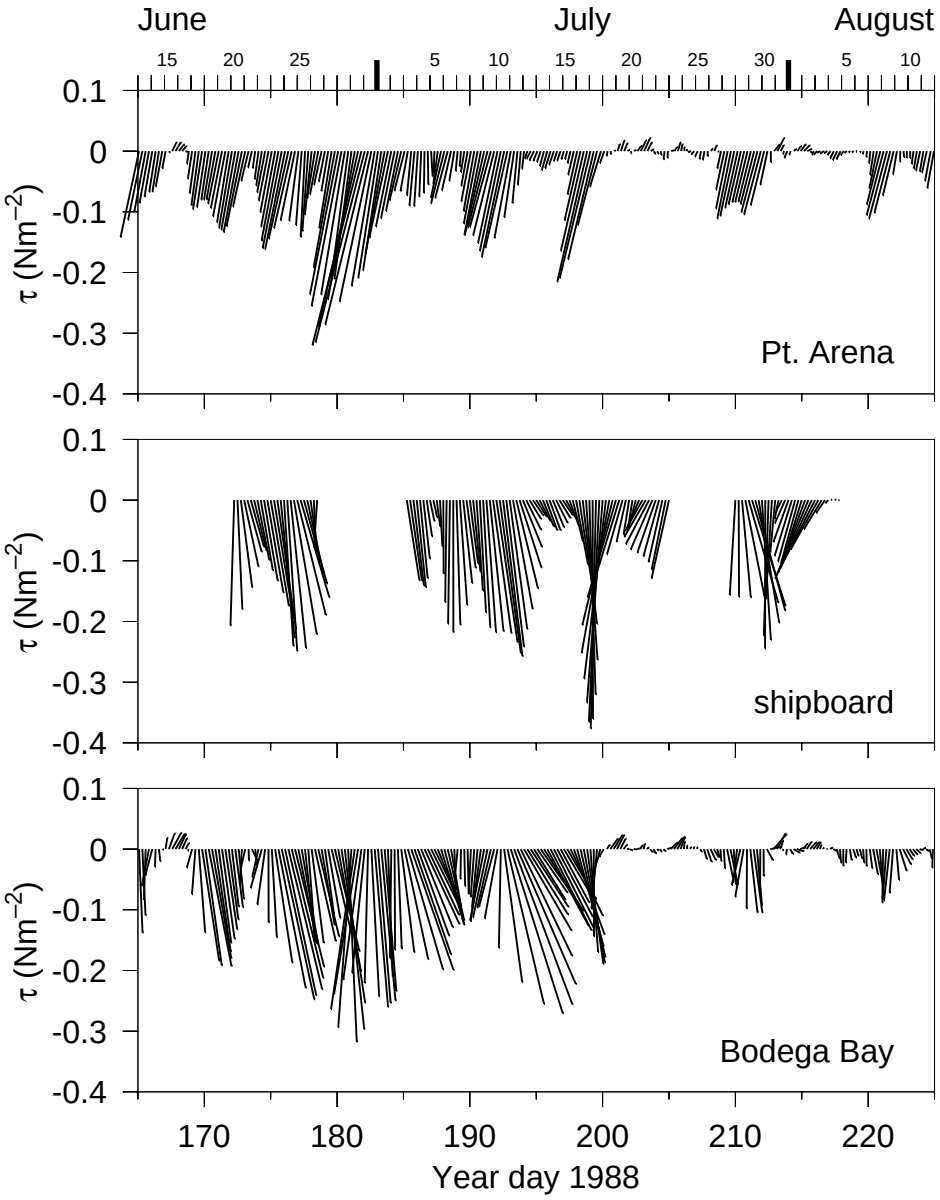

Fig. III.2. Low-passed (<0.6 cpd) six-hourly vector time series of wind stress measured from NDBC buoy at Pt. Arena (46014 at 39.22°N, 123.97°W, rotated to 341°T), from the R/V *Wecoma* (rotated to 341°T), and from NDBC buoy at Bodega Bay (46013 at 38.23°N, 123.30°W, rotated to 316°T).

III.4.1 Detiding the ADCP

Barotropic tidal currents in the region are estimated using an empirical model and then removed from the ADCP. The tidal estimation is covered in detail in Chapter II; we summarize here. A least-squares harmonic method similar to Candela *et al.* (1992) is used, where the M_2 tidal parameters are allowed to vary spatially using polynomial surface trend interpolation. The fit is normalized at each location by x/H, where x is distance offshore and H is bottom depth. The smaller S_2, K_1, O_1, and N_2 tidal constituents (with no spatial variation) are also determined from the analysis, but the M_2 dominates (83% of total tidal variance). Both CTZ 1988 data (shipboard ADCP and moored current meters) and historical current meter data are combined in a single calculation, yielding improved tidal estimates. The historical data include selected moored current meter records from the OPTOMA, LLWOD, NCCCS, and CODE experiments.

The estimated M_2 tide ellipses have semi-major axes varying from 1-4 cm/s across the region, largest over the slope. Uncertainties in the semi-major/minor axes vary from 0.2-0.4 cm/s (95% level). Ellipse orientation is roughly alongshore, rotation is counter-clockwise, and the alongshore phase speed of this poleward-moving tide is 130±30 m/s (95%). All of these results are consistent with previous regional tidal studies (Munk *et al.*, 1970; Noble *et al.*, 1987).

We do not have a good estimate of the baroclinic tide throughout the region, but at the CTZ moorings the M_2 baroclinic tidal currents vary from 5-10 cm/s (Chapter 2, Figure II.4). The presence of this unknown baroclinic tide might affect our maps of the geostrophic flow. Unlike the barotropic current which we removed, however, the baroclinic signal is also present in the hydrographic data. Thus we do not expect the baroclinic tide to significantly affect the

fitting of the geostrophic to the ADCP profiles (Figure III.3). Other portions of the baroclinic tide will be removed through the process of removing divergence (Eq. 3).

III.4.2 Objective analysis

Prior to combining the hydrographic and ADCP data for each of the five surveys, we grid the data horizontally to a rectangular 5 km grid using a Barnes objective analysis (OA) scheme (e.g. Daley, 1991). The Barnes OA is a successive corrections Gaussian weighted-averaging method that has long been used within the applied meteorology community. An iteration will retain features from the previous one, but will add a correction based on Gaussian smoothing of the differences between the observations and the analysis at the data locations. Following some of the recommendations of Koch *et al.* (1983) and Barnes (1994), we settle on a three-pass Barnes scheme which uses successive smoothing length scales of 30, 26, and 22 km. Scales smaller than these will be suppressed, while scales larger than these are freely allowed. Our OA method allows smaller scales to survive the gridding process, compared to methods used in previous studies with similar data sets. As part of the statistical OA method used by Walstad *et al.* (1991) and Kosro *et al.* (1991), for example, a Gaussian decay scale of 50 km is applied. Our choices are based on both the CTZ hydrographic station sampling plan and the length scales expected in mesoscale dynamics Koch *et al.* (1983). recommends consideration of the average nearest-neighbor distance in choosing the smallest smoothing radius. While the most frequent nearest-neighbor distance overall is 25 km, a fair number of 22 km spacings are also present. The internal Rossby radii of deformation calculated from historical data have an average of 25 km but range from 19-28 km within the CTZ region (Chelton *et al.*, 1998). The results are not extremely sensitive to the choice of the Barnes radii. The choice for the first-pass radius was also analyzed (with 0/500 dynamic height) using cross-validation. The cross-validation score

had a broad minimum for length scales from 25-30 km, another indication that the appropriate choice should be somewhere in this range.

From the hydrographic data, dynamic heights relative to 500 m at 25 m increments in the vertical are interpolated horizontally onto the 5 km rectangular grid, using the Barnes OA. Horizontal grid points outside the convex hull of data locations are not used. The detided ADCP velocities *u* and *v* from 25-200 m at 25 m increments are gridded separately, but using the same Barnes parameters. Allen and Smeed (1996) apply similar methods at this stage, although they use only a single-pass Gaussian interpolation for initial gridding of density and ADCP data. The multiple correction passes of the Barnes method improve the gridding quality (interpolations from the final grid to the data locations are in closer agreement with the data themselves).

III.4.3 Referencing geostrophy

Our aim now is to combine the hydrographic and ADCP data sets using the simplest dynamics: we assume the velocity field is horizontally non-divergent and in geostrophic balance. Under the quasi-geostrophic assumption (e.g. Walstad *et al.*, 1991), the gridded dynamic heights can be directly related to streamfunction:

$$\psi_{z/500} = \frac{g}{f_0}(\Delta D_{z/500}) - <\Delta D> \quad , \tag{1}$$

where northward geostrophic velocity $v_{g,z/500} = \partial\psi/\partial x$, eastward geostrophic velocity $u_{g,z/500} = -\partial\psi/\partial y$, g is the acceleration of gravity, f_0 is the local constant Coriolis parameter, subscript $z/500$ means value at z relative to 500 m, and the angle brackets denote the horizontal spatial average. The approach is to first use a depth range of ADCP velocities at each horizontal location to reference the corresponding geostrophic velocity profile, minimizing at each horizontal grid point:

$$\sum_{z=z_1}^{z_2} [(u_{g,z} - u)^2 + (v_{g,z} - v)^2] \ , \tag{2}$$

where $u_{g,z} = u_{g,500} + u_{g,z/500}$, $v_{g,z} = v_{g,500} + v_{g,z/500}$, and u, v are the OA mapped ADCP velocities. This least-squares fit of the ADCP profile to the geostrophic shear determines the deviation from the lnm assumption ($u_{g,500}$, $v_{g,500}$) at each grid point. Then, non-divergence is enforced at 500 m by solving for the streamfunction ψ_{500} from $\mathbf{u}_{g,500}$:

$$\nabla^2 \psi_{500} \ = \ \nabla \times \mathbf{u}_{g,500} \tag{3}$$

The boundary conditions for (3) can be an important issue. Using **u** directly at the edges of the analysis region, the simplest approach (eg., Pollard and Regier, 1992; Allen and Smeed, 1996), amounts to assuming that the boundary **u** is already divergenceless and can introduce noise into the solution. We use the version III method of Hawkins and Rosenthal (1965), who were interpolating scattered wind observations, introduced to the oceanographic community by Carter and Robinson (1987). This approach involves a prior step of solving for velocity potential, forced by the field of divergence calculated from **u**, with a boundary condition of zero on all sides. The result is used solely to add a correction term to the boundary conditions for (3). This approach has the effect of maximizing the amount of kinetic energy which ends up in the resulting streamfunction field. In a few tests we found 10% increases in kinetic energy after applications of the method.

We use second-order-accurate finite-differences on a 5 km rectangular grid to solve (3), and we also apply the condition of no-normal-flow through our northeastern boundary along the continental slope. We use the Poisson solver developed by Cummins and Vallis (1994), which handles irregular boundary conditions.

Absolute geostrophic streamfunction ψ_z can now be figured at all levels, using the reference ψ_{500} determined by (3). The divergence removed by solving (3) is assumed to be noise due to internal tides, lack of synopticity, ADCP errors, etc. In our application of the method to each

of the five surveys, the divergence fields removed have rms values of 0.03-0.05 ms^{-1}. By removing this divergence, we are adjusting the flow field in order to maintain conservation of mass. These adjustments are similar in size to the rms uncertainties in absolute velocity inherent in the ADCP data (0.05 ms^{-1}), so we are remaining within our original measured velocity bounds.

Although developed independently and with notational differences, our approach is similar to the method in section 2 of Rudnick (1996), who applied it to a set of SeaSoar/ADCP surveys of the Azores front. Some differences: he uses both density and ADCP data in the depth range 16-264 m, while we use density data in the range 0-500 m and ADCP data from 75-200 m; we use a different method of solving the Poisson equation for the streamfunction, as discussed above.

III.4.4 ADCP depth range

We briefly explore the issue of choosing $z_{1,2}$ in (2), the range of ADCP to use. While near-surface ADCP will begin to be affected by ageostrophic phenomena which violate our quasi-geostrophic assumptions, this consideration must be balanced against the advantage of including more data in any least-squares calculation. Inertial oscillations can contaminate the ADCP even at deep levels (see Chapter IV). Rudnick (1996) makes the unusual choice of using the entire 16-264 m depth range of ADCP; most studies choose a fairly deep single level. The decreasing data quality with depth of shipboard ADCP can also be a concern, however.

To help guide our choice, we inspect the individual fits of profiles at selected grid points; Figure III.3 is an example for an onshore-offshore section across the first survey grid. Inertial motions and other effects can be seen in the 25-200 m ADCP profiles, not present in the smoother geostrophic profiles derived from the density data. This is typical; Bacon (1994) for

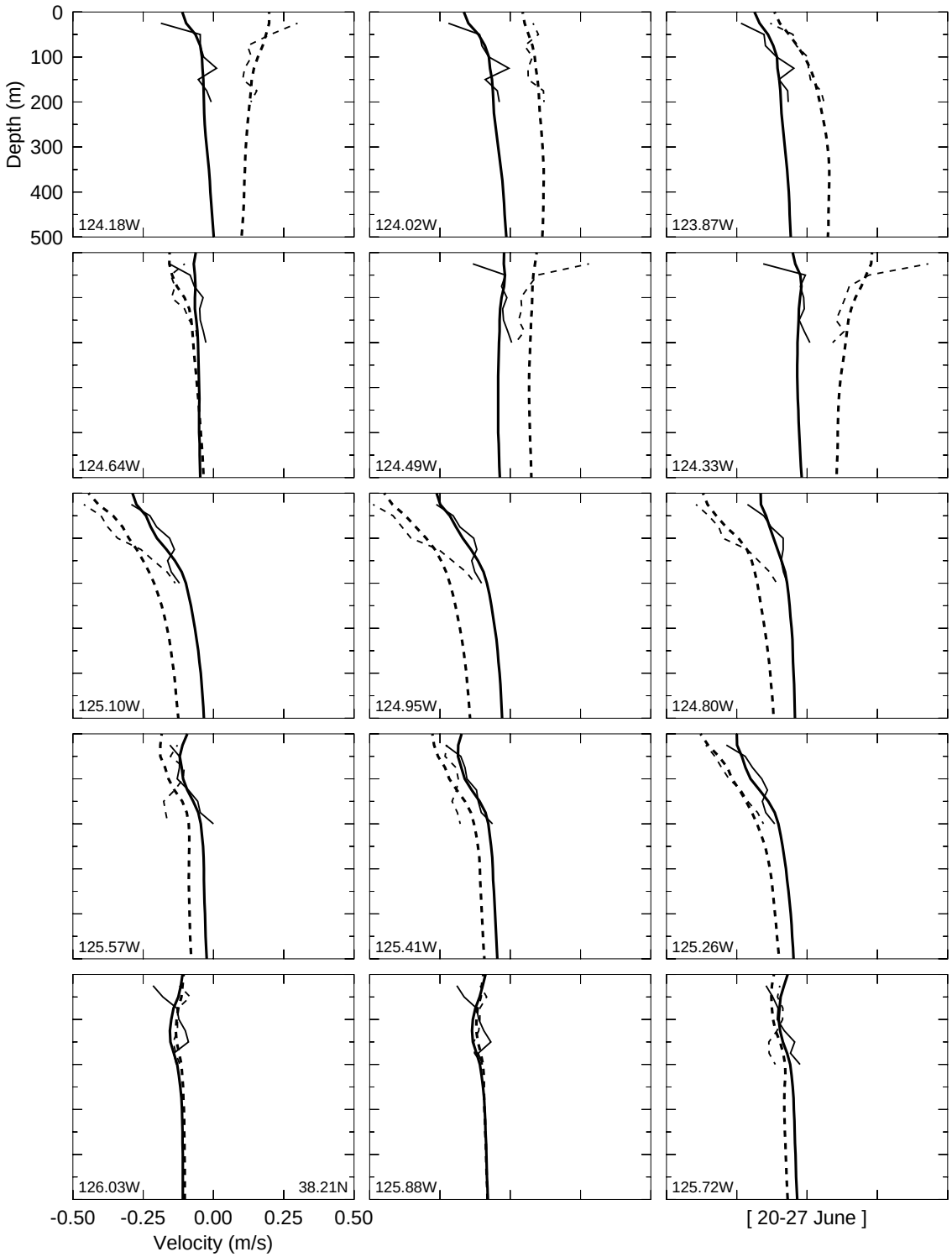

Fig. III.3. Fitted geostrophic profiles (0-500 m lines) and ADCP (25-200 m lines) for east(solid) and north(dashed) velocity components, for selected grid points along 38.21°N from the 20-27 June survey.

example shows many such comparisons, with similar characteristics. The 25 m ADCP is clearly within the surface Ekman layer, leading to frequent deviations away from the geostrophic profile. The 50 m and deeper levels are not so obviously affected. The overall profile fit residuals (Figure III.4) for various 50-200 m depth range choices do not vary much, 0.01-0.03 ms^{-1} rms. We settle on z_1 = 200 m and z_2 = 75 m as a reasonable compromise which maximizes the quantity of ADCP data available while avoiding near-surface effects.

III.5 Absolute geostrophic velocities

Applying the method to each of the CTZ 1988 hydrographic/ADCP surveys, we infer significant (O 0.1 ms^{-1}) flow at 500 m (Figure III.5 upper panels). A central feature common to all five surveys is a region of poleward flow, usually adjacent to the continental slope. This is a good example of an oceanic feature revealed by our method of combining the ADCP and hydrographic data.

After solving (3) for the divergenceless flow, subtracting this from the original $\mathbf{u}_{g,500}$ yields the residual, which contains all of the divergence. The residual flow is smaller (about 0.03-0.05 ms^{-1} rms) and lacks much of a pattern (Figure III.5 lower panels). The maxima seen among the residuals in the vicinity of the slope could be due to internal tides, which can be about this size close to the slope (Torgrimson and Hickey, 1979). Lack of synopticity during the surveys (which each took about 5 days to complete) can also easily account for residuals, particularly close to the core of the main jet, which we know to be sometimes translating and rotating spatially at smaller time scales (Dewey *et al.*, 1991). Our divergenceless flow field solution will average out these undulations.

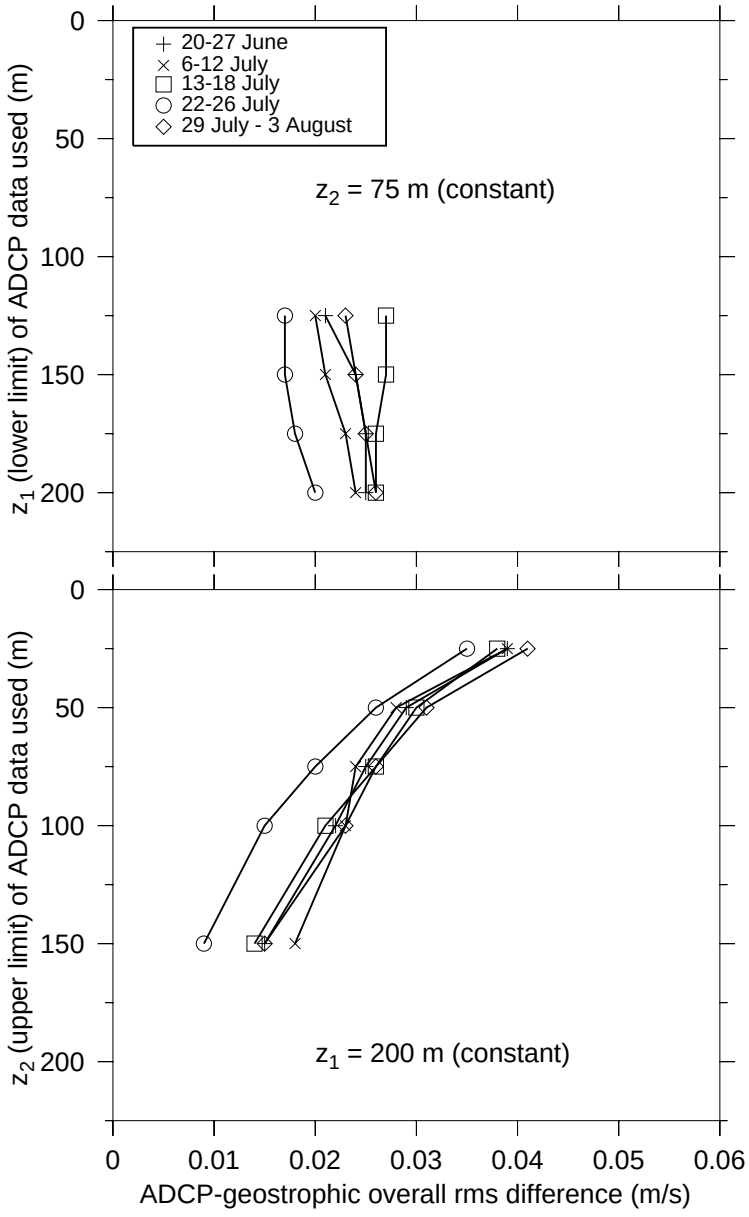

Fig. III.4. Overall rms residuals after fitting of different ADCP depth ranges to the geostrophic profiles.

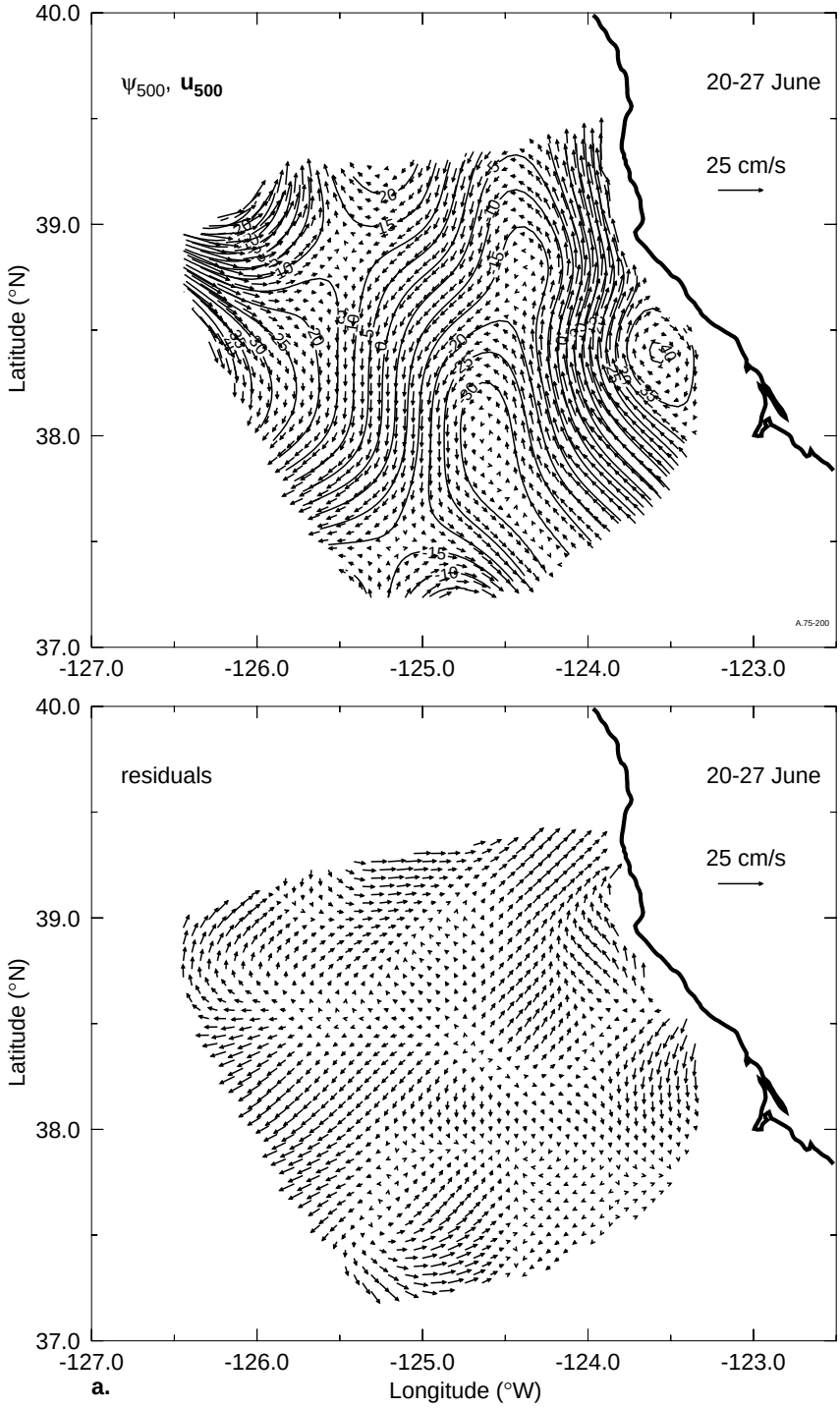

Fig. III.5 Absolute geostrophic streamfunction (10^2 m^2s^{-1}) and sub-sampled **u** (upper panels) and $\mathbf{u}_{resid}$ (lower panels) at 500 m depth, for 20-27 June (a), 6-12 July (b), 13-18 July (c), 22-26 July (d), and 29 July - 3 August (e).

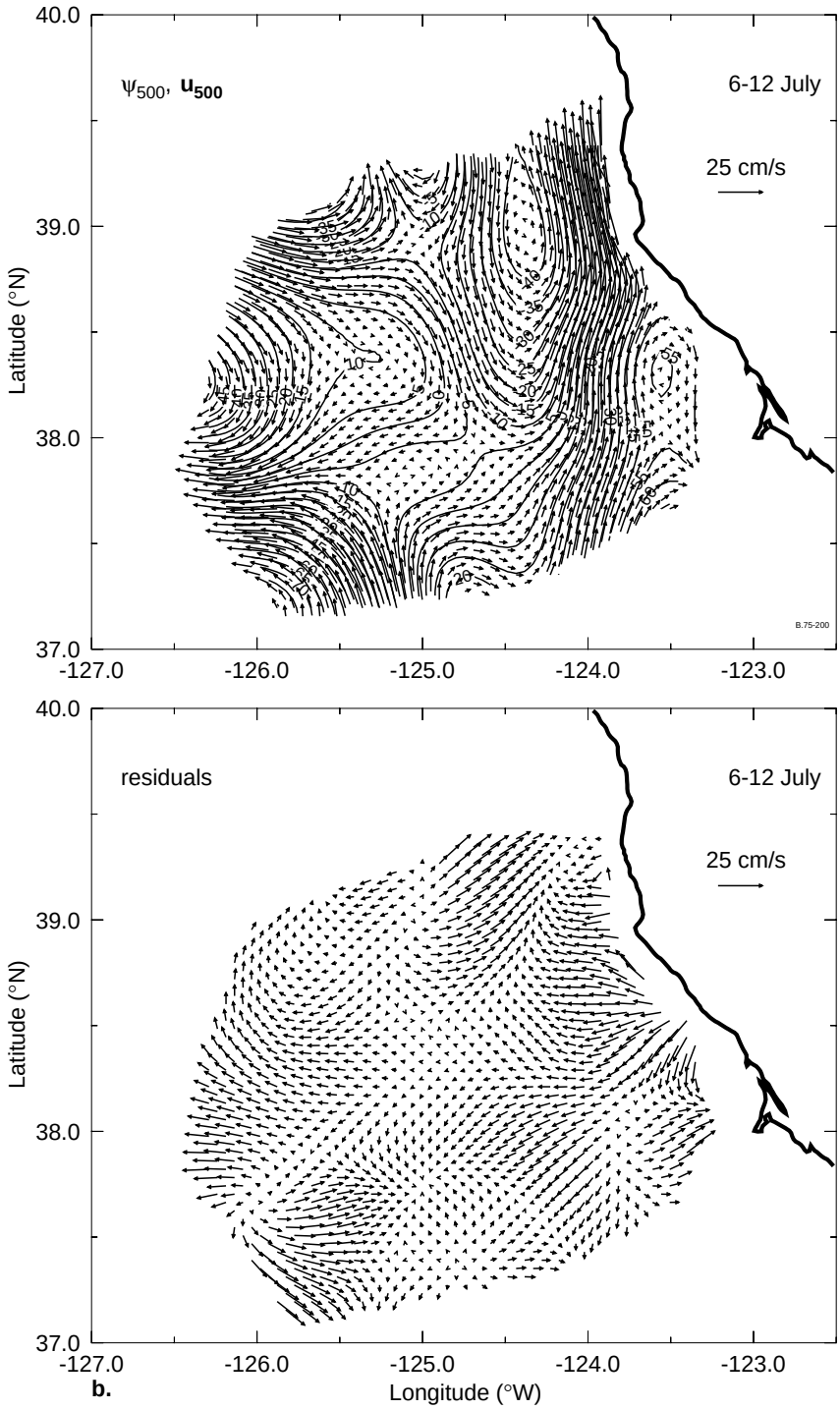

b.

Fig. III.5, Continued

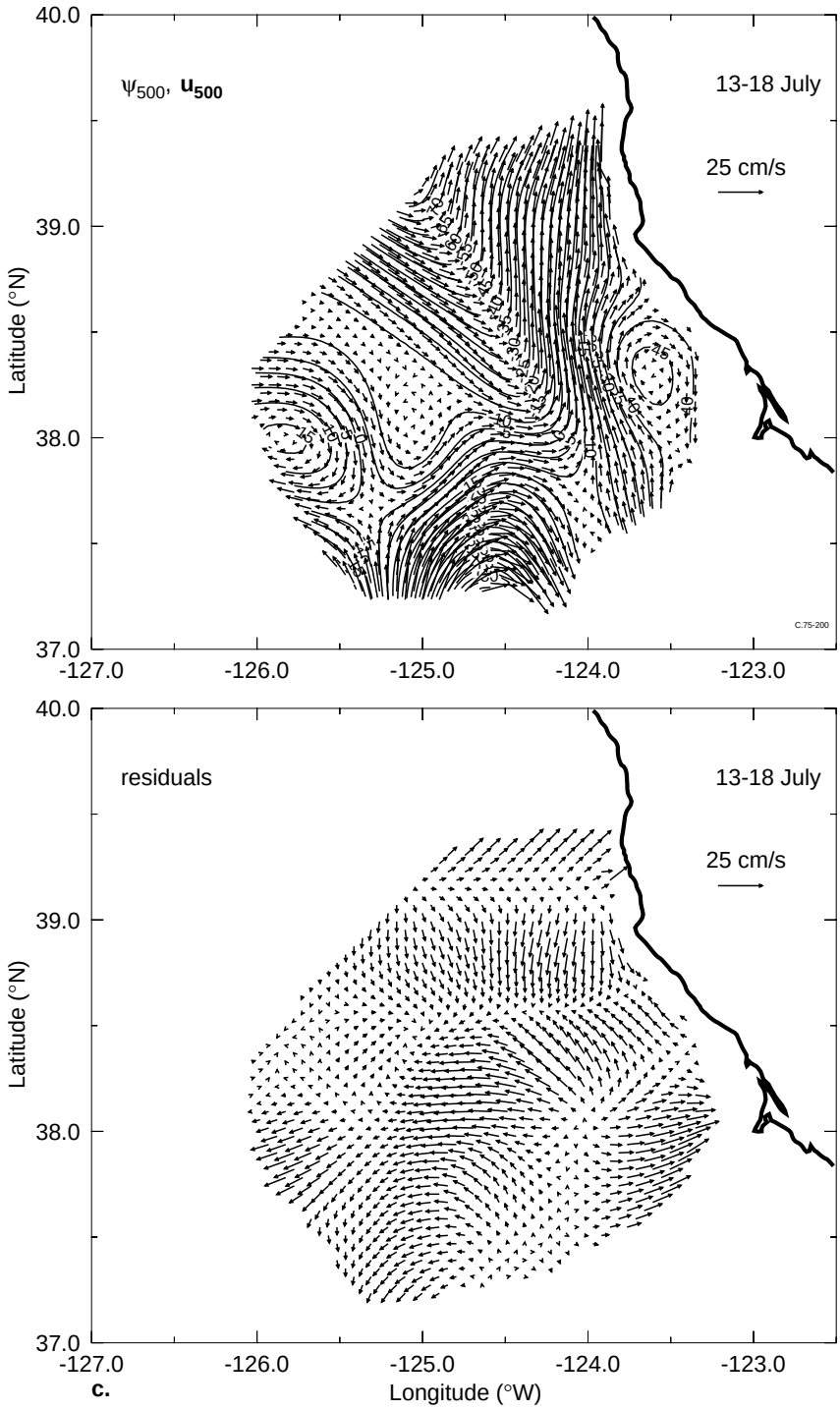

c.

Fig. III.5, Continued

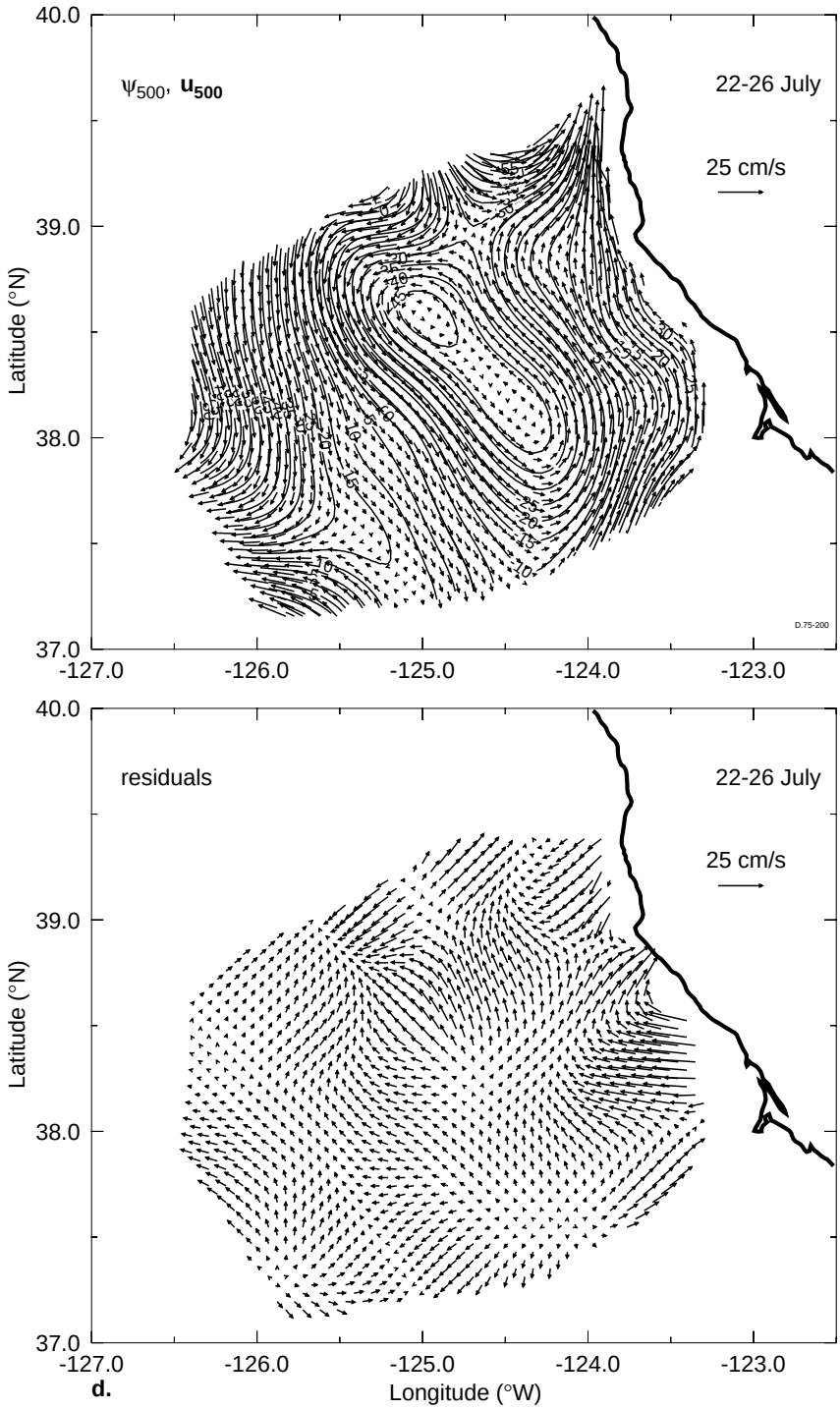

Fig. III.5, Continued

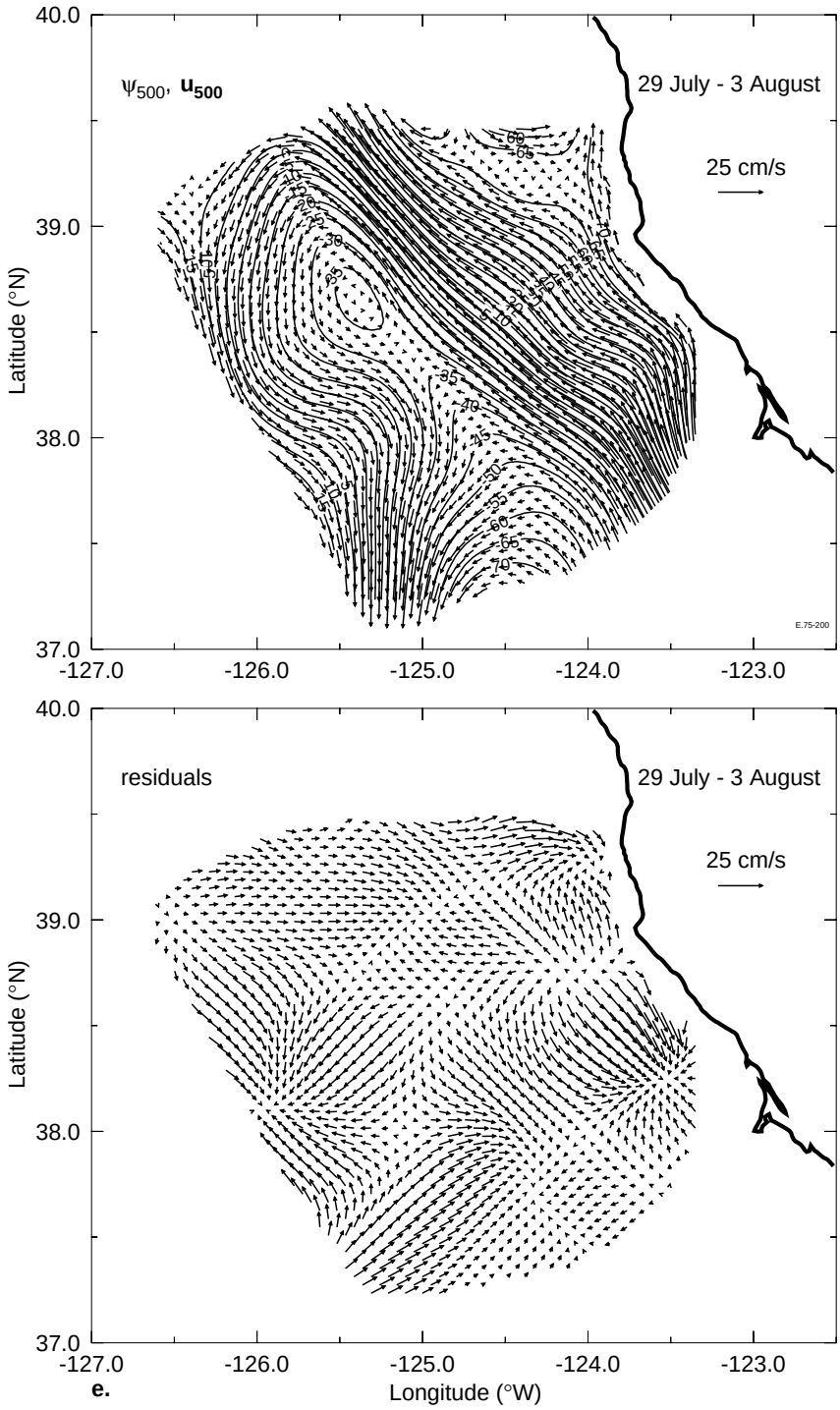

e.

Fig. III.5, Continued

III.5.1 Horizontal maps

The absolute surface geostrophic flow (Figure III.6 lower panels) consistently shows a strengthened CTZ jet compared to the 500 m lnm fields (Figure III.6 upper panels). The equatorward jet is the dominant feature throughout the sequence of five surveys over six weeks. During the first three surveys (Figure III.6a,b,c), the jet position and strength is relatively consistent, entering close to the northeast corner of the grid as a southward current and exiting the offshore side of the grid as a significantly stronger west-southwest flow. During the fourth and fifth surveys (Figure III.6d,e), as it enters the region the jet has a well-developed meander, only partially resolved by our grid. It exits the grid as a roughly southward and wider flow.

In addition to showing the true strength of the jet, the absolutely referenced fields are better able to resolve the meandering path. During the 13-18 July survey (Figure III.6c) for example, we see a narrower jet with a more developed meander in the lower panel. The path of the jet is also more consistent with the change in orientation observed at the D-line by both the moorings and the repeated microstructure sections at about this time (Huyer *et al.*, 1991; Dewey *et al.*, 1991). The ADCP data sets have both better along-track resolution and the ability to provide along-track as well as cross-track velocities, compared with geostrophic velocities from the hydrographic sampling alone. The ADCP information is thus providing greater spatial resolution, in addition to providing the reference velocity at 500 m.

The absolute geostrophic flow at 200 m (Figure III.7 lower panels) also has the equatorward jet as a primary feature, moving and evolving throughout the survey sequence in a manner similar to the surface flow. In addition, all five surveys show a region of poleward flow inshore of the equatorward jet. At this level, the base of the equatorward CTZ jet is interacting with the

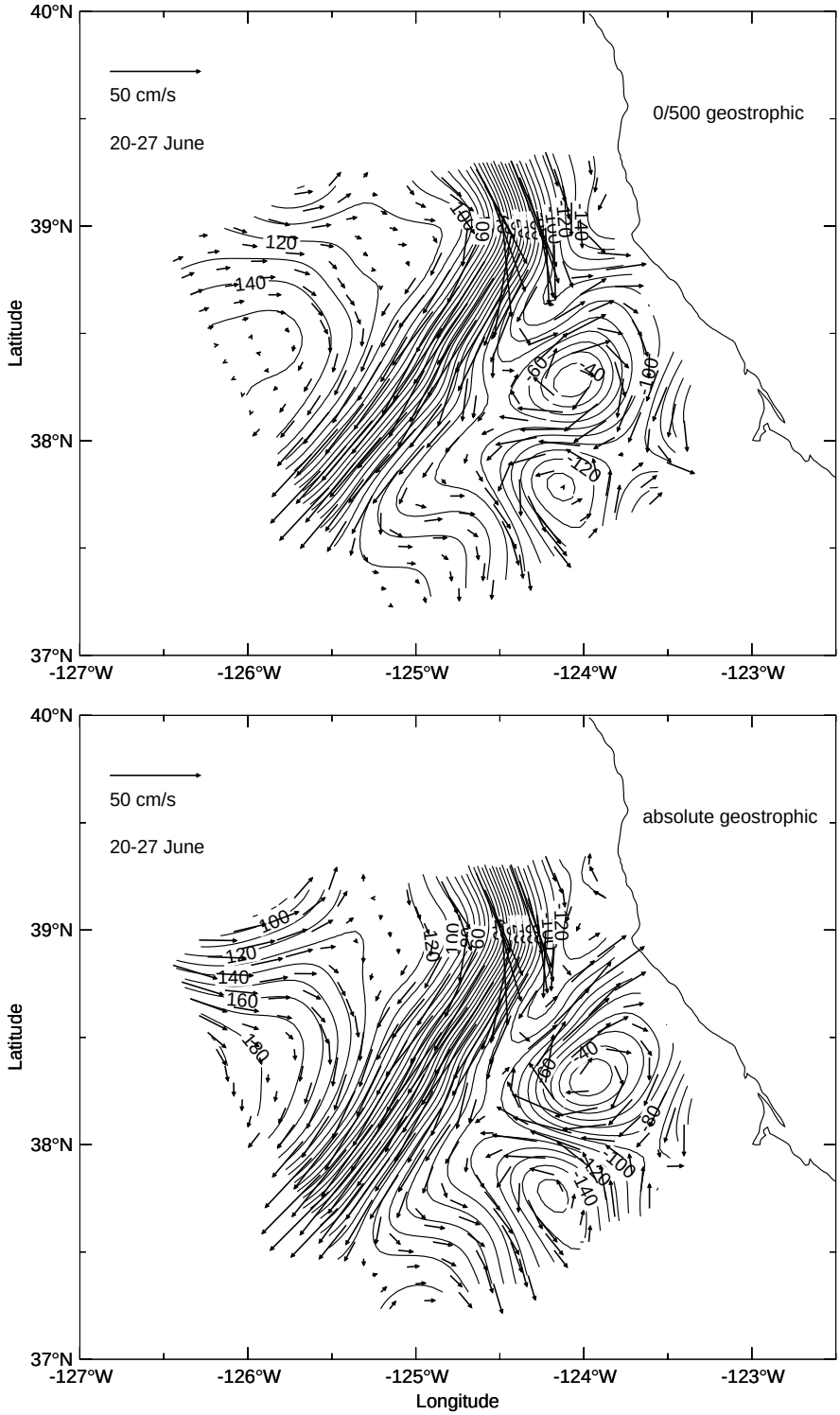

Fig. III.6 Geostrophic streamfunction (10^2 m^2s^{-1}) at the surface relative to 500 m (top) and absolute (bottom), with sub-sampled **u** overlaid, for 20-27 June (a), 6-12 July (b), 13-18 July (c), 22-26 July (d), and 29 July - 3 August (e).

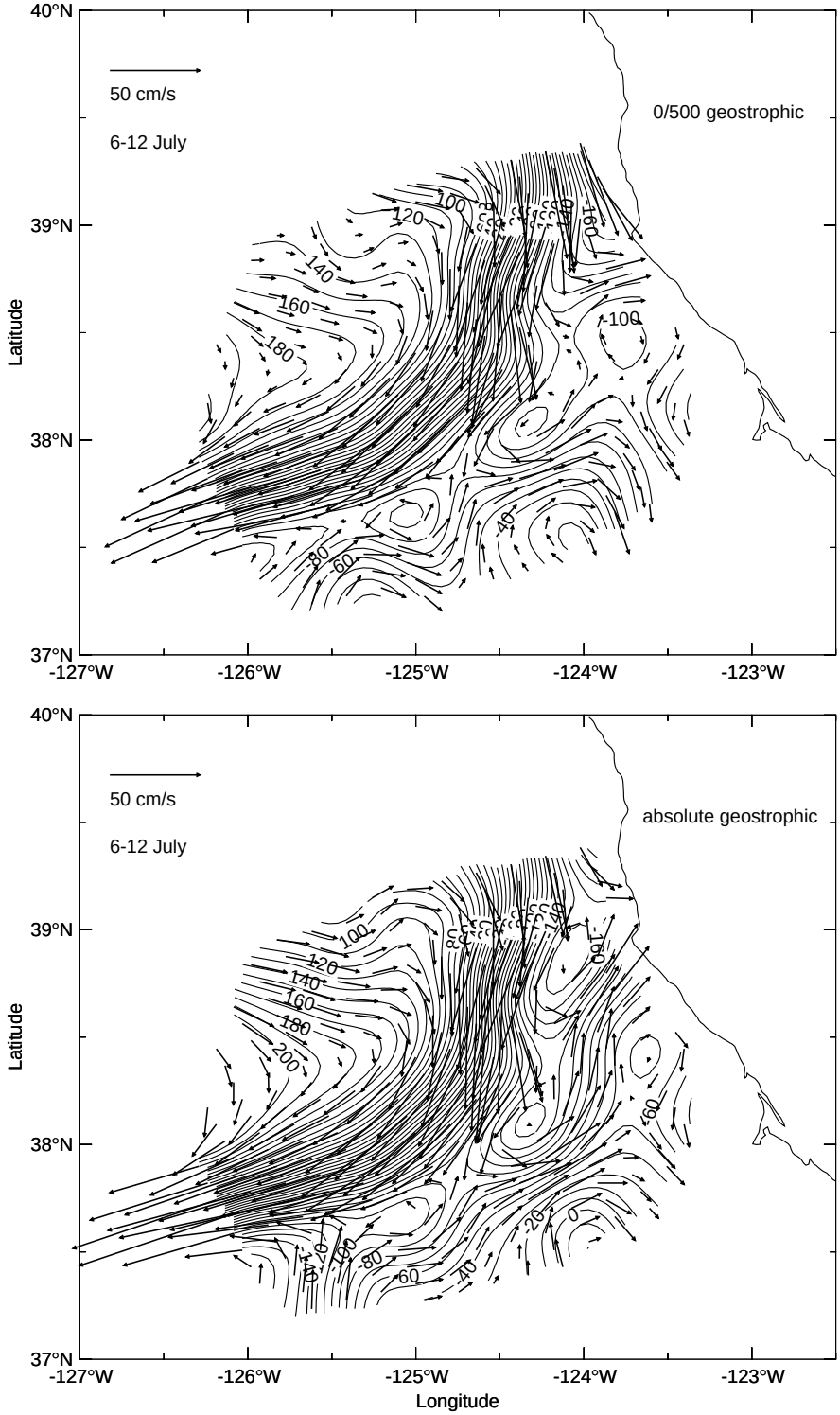

b.

Fig. III.6, Continued

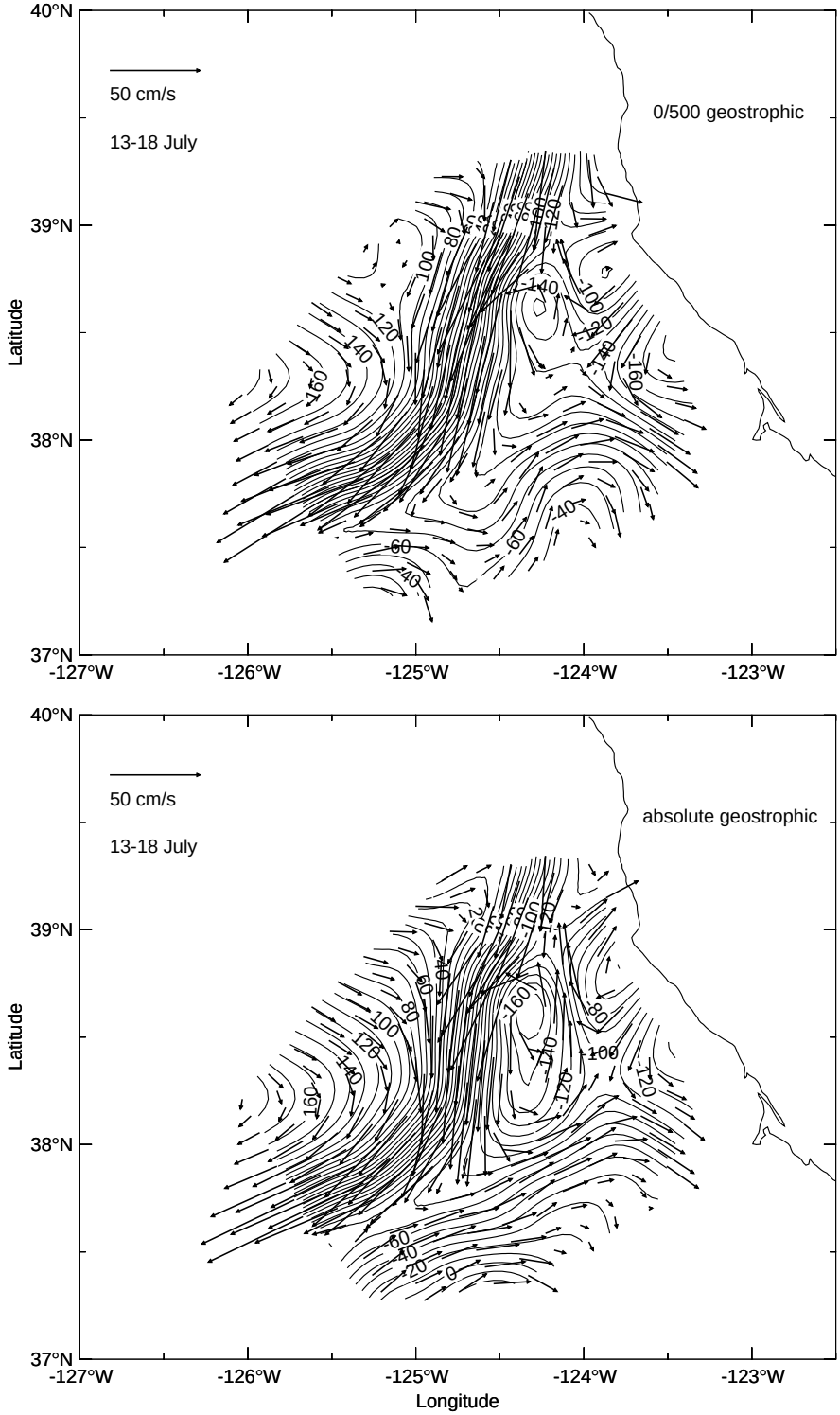

c.

Fig. III.6, Continued

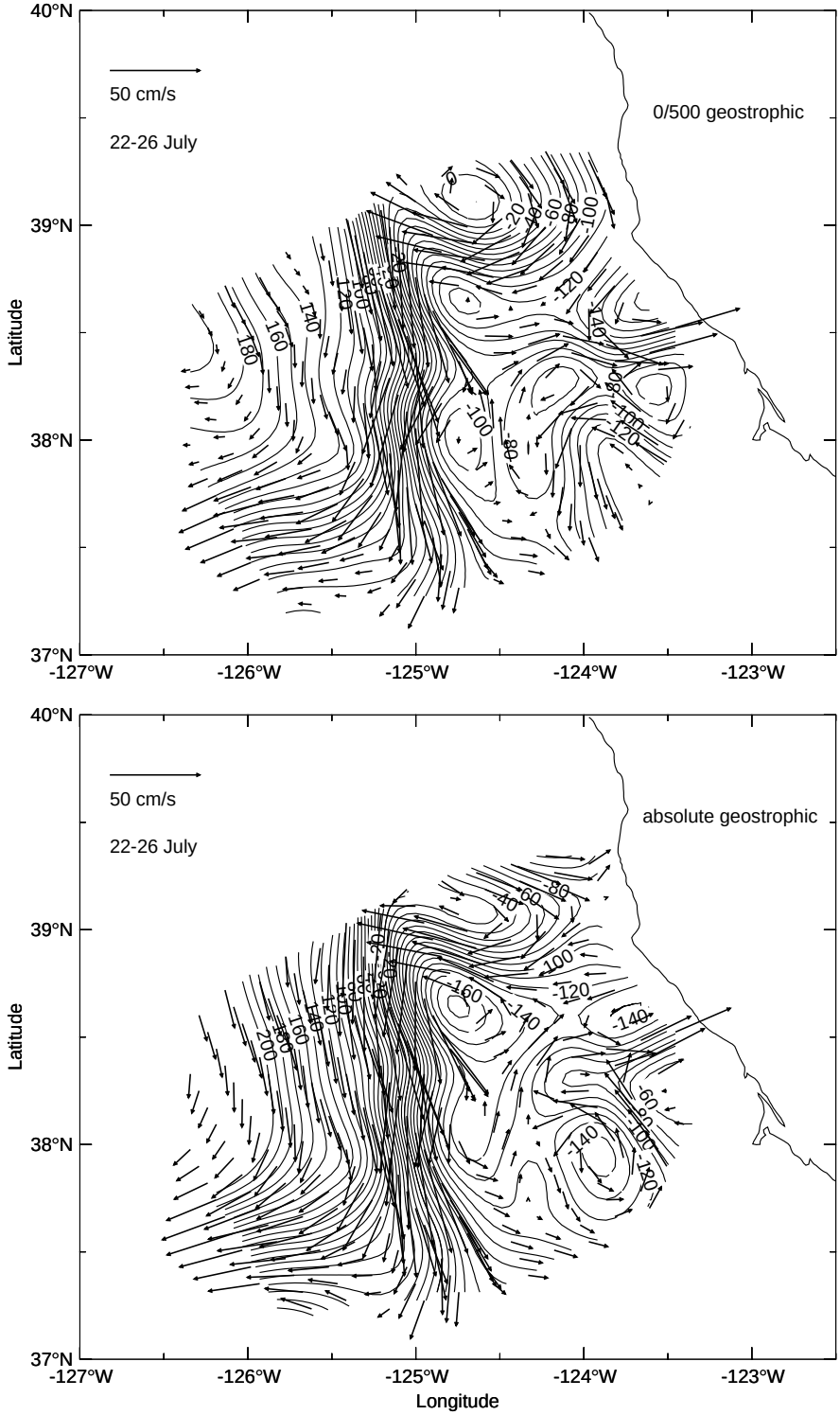

d.

Fig. III.6, Continued

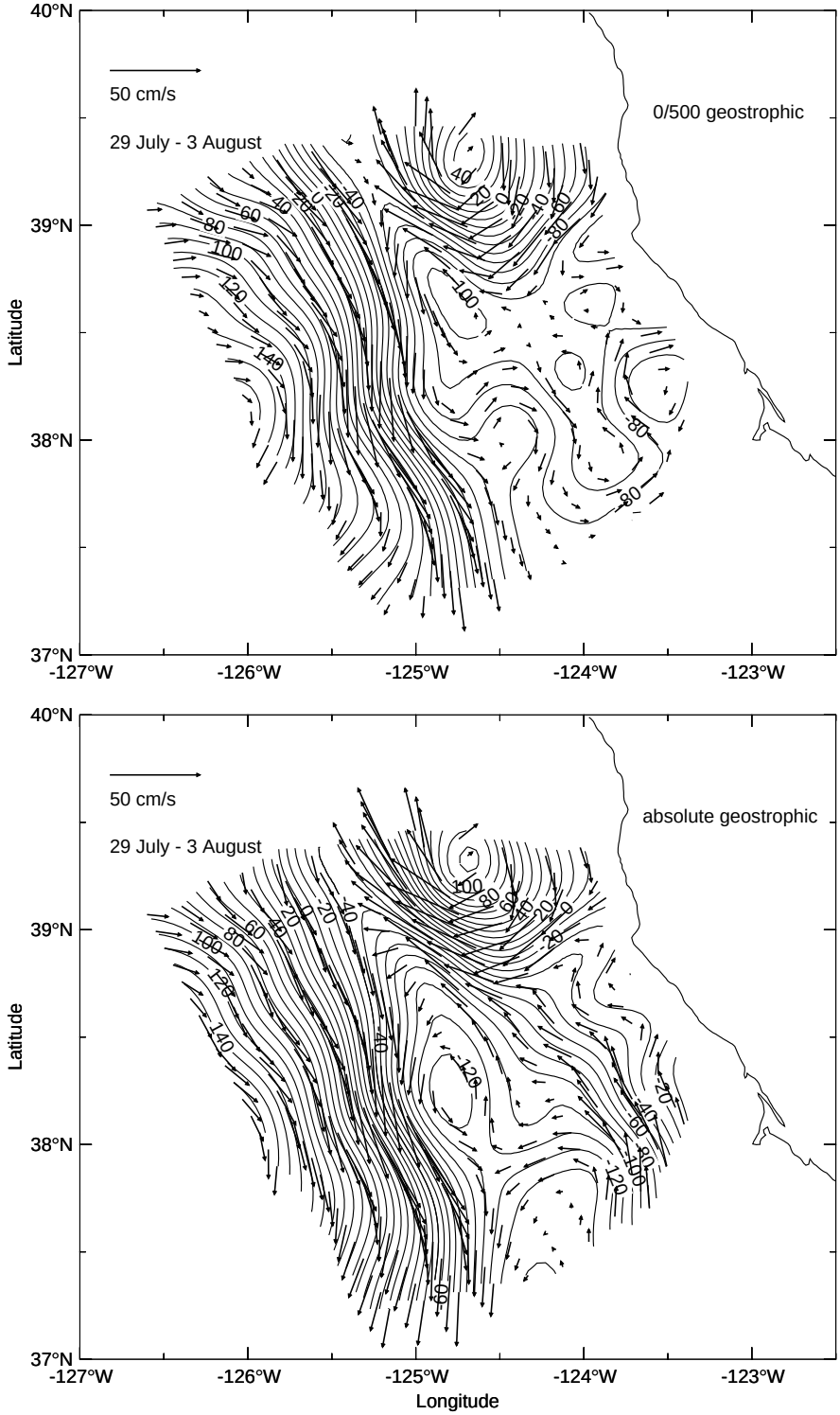

e.

Fig. III.6, Continued

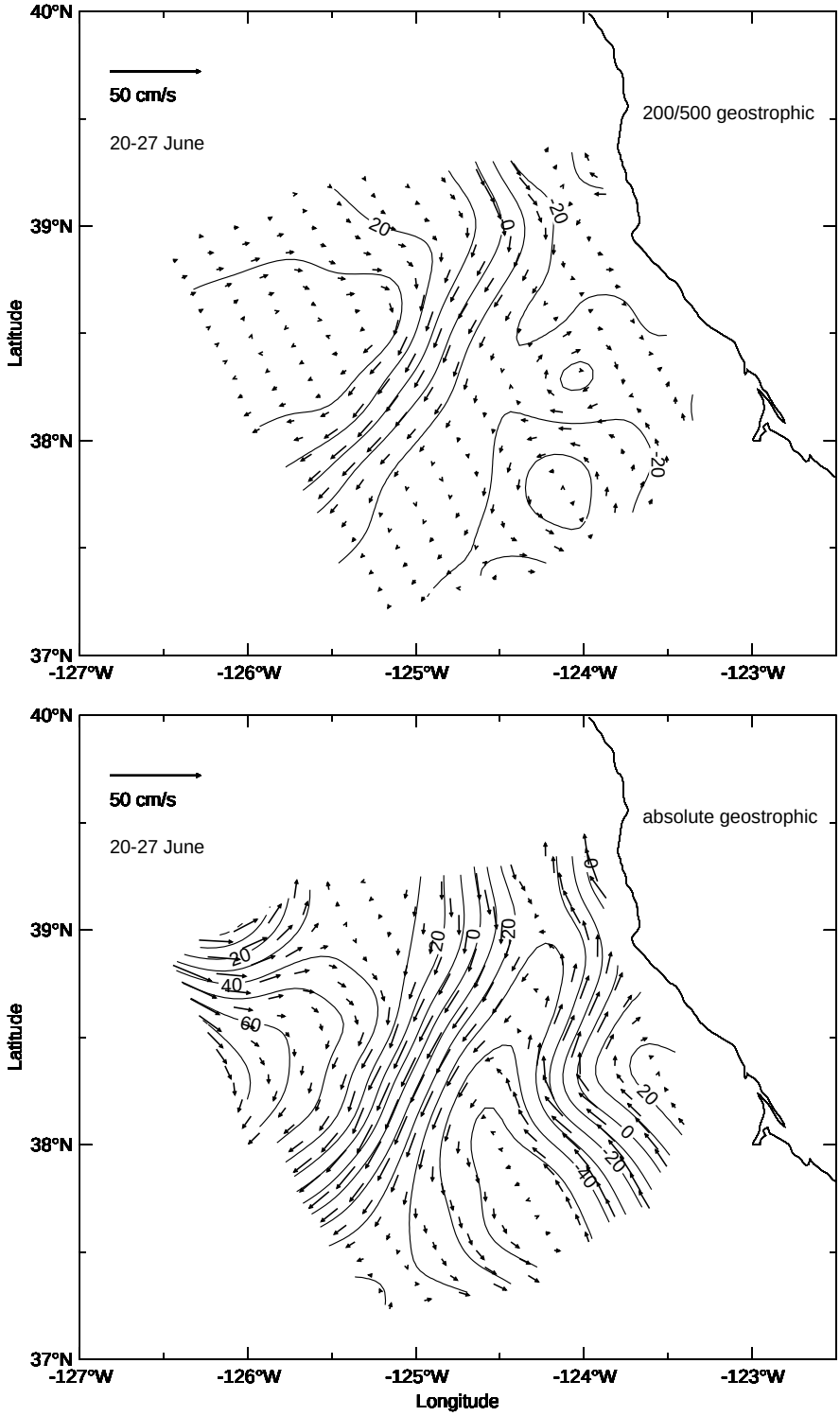

Fig. III.7 Geostrophic streamfunction (10^2 m^2s^{-1}) at 200 m relative to 500 m (top) and absolute (bottom), with sub-sampled **u** overlaid, for 20-27 June (a), 6-12 July (b), 13-18 July (c), 22-26 July (d), and 29 July - 3 August (e).

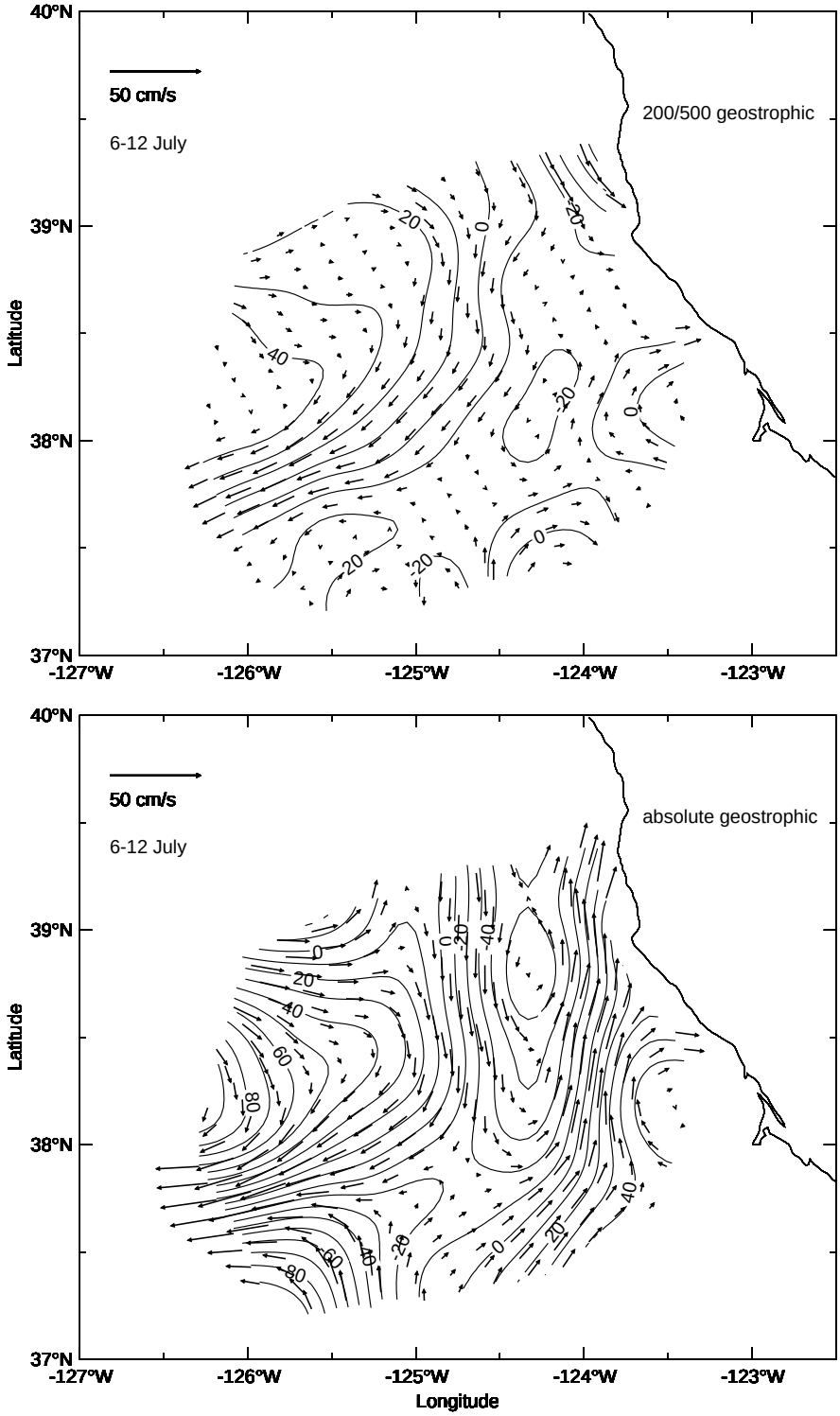

b.

Fig. III.7, Continued

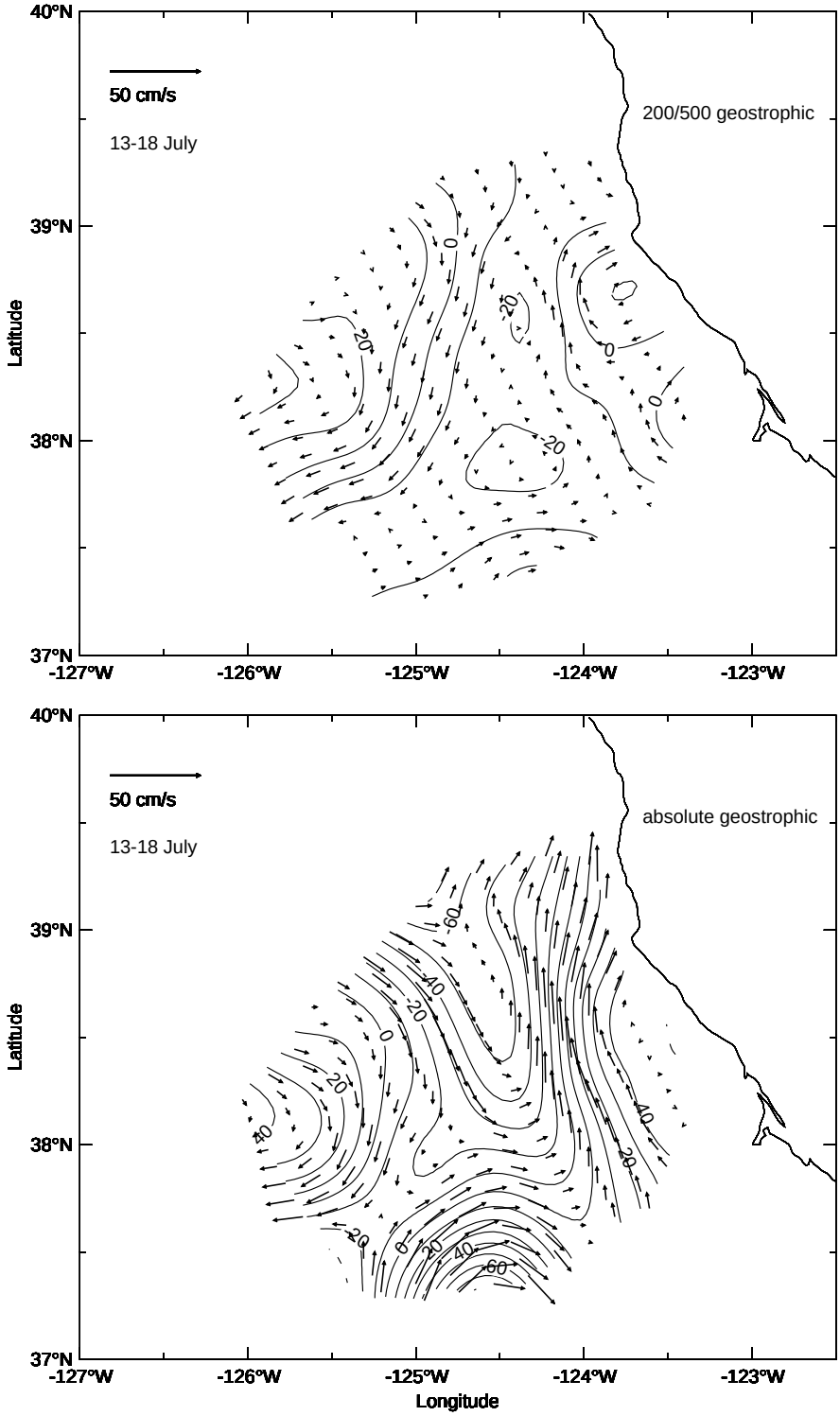

c.

Fig. III.7, Continued

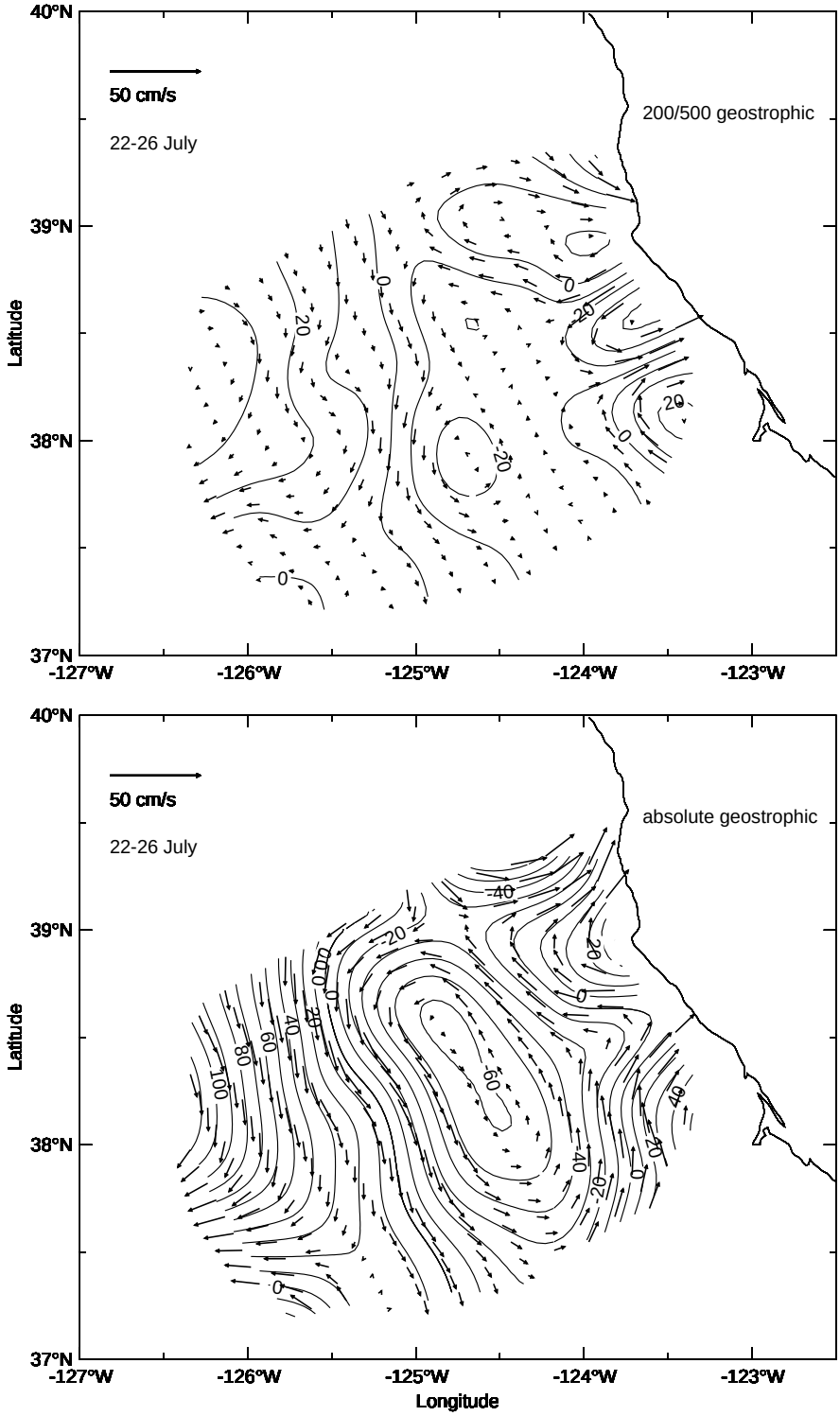

d.

Fig. III.7, Continued

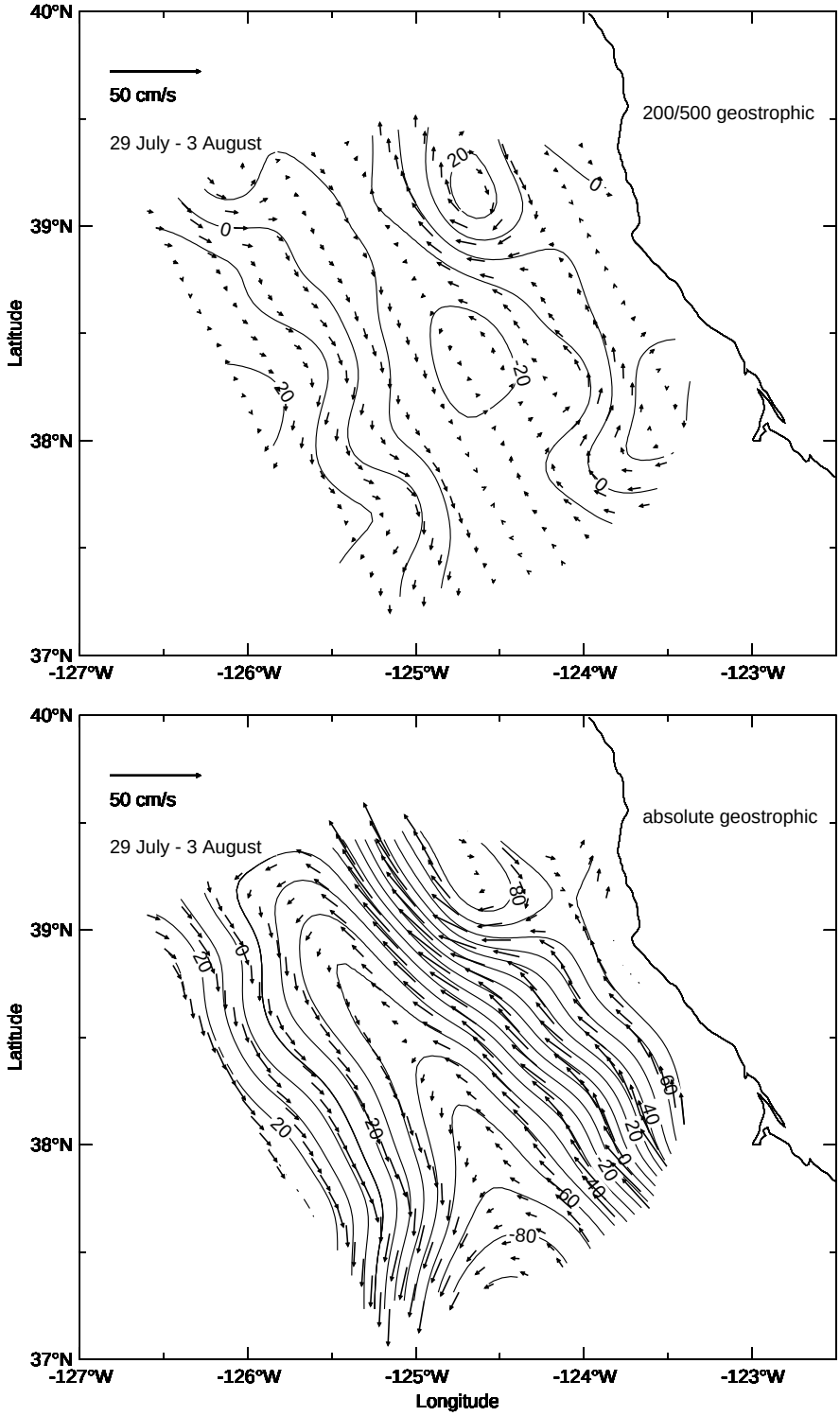

e.

Fig. III.7, Continued

upper portion of the poleward undercurrent, in a complex manner at times. The undercurrent is usually inshore of the CTZ jet, but during the 29 July - 3 August survey it bifurcates off of Pt. Arena (Figure III.7e). Most of the flow veers offshore and then continues north, coincident with the CTZ jet which is experiencing a sharp meander to the north at this point (Figure III.6e), while a smaller portion continues north along the slope. This interaction and separation of most of the undercurrent away from the slope is consistent with maps of water mass properties, which show typical relatively warm and salty undercurrent water away from the slope (Huyer *et al.*, 1991).

III.5.2 Vertical sections

As the jet enters our survey region at about 39°N, initially it appears in vertical cross-section as a strong equatorward jet about 50 km wide, 0.5 ms^{-1} velocity at the surface, with a transport of 2.8 $\times 10^6 m^3 s^{-1}$ (Figure III.8). During the next survey (6-12 July), the jet widens and increases its transport to 3.1 $\times 10^6 m^3 s^{-1}$, in combination with a strengthening poleward undercurrent hugging the slope. From 13-18 July, the undercurrent and jet can no longer be clearly distinguished and are crossing. After this time, the jet is no longer well resolved by this section.

The strongest jet observed is at the offshore F line, as it exits the region during the 6-12 July survey (Figure III.9). At this time the jet is nearly normal to the section, 100 km wide, and has 0.6 ms^{-1} core velocity at the surface. The transport of 7.2 $\times 10^6 m^3 s^{-1}$ represents a 70% increase over the value relative to 500 m (4.2 $\times 10^6 m^3 s^{-1}$).

It is not surprising that a jet with such large horizontal and vertical shears becomes increasingly unstable after this survey. As with the idealized instability processes studied in Pierce *et al.* (1991) (Chapter V) and Allen *et al.* (1991), a small perturbation can be sufficient to

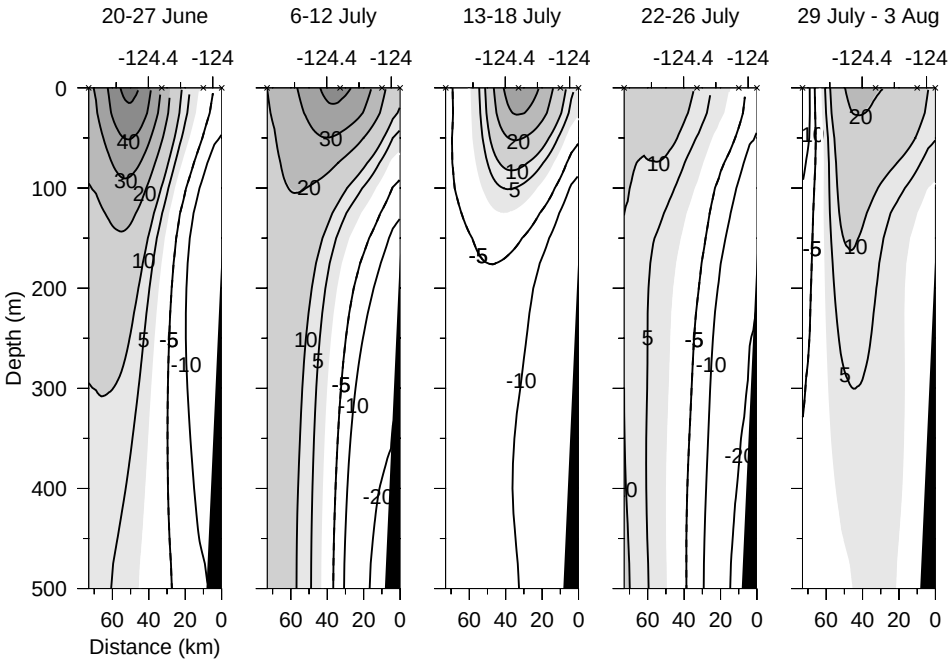

Fig. III.8 Vertical cross-sections of absolute geostrophic velocity (cm/s, equatorward shaded) at offshore-onshore line 1, the northeast corner of the survey grid.

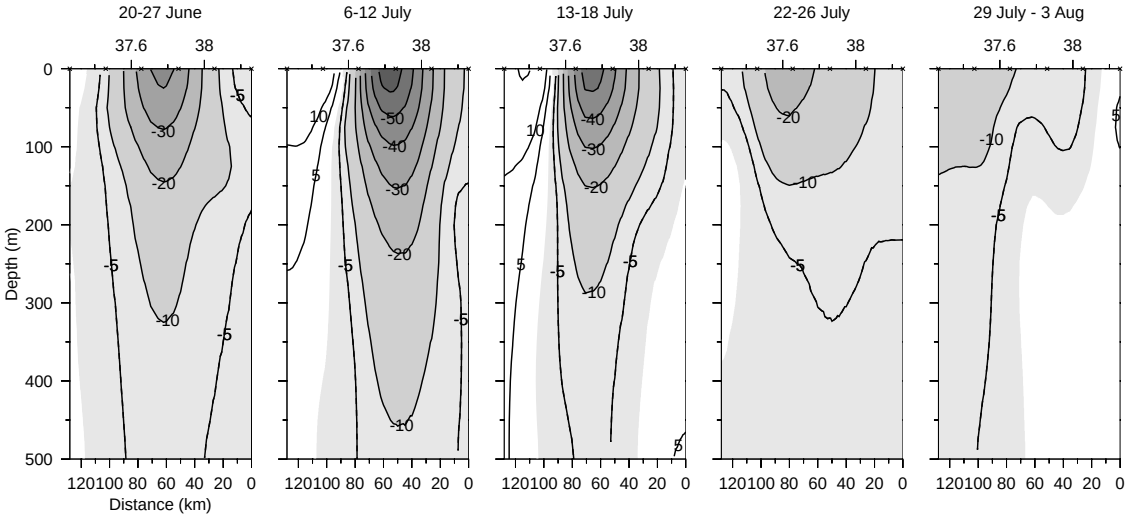

Fig. III.9 Vertical cross-sections of absolute geostrophic velocity (cm/s, south-southwest shaded) at line F, the offshore boundary of the grid.

cause the growth of a large jet meander. The perturbation which caused the mid-July shift in jet orientation might have been the relaxation seen in the wind stress on July 12 at Pt. Arena and July 13 in the *Wecoma* record (Figure III.2).

The offshore-onshore line 5 serves well for looking at the jet structure during the last two surveys after the mid-July shift, when the jet core is oriented nearly north-south (Figure III.10). The first panel of Figure III.10, the 20-27 June case, is remarkably similar to the other two panels, although the jet was crossing the section a bit obliquely (Figure III.6a). Mean jet transport across line 5 for all five surveys was 6.3±0.9 $\times 10^6 m^3 s^{-1}$ (60% greater than the 500 m lnm value).

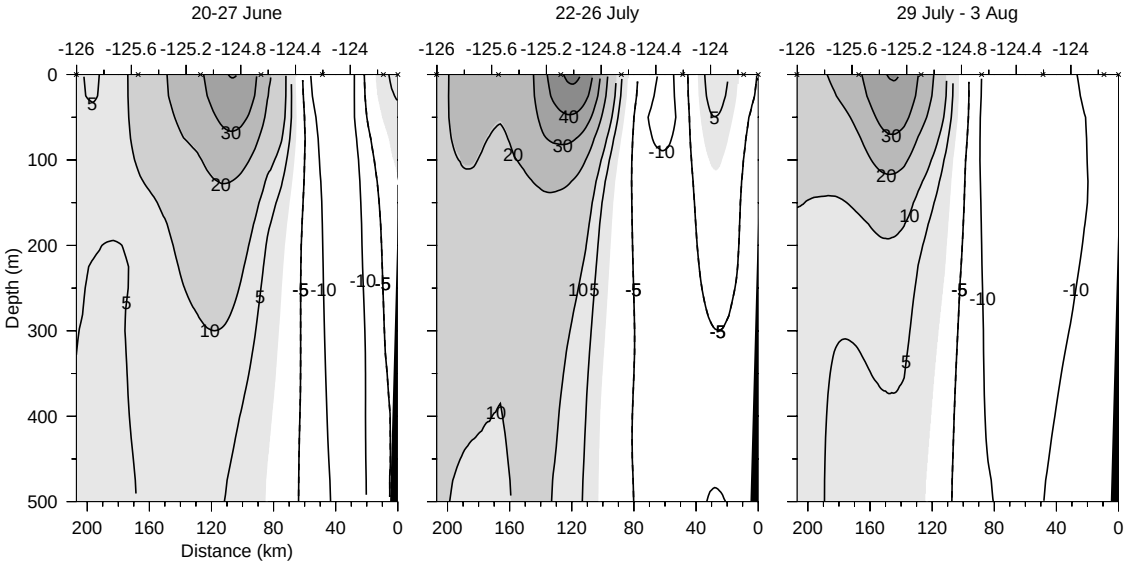

Fig. III.10 Vertical cross-sections of absolute geostrophic velocity (cm/s, equatorward shaded) across offshore-onshore line 5, in the middle of the grid at about 38.4°N.

III.5.3 D-line moored array

The moored array along the D-line (Figure III.1) measured currents that are consistent with results from the five hydrographic/ADCP surveys. The core of the jet comes closest to mooring D5/6 most of the time; maximum velocities are found here. The translation and rotation of the meandering jet past the fixed mooring leads to significant variability, however (Figure III.11). In general, a strong (about 60 cm/s at the surface) southwestward jet crosses the D-line from June to early July. Between July 12 and 17, the predominant direction of the current changes to roughly north-south (Huyer *et al.*, 1991). Note that the signature of the jet is still evident at 450 m, with speeds of about 5 cm/s.

The gray vectors in Figure III.11 are the absolute geostrophic velocities from the analysis of shipboard ADCP and CTD data from the five surveys. The agreement with the moored data is reasonably good, especially considering the variability present in the moored record and the length of time spent completing each survey. Jet strengths are comparable at each depth level, and the moored data provide independent confirmation of our finding that the jet signal is present at depth and that a 500 m lnm is not appropriate. The directional change of the jet is also remarkably consistent between the mooring and the survey results (Figure III.11).

III.6 Vertical velocities

One of the intriguing results of the CTZ program was the discovery by several independent methods that vertical velocities were larger than expected. In particular, subduction by O(10) m/d downward velocities within the jet produced anomalies at depth of hydrographic variables, chlorophyll, and radon, as summarized by Brink and Cowles (1991).

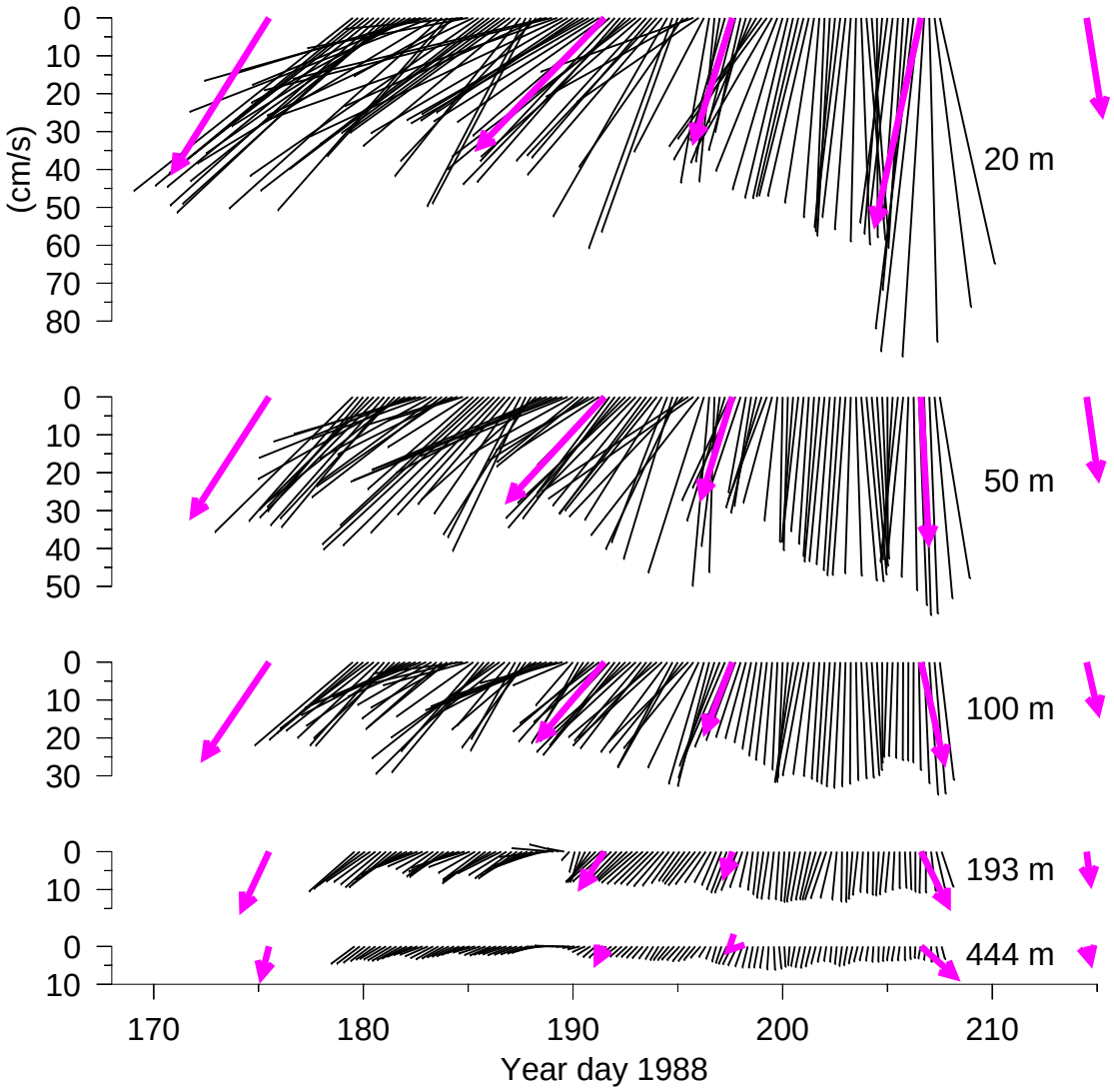

Fig. III.11 Low-passed velocity vectors from selected depths at mooring D5/6. The thicker gray vectors are from the analyses of shipboard ADCP and CTD data from the 20-27 June, 6-12 July, 13-18 July, 22-26 July, and 29 July - 3 August surveys; the vectors are drawn at the mid-point of each survey time period.

Dewey *et al.* (1991), using high-resolution repeated ADCP and microstructure sections along the D-line from 2-16 July when the jet was relatively stable, made estimates of each of the three terms which can contribute to *w*. They estimated that contributions to the mean vertical velocity were 80-90% along sloping isopycnals, 10-20% from isopycnal displacements, and 0-10% from diapycnal mixing.

Assuming flow along isopycnals, we interpolate absolute geostrophic **u** onto an isopycnal surface (σ_θ = 25.8). Then, by simple kinematics, vertical velocity on this surface is:

$$w = -\mathbf{u} \cdot \nabla z \quad , \tag{4}$$

where *z* is the depth of the isopycnal surface (e.g. one of the methods used by Leach, 1987). The resulting maps of *w* are consistent with previous CTZ studies in showing 10-20 m/d vertical velocities (Figure III.12). But they also reveal the spatial patterns of *w*, not available from the isolated studies of Dewey *et al.* (1991), Kadko *et al.* (1991), and Washburn *et al.* (1991).

The occurrence of *w* in 10−20 m/d patches of 20−30 km size is consistent with the short wavelength frontal instability mechanism identified by Barth (1994). Similar patterns of *w* were also obtained in a primitive equation modeling study of the CTZ region by Haidvogel *et al.* (1991). The net vertical subduction of a particle within the jet at 100 m depth (calculated by integrating changes in **u** and *w* along the 100 m isoline on the σ_θ=25.8 surface) can be as large as 90 m (Figure III.13). As pointed out by Shearman *et al.* (1998), the contradiction of following a water parcel at an assumed 100 m constant depth while discussing its vertical excursion is consistent with the quasi-geostrophic approximation, and appropriate in this context. The upwelling trend observed as we follow the 100 m streamline during the 6-12 July survey (Figure III.13) is consistent with the large scale anti-cyclonic bend which the jet is experiencing during this survey (Figure III.12); potential vorticity conservation implies that upwelling should be associated with an anti-cyclonic change in relative vorticity. Conversely, the sharp downwelling

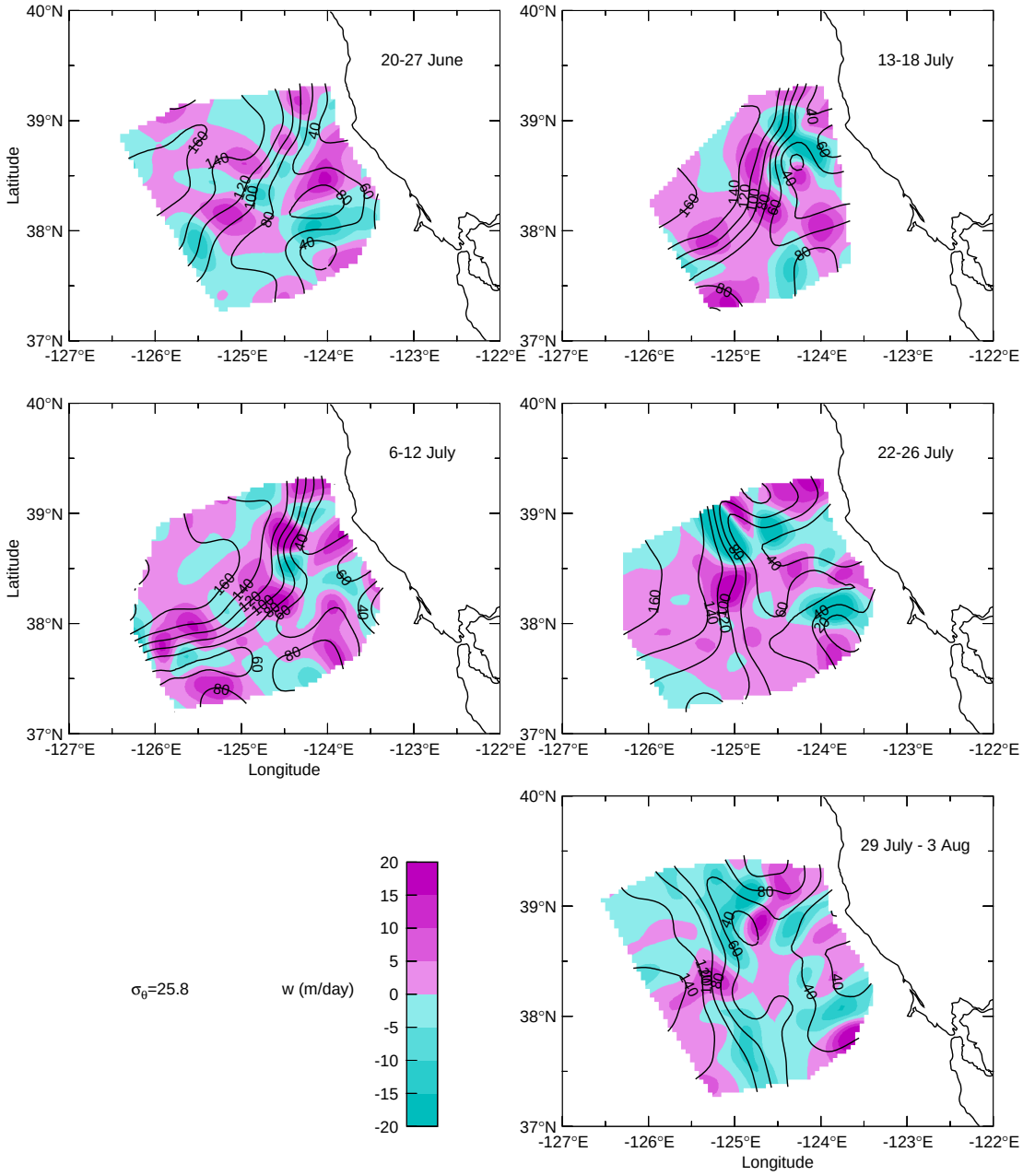

Fig. III.12 Vertical velocities on the σ_θ = 25.8 surface (image) and depth of this isopycnal (contours).

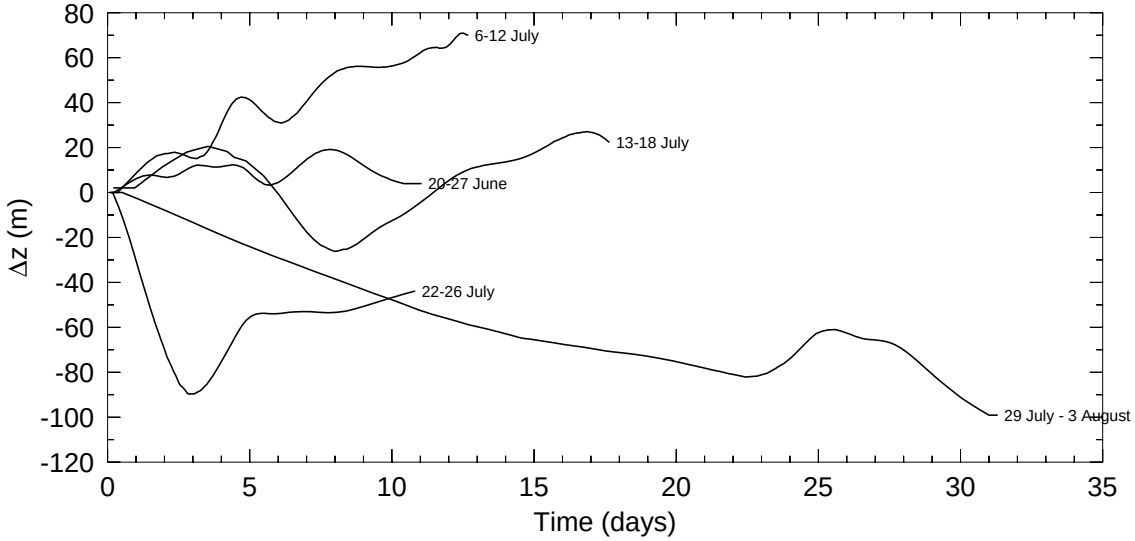

Fig. III.13 Net vertical displacements of flow along the 25.8 σ_θ surface at 100 m depth, for each survey. Time reference is not comparable between surveys (t=0 represents the beginning of the 100 m isoline at the north end of each survey).

initially observed in the 22-26 July case is associated with the strong cyclonic bend which the jet is experiencing as it enters the survey grid. During the 29 July - 3 August survey, along the offshore flank of the nearly straight jet, we observe a smaller but persistent downwelling tendency which leads to the largest net vertical subduction (Figure III.13).

Similar results were obtained by Hofmann *et al.* (1991), who studied simulated subsurface drifter tracks within the primitive equation model of Haidvogel *et al.* (1991). Over the course of the 30-day simulation, the drifters released at a depth of 90 m experienced vertical displacements of as much as 75 m upward and 120 m downward. Our results are similar, with a range of 70 m upward and 90 m downward (Figure III.13).

Our vertical velocity results are also in good general agreement with Shearman *et al.* (1998), who performed a careful diagnosis of vertical velocity using the Q-vector form of the quasi-geostrophic equation. They analyze high-resolution SeaSoar/ADCP data from the 1993 EBC program, at a location within a strong jet just offshore of our F line. Details differ, but we

both find maximum *w* of about 40 m/d, a background pattern consistent with potential vorticity conservation, and smaller scale *O* 10-20 m/d patches. We assumed that *w* is due only to advection along isopycnals (Eq. 4), while Shearman *et al.* (1998) do not. We interpret our agreement with them as additional evidence that advection along isopycnals is a reasonable assumption.

III.7 Summary

We have combined shipboard ADCP and CTD survey data to determine absolute quasi-geostrophic and mass-conserving horizontal velocities from 0-500 m depth. This method, similar to the one used by Rudnick (1996), significantly improves the description of the flow field off northern California during the June-August 1988 CTZ experiment. Mean equatorward volume transport of the mesoscale jet over the five surveys was $6.3 \pm 1.3 \times 10^6 m^3 s^{-1}$, and the maximum observed was $8.0 \times 10^6 m^3 s^{-1}$. The strength and deep (450 m) signature of the jet is confirmed by the CTZ moored array. We derive vertical velocity fields directly from the geostrophic horizontal velocities, assuming advection along isopycnal surfaces. Vertical velocities within the jet can be as large as 40 m/d, characterized by both 10-20 m/d patches of size 20-30 km and larger scale patterns.

III.8 References

Allen, J. S., L. J. Walstad, and P. A. Newberger, 1991: Dynamics of the coastal transition zone jet, 2. nonlinear finite amplitude behavior. *J. Geophys. Res.*, **96**, 14995-15016.

Allen, J. T. and D. A. Smeed, 1996: Potential vorticity and vertical velocity at the Iceland-Faeroes front. *J. Phys. Oceanogr.*, **26**, 2611-2634.

Bacon, S., 1994: Skill in an inversion solution: CONVEX-91 hydrographic results compared with ADCP measurements. *J. Atmos. Oceanic Technol.*, **11**, 1569-1591.

Barnes, S. L., 1994: Applications of the Barnes objective analysis scheme, part III: tuning for minimum error. *J. Atmos. Oceanic Tech.*, **11**, 1459-1479.

Barth, J. A., 1994: Short-wavelength instabilities on coastal jets and fronts. *J. Geophys. Res.*, **99**, 16095-16115.

Brink, K. H. and T. J. Cowles, 1991: The coastal transition zone program. *J. Geophys. Res.*, **96**, 14637-14647.

Candela, J., R. C. Beardsley, and R. Limeburner, 1992: Separation of tidal and subtidal currents in ship-mounted acoustic doppler current profiler observations. *J. Geophys. Res.*, **97**, 769-788.

Carter, E. F. and A. R. Robinson, 1987: Analysis models for the estimation of oceanic fields. *J. Atmos. Oceanic Technol.*, **4**, 49-74.

Chelton, D. B., R. A. deSzoeke, and M. G. Schlax, 1998: Geographical variability of the first baroclinic Rossby radius of deformation. *J. Phys. Oceanogr.*, **28**, 433-460.

Chereskin, T. K. and M. Trunnell, 1996: Correlation scales, objective mapping, and absolute geostrophic flow in the California current. *J. Geophys. Res.*, **101**, 22619-22629.

Cummins, P. F. and G. K. Vallis, 1994: Algorithm 732: solvers for self-adjoint elliptic problem in irregular two-dimensional domains. *ACM Trans. Math. Soft.*, **20**, 247-261.

Daley, R., 1991: *Atmospheric data analysis*, Cambridge.

Dewey, R. K., J. N. Moum, C. A. Paulson, D. R. Caldwell, and S. D. Pierce, 1991: *J. Geophys. Res.*, 14885-14907.

Haidvogel, D. B., A. Beckmann, and K. S. Hedstrom, 1991: Dynamical simulations of filament formation and evolution in the coastal transition zone. *J. Geophys. Res.*, **96**, 15017-15040.

Hawkins, H. F. and S. L. Rosenthal, 1965: On the computation of streamfunctions from the wind field. *Mon. Wea. Rev.*, **93**, 245-252.

Hofmann, E. E., K. S. Hedstrom, J. R. Moisan, D. B. Haidvogel, and D. L. Mackas, 1991: Use of simulated drifter tracks to investigate general transport patterns and residence times in the coastal transition zone. *J. Geophys. Res.*, **96**, 15041-15052.

Huyer, A., P. M. Kosro, J. Fleischbein, S. R. Ramp, T. Stanton, L. Washburn, F. P. Chavez, T. J. Cowles, S. D. Pierce, and R. L. Smith, 1991: Currents and water masses of the coastal transition zone off northern California, June to August 1988. *J. Geophys. Res.*, **96**, 14809-14831.

Huyer, A., J. A. Barth, P. M. Kosro, R. K. Shearman, and R. L. Smith, 1998: Upper-ocean water mass characteristics of the California current, summer 1993. *Deep-Sea Res.*. [in press.]

Kadko, D. C., L. Washburn, and B. Jones, 1991: Evidence of subduction within cold filaments of the northern California coastal transition zone. *J. Geophys. Res.*, **96**, 14909-14926.

Koch, S. E., M. DesJardins, and P. J. Kocin, 1983: An interactive Barnes objective map anlaysis scheme for use with satellite and conventional data. *J. Climate Appl. Met.*, **22**, 1487-1503.

Kosro, P. M., 1985: Shipboard acoustic current profiling during the Coastal Ocean Dynamics Experiment., UCSD Ph.D. thesis, SIO Ref. No. 85-8, University of California, La Jolla, Ca..

Kosro, P. M., A. Huyer, S. R. Ramp, R. L. Smith, F. P. Chavez, T. J. Cowles, M. R. Abbott, P. T. Strub, R. T. Barber, P. Jessen, and L. F. Small, 1991: The structure of the transition zone between coastal waters and the open ocean off northern California, winter and spring 1987. *J. Geophys. Res.*, **96**, 14707-14730.

Large, W. G. and S. Pond, 1981: Open ocean momentum flux measurements in moderate to strong winds. *J. Phys. Oceanogr.*, **11**, 324-336.

Leach, H., 1987: The diagnosis of synoptic-scale vertical motion in the seasonal thermocline. *Deep-Sea Res.*, **34**, 2005-2017.

Munk, W., F. Snodgrass, and M. Wimbush, 1970: Tides offshore, transition from California coastal to deep-sea waters. *Geophys. Fluid Dyn.*, **1**, 161-235.

Noble, M., L. K. Rosenfeld, R. L. Smith, J. V. Gardner, and R. C. Beardsley, 1987: Tidal currents seaward of the northern California continental shelf. *J. Geophys. Res.*, **92**, 1733-1744.

Pierce, S. D., J. S. Allen, and L. J. Walstad, 1991: Dynamics of the coastal transition zone jet: 1. linear stability analysis. *J. Geophys. Res.*, **96**, 14979-14993.

Pollard, R. T. and L. A. Regier, 1992: Vorticity and vertical circulation at an ocean front. *J. Phys. Oceanogr.*, **22**, 609-625.

Rudnick, D. L., 1996: Intensive surveys of the Azores front, 2. inferring the geostrophic and vertical velocity fields. *J. Geophys. Res.*, **101**, 16291-16303.

Shearman, R. K., J. A. Barth, and P. M. Kosro, 1998: Diagnosis of the three-dimensional circulation associated with mesoscale motion in the California current. *J. Phys. Oceanogr.*. [in press.]

Torgrimson, G. M. and B. M. Hickey, 1979: Barotropic and baroclinic tides over the continental slope and shelf off Oregon. *J. Phys. Oceanogr.*, **9**, 945-961.

Walstad, L. J., J. S. Allen, P. M. Kosro, and A. Huyer, 1991: Dynamics of the coastal transition zone jet through data assimilation studies. *J. Geophys. Res.*, **96**, 14959-14977.

Washburn, L., D. C. Kadko, B. H. Jones, T. Hayward, P. M. Kosro, T. P. Stanton, S. Ramp, and T. Cowles, 1991: Water mass subduction and the transport of phytoplankton in a coastal upwelling system. *J. Geophys. Res.*, **96**, 14927-14946.

IV. Near-inertial oscillations in an eastern boundary current jet

IV.1 Abstract

The 1988 Coastal Transition Zone experiment observed a strong mesoscale equatorward jet in an eastern boundary current system. This jet was about 50 km wide, with core velocities > 0.7 ms^{-1}, and extended down to below 500 m. From 2-16 July 1988, the jet was relatively stable and headed south-southwest across a moored current meter array. Repeated shipboard ADCP sections were also made along the line of moorings. On average during this two week period, the southern mooring was in the cold flank of the jet, experiencing strong cyclonic shear, while the mooring 50 km north was on the warm side of the jet experiencing anticyclonic shear. The effective inertial frequency $f_{eff} = f + \gamma/2$, where γ is local horizontal shear, was shifted up to $1.1f$ on the cold side and down to $0.95f$ on the warm side of the jet. Analysis of band-passed near-inertial currents measured by the moorings reveals amplified inertial energy in the region with lower f_{eff}, consistent with the trapping and amplification of inertial oscillations predicted for such regions. Several near-inertial packets of energy connected with wind stress events appear to travel downward slowly to at least 200 m depth. Observed inertial amplitudes are about 15 cm/s at the surface and 5 cm/s at 450 m.

IV.2 Introduction

In this note, we examine current meter data for evidence that inertial oscillations within an eastern boundary current jet are affected by interaction with the jet's vorticity γ; the effective inertial frequency due to this interaction will be $f_{eff} = f + \gamma/2$ (Kunze, 1985). The 2-16 July mean jet crossed nearly normal to the D-line and the array of three moorings was well situated to capture the jet (Figure IV.1a). This mean jet velocity section was calculated from 16 repeated ADCP sections up and down the D-line, as thoroughly analyzed by Dewey *et al.* (1991). Values of f_{eff} calculated from this mean jet (Figure IV.1b) show clearly that mooring D5/6 is within a region of low f_{eff}, while D7/8 is experiencing high f_{eff}.

IV.3 Data

Low-passed (<0.6 cpd) six-hourly vector time series of wind stress were calculated from R/V *Wecoma* 2-23 July meteorological measurements, using the formulae of Large and Pond (1981). The *Wecoma* was steaming up and down the D-line during this period.

The CTZ 1988 three primary current meter moorings were deployed 21-26 June and recovered 27-29 July. One mooring (D6/7) had Aanderaa currents meters at nominal 90, 140, 190, and 430 m depths. Two moorings (D5/6 and D7/8) had 307 kHz upward-looking RDI ADCPs at about 120 m (20-115 m range) and Aanderaas at 120, 150, 200, and 450 m. Low-pass filtered versions of the time series are in Dewey *et al.* (1991) or Huyer *et al.* (1991).

Here our interest is in the near-inertial frequency band. To proceed, we apply a time domain band-pass filter. We require a particularly sharp filter, since the local inertial period (19.3 h) is particularly close to the nearest diurnal tidal peak, K_1 at 23.9 h. We also wish to allow for shifted inertial frequencies, not wanting to suppress them; this requires an even

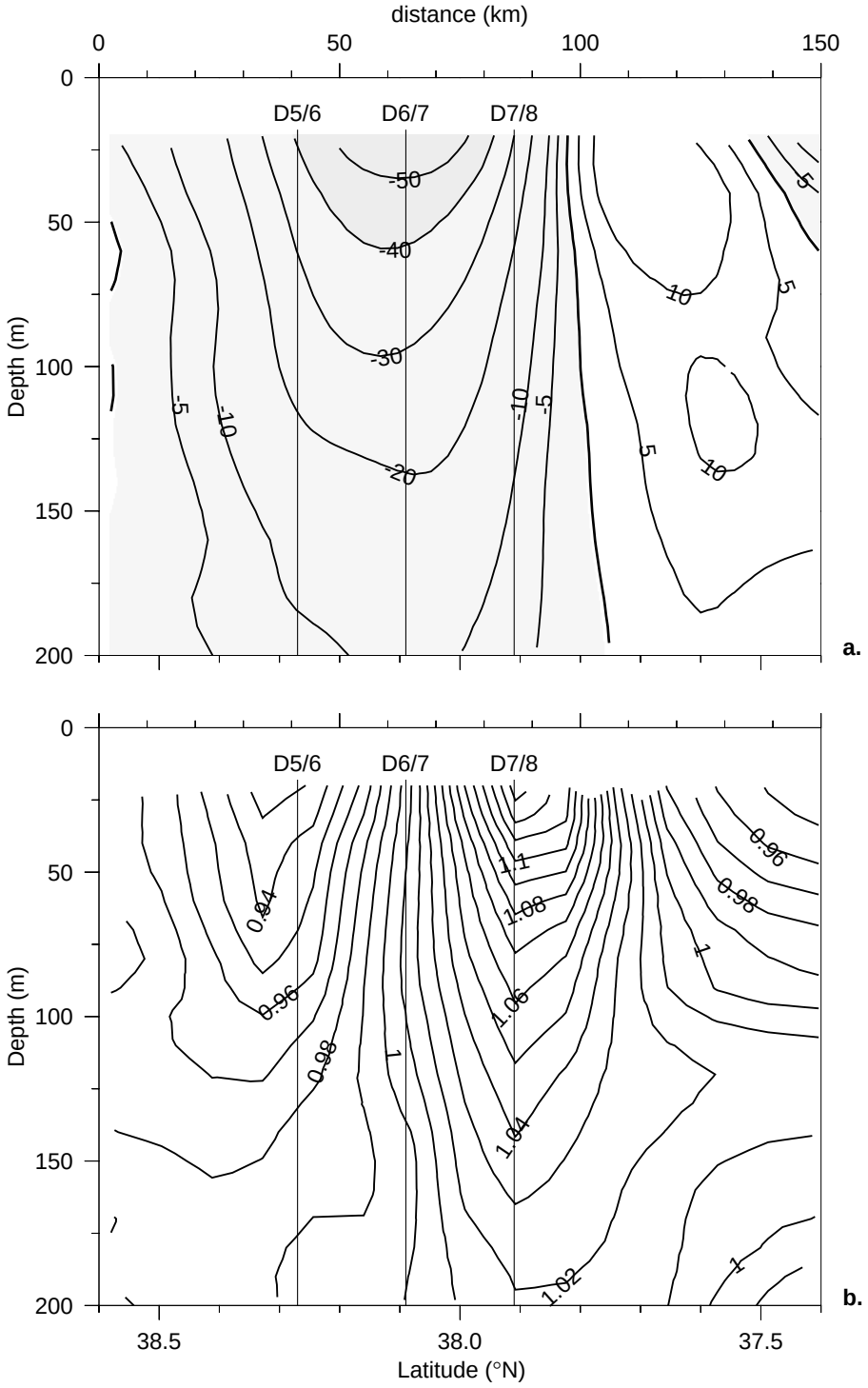

Fig. IV.1 The 2-16 July mean cross-track jet velocity from repeated shipboard ADCP (a) and corresponding f_{eff} calculated from it (b).

sharper transition.

We design a bandpass finite impulse response filter using the Parks-McClellan equiripple method (Figure IV.2). This method, in common use by electrical engineers for years, is more effective than conventional window-based filter designs in producing a desired frequency response with minimum filter length (Parks and Burrus, 1987). Minimum filter length is particularly important in this case, to minimize losses at the ends of our relatively short record. We design a filter with amplitude response within 1% of unity from 0.95-1.15 f, while K_1 and all other bands are sufficiently suppressed (Figure IV.2). Total filter length was 120 h.

Application of the filter reveals near-inertial currents within the jet of *O* 15 cm/s at the surface (Figures IV.3, IV.4). Amplitudes decrease with depth, but can still be as large as 5 cm/s at 200 m.

IV.4 Discussion

The largest wind stress event at around 18 July is clearly associated with the surface packet of near-inertial motion at D5/6, which develops with about a one day lag behind the wind. D5/6 at the surface appears to respond to several wind stress events throughout the period. At D7/8, however, the response is reduced. This pattern of enhanced response at D5/6 and reduced at D7/8 is consistent with trapping of near-inertial energy in the trough of low f_{eff} and exclusion from the peak of high f_{eff} (Kunze, 1985).

Over the 2-16 July period, the mean clockwise-rotating amplitude also shows enhancement at D5/6 (Figure IV.5a.). The near-inertial frequency peaks (which we locate by maximizing the clockwise component amplitude) at D7/8 show an increase up to 1.04 f at the surface (Figure IV.5c), which is not as large as expected from the background shear (Figure IV.1b).

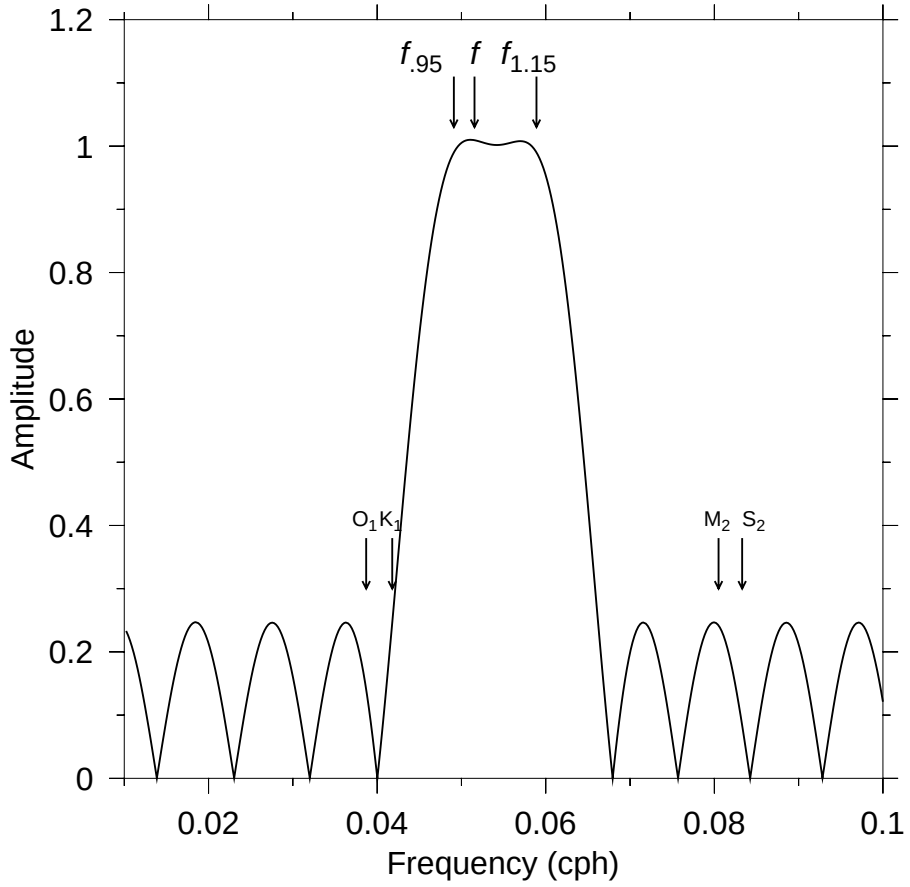

Fig. IV.2. Amplitude response of the designed band-pass filter using the Parks-McClellan equiripple method.

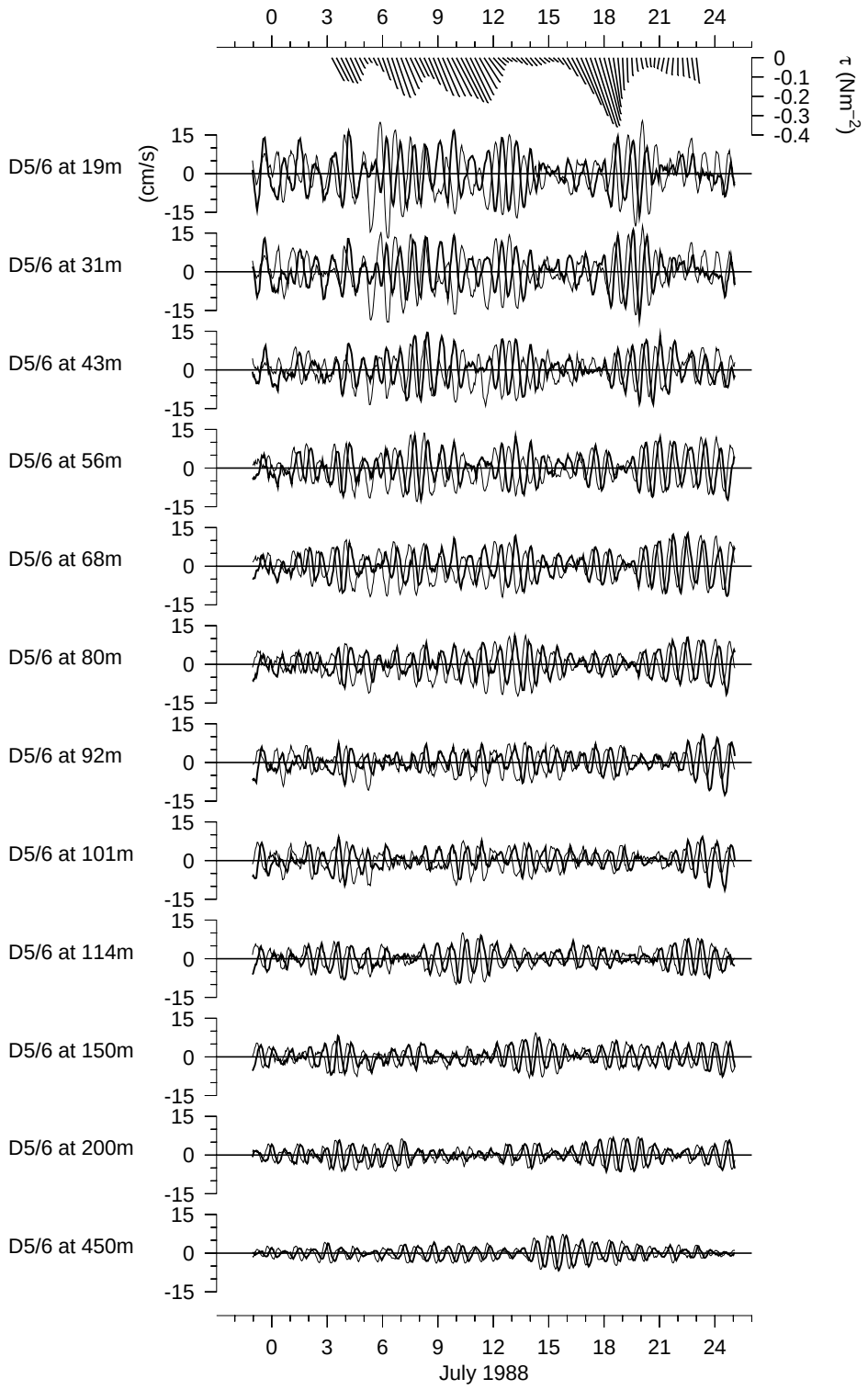

Fig. IV.3. Band-pass filtered near-inertial *u*(bold) and *v* at mooring D5/6; top panel has wind stress vectors.

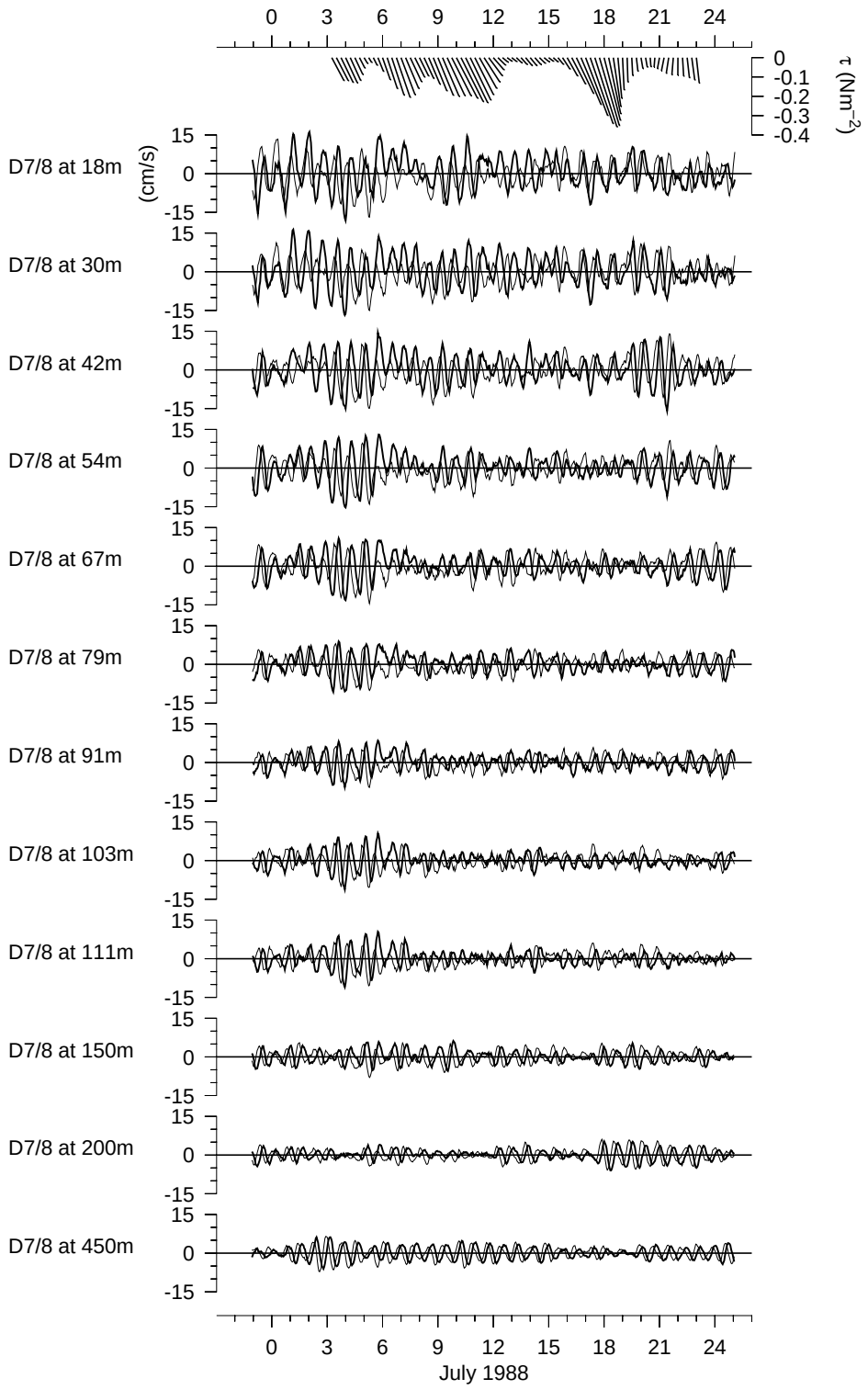

Fig. IV.4. Band-pass filtered near-inertial *u*(bold) and *v* at mooring D7/8; top panel has wind stress vectors.

Uncertainties in the frequency determination are large, however (Figure IV.5d).

Finally, this note was partially motivated by interest in the effects of near-inertial energy as a *noise* component from the point of view of mesoscale studies such as Chapter III. For example, when making use of ADCP measurements to reference geostrophy, the packets seen in Figures IV.3,4 remind us that the ADCP may be affected by unknown inertial signals. As Rudnick (1996) mentions, choosing a deeper level of data is not necessarily a better choice for reducing noise, and we see evidence of this in the similar sizes of inertial packets from 100 to 450 m (Figure IV.3). The advantage of using ADCP over a range of depths is that the inertial packets eventually will lack vertical coherence, so will tend to average out.

IV.5 References

Dewey, R. K., J. N. Moum, C. A. Paulson, D. R. Caldwell, and S. D. Pierce, 1991: *J. Geophys. Res.*, 14885-14907.

Huyer, A., P. M. Kosro, J. Fleischbein, S. R. Ramp, T. Stanton, L. Washburn, F. P. Chavez, T. J. Cowles, S. D. Pierce, and R. L. Smith, 1991: Currents and water masses of the coastal transition zone off northern California, June to August 1988. *J. Geophys. Res.*, **96**, 14809-14831.

Kunze, E., 1985: Near-inertial wave propagation in geostrophic shear. *J. Phys. Oceanogr.*, **15**, 544-565.

Large, W. G. and S. Pond, 1981: Open ocean momentum flux measurements in moderate to strong winds. *J. Phys. Oceanogr.*, **11**, 324-336.

Parks, T. W. and C. S. Burrus, 1987: *Digital filter design*, Wiley, New York.

Rudnick, D. L., 1996: Intensive surveys of the Azores front, 2. inferring the geostrophic and vertical velocity fields. *J. Geophys. Res.*, **101**, 16291-16303.

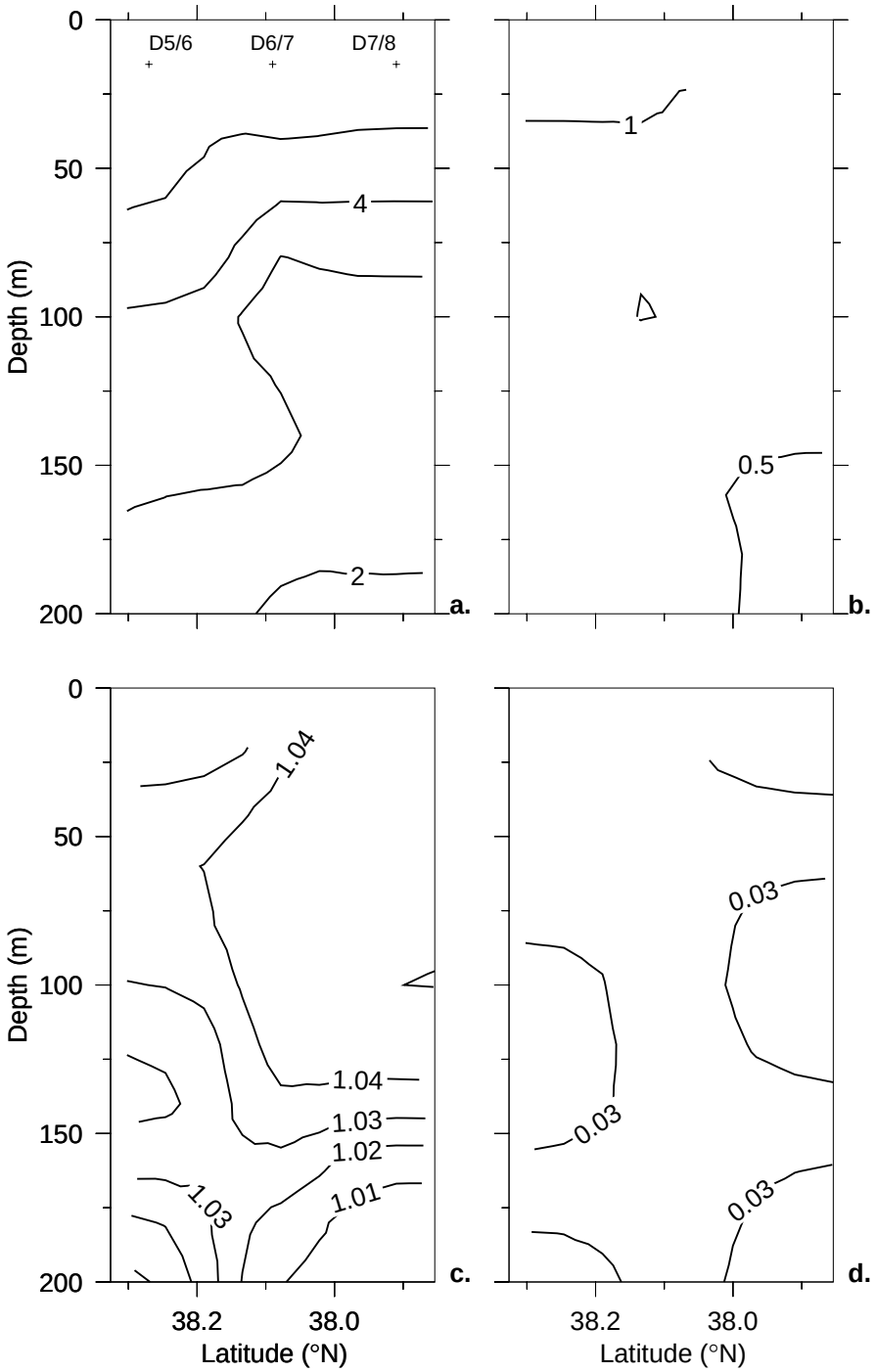

Fig. IV.5. From current meter data, the 2-16 July mean clockwise component near-inertial amplitude in cm/s (a) with uncertainty (b) and the corresponding frequency in units of f (c) with uncertainty (d).

V. Dynamics of the Coastal Transition Zone Jet: 1. Linear Stability Analysis

Stephen D. Pierce
J. S. Allen
Leonard J. Walstad

College of Oceanic and Atmospheric Sciences
104 Ocean Admin Bldg, Oregon State University, Corvallis, OR, 97331-5503

Published in: *Journal of Geophysical Research*
Coastal Transition Zone Special Issue
Volume 96, No. C8, pp. 14979-14993

Reprinted by permission

V.1 Abstract

The linear stability of a coastal transition zone (CTZ) jet is analyzed using a six-layer quasi-geostrophic model with observed basic state velocity profiles. The velocity profiles are obtained from objectively analyzed hydrographic and acoustic Doppler data from the 1987 CTZ pilot experiment. Along-jet perturbation wavelengths of 260-265 km are found to be the most unstable, with *e*-folding growth periods of 7-11 days and along-jet phase speeds of 4-8 km/d downstream. Energy transformation terms and energy budgets are discussed. Both barotropic and baroclinic instability processes are important.

V.1 Introduction

The dynamics of the transition zones between open ocean and upwelling regions along eastern ocean boundaries are not well understood. The northern California example of a coastal transition zone (CTZ), with its intriguing filaments or jets, has recently been the subject of a major observational effort (CTZ Group, 1988). In the late spring and summer of 1987, two hydrographic and shipboard acoustic Doppler current profiler (ADCP) surveys revealed an intense equatorward jet along the boundary between cool and saline upwelled water and warmer, fresher offshore water (Kosro *et al.*, 1991) The presence of this mesoscale jet with energetic meanders anywhere from 100 to 400 km in size is by now an expected feature of this region and season (Strub *et al.*, 1991; Huyer *et al.*, 1991). Some of the dynamical questions suggested by these observations involve the nature and structure of these jet meanders. Why does a meander grow? What determines its wavelength? If the growth can be explained as an instability, what source of energy feeds the instability? These questions may be approached in a variety of ways.

Walstad *et al.* (1991) take advantage of the combination of hydrographic and ADCP data from the 1987 experiment to perform quasi-geostrophic data assimilation studies. Initial conditions are specified by objective analysis of the May 22 data set. The model is time-stepped forward to June 12 using boundary conditions obtained by linear interpolation between the May 22 and June 12 observations. The four-dimensional field estimate of the flow is obtained by varying the objective analysis parameters until the final June 12 quasi-geostrophic solution is in best agreement with the observed June 12 field. The agreement is fairly good [see Walstad *et al.* (1991) for details]. The structure and energetics of the solution are then analyzed.

The present study (part 1) regards a jet meander as a possible linear instability of a quasi-geostrophic basic state flow. We consider two-dimensional velocity sections of the jet extracted

from the objectively analyzed May 22 and June 12, 1987, data sets as the basic states for the stability analyses. The formulation allows for both barotropic and baroclinic instability processes. We obtain phase speeds, growth rates, and modal structure of the perturbations as a function of along-jet wavelength. In addition, we examine the transformation of kinetic and potential energy to the perturbations, presenting integrated energy budgets and maps of the relevant terms in the quasi-geostrophic energy balance.

In part 2, Allen *et al.* (1991) continue the stability study by examining the nonlinear, finite amplitude behavior of the CTZ jet. One of the basic state profiles we analyze here in part 1 is used as an initial condition for a time-dependent, nonlinear quasi-geostrophic model in a periodic f plane channel. The jet structure is perturbed and the evolution of the stream function, vertical velocity, vorticity, and potential vorticity fields is examined. Some of the results presented in part 2 use the most unstable linear mode found in part 1 to perturb the nonlinear model. The contributions of different terms to the kinetic and potential energy balances are also assessed in part 2.

Although the literature involving studies of the stability of mean flows is extensive, historically the majority of it concentrates on one-dimensional cases, i.e., either pure baroclinic or pure barotropic instabilities. This is not surprising since the two-dimensional case is difficult analytically [Pedlosky (1987) section 7.15]; the normal-mode equation is nonseparable. With increasing computer capabilities, however, numerical solutions have become viable. Important idealized studies of the mixed stability problem include Hart (1974) and Holland and Haidvogel (1980), which each explore parameter space using specific two-layer idealized mean state profiles. Killworth (1980) offers a less in-depth but broader overview of the mixed stability of many different idealized profiles. The present work in some ways builds upon Haidvogel and Holland (1978), who analyze the mixed stability of profiles obtained from general circulation

model output; we extend their two-layer model to an arbitrary number of layers (six for our standard case).

The emphasis of the present study is on the use of specific observed basic state profiles to produce results relevant to the CTZ region. Although Johns (1988) does not treat the mixed stability case, his pure baroclinic study of Gulf Stream meanders using actual data is similar to our approach. Beckmann (1988), who treats the mixed instability case for jet modes in the eastern North Atlantic, also uses methods similar to the present study.

V.2 Observed jet

Kosro *et al.* (1991) provide a complete description of the late spring and summer (May 18-27 and June 9-19) 1987 surveys; only a brief overview of the data relevant to this study is given here. The nominal station grid for the surveys consists of two alongshore lines about 90 and 150 km from the coast, connected by four cross-shore lines to form three subgrids with approximately 15-km station spacing. Hydrographic data to at least 495 m depth were collected at 76 stations for each survey, and good quality acoustic Doppler current profiler (ADCP) data were collected continuously along the shiptrack.

ADCP data at 121 m are used by Walstad *et al.* (1991) to reference the hydrographic measurements, thus determining the absolute geostrophic flow field for the upper 500 m along the station grid. We utilize the objective analysis of this combined data set as presented by Walstad *et al.* (1991). This method includes extrapolation of both the density and the velocity fields below 500 m using historical data and the first baroclinic mode. For each of the surveys, the correlation function for the objective analysis is assumed independent of time and an estimate of the density and velocity fields is made for the midpoint of the cruise: May 22 and June 12. The

reader is referred to Walstad *et al.* (1991) for the details and approximations inherent in these techniques. Examples of the resulting stream function fields, at 50 m depth, are shown in Figure V.1.

For the purpose of our stability analysis, we extract one two-dimensional vertical section of the flow field from each survey and use this as our basic state. The locations of these sections (Figure V.1) are chosen subjectively, with an eye toward catching the jet where it is least affected by other phenomena such as eddies. Ideally, we want to choose a place where the jet does not seem to be part of a mature meander. It is debatable within linear stability theory whether it is more appropriate to use "snapshots" such as these or some type of observational mean for the basic state profiles. Although some sort of average might seem more relevant than a local calculation at one point in the jet, this average will not necessarily be related to the theoretical unperturbed form of the flow. As discussed by Pedlosky (1987), any real time average will be affected by the very perturbations which we seek to study. Our choice is to make a best guess at the structure of a fluctuation-free jet and to use this as our "mean" state. The paradigm of this flow field as a mean jet plus a perturbation seems justified a posteriori by nonlinear results from part 2, which reveal a jet retaining much the same form as the unperturbed flow even through the course of large meanders.

We examine the stability of the observed jet profiles over a flat bottom, without complicating effects from bottom topography. Although the CTZ region is located adjacent to the continental slope, where bottom topography may affect the dynamics, observations of the jet location during 1987 indicate that the core of the jet was mostly found offshore of the continental slope Kosro *et al.* (1991). Within the analysis region used by Walstad *et al.* (1991), the northeastern corner of the grid does include a narrow strip of the outer continental slope region. Yet the remainder of the region does not contain substantial topography. Since the time-dependent jet is

Fig. V.1. Stream function at 50 m from objective analysis of combined hydrographic and ADCP data from the late spring and summer 1987 surveys (Walstad *et al.*, 1991). The contour interval is equivalent to 2 dynamic cm. The two lines drawn between small circles indicate locations of the vertical sections extracted for the stability analyses.

constantly altering its orientation with respect to the local bottom topography, it is difficult to specify an appropriate mean relative position. In addition, recall that we do not have CTZ observations available below 500 m depth. The stream function values below this point are obtained using extrapolation and available historical data and are consequently not well determined. We feel that these uncertainties preclude the specification of bottom topography in a meaningful manner. Thus we assume a flat bottom for this initial analysis.

V.3 Linear stability model

V.3.1 Formulation

The linear stability model follows the development by Haidvogel and Holland (1978) extended to an arbitrary number of layers. Consider a quasi-geostrophic model with N layers of constant density ρ_n and undisturbed layer thicknesses H_n, where $n = 1, 2, \ldots, N$ ($n = 1$ is the surface layer). The subscript $n + 1/2$ denotes a variable defined at the interface between layers n above and $n+1$ below. The stream function for each layer is $\psi_n = \psi_n(x, y, t)$ and the geostrophic velocity components are

$$u_n = -\psi_{ny} , \qquad v_n = \psi_{nx} , \tag{1}$$

where (x, y) are Cartesian coordinates, t is time, and subscripts (x, y, t) denote partial differentiation. Consider the inviscid quasi-geostrophic vorticity and density equations, on an f plane, in terms of the stream function ψ_n for layers $n = 1, N$:

$$\nabla^2\psi_{nt} + J(\psi_n, \nabla^2\psi_n) + f_0 H_n^{-1}(w_{n+1/2} - w_{n-1/2}) = 0 , \tag{2}$$

$$(\psi_n - \psi_{n+1})_t = J(\psi_n - \psi_{n+1}, \psi_{n+1/2}) - g'_{n+1/2} f_0^{-1} w_{n+1/2} , \tag{3}$$

where $$\psi_{n+1/2} = \frac{H_{n+1}}{H_n + H_{n+1}}\psi_n + \frac{H_n}{H_n + H_{n+1}}\psi_{n+1} , \tag{4}$$

and H_n is layer thickness (total depth $H = H_1 + H_2 + \cdots H_N$), $g'_{n+1/2} = g(\rho_{n+1} - \rho_n)/\rho_0$ is reduced gravity, f_0 is the Coriolis parameter, and J is the Jacobian operator. Vertical boundary conditions are $w_{1/2} = w_{N+1/2} = 0$ at $z = 0, -H$.

Combine (2) and (3) to form equations for potential vorticity conservation; for the top layer,

$$\frac{D_1}{Dt}\ \{\ \nabla^2\psi_1 + \frac{H}{H_1}\ F_1[\psi_2 - \psi_1]\} = 0\ , \tag{5a}$$

for $n = 2, (N-1)$:

$$\frac{D_n}{Dt}\ \{\ \nabla^2\psi_n + \frac{H}{H_n}\ [F_n(\psi_{n+1} - \psi_n) - F_{n-1}(\psi_n - \psi_{n-1})]\} = 0\ , \tag{5b}$$

and for the bottom layer,

$$\frac{D_N}{Dt}\ \{\ \nabla^2\psi_N - \frac{H}{H_N}\ F_{N-1}[\psi_N - \psi_{N-1}]\} = 0\ , \tag{5c}$$

where $F_n = f_0^2/g'_{n+1/2}H$ and $\frac{D_n}{Dt} = \frac{\partial}{\partial t} + u_n\frac{\partial}{\partial x} + v_n\frac{\partial}{\partial y}$.

To simplify the stability problem to a tractable one, we assume that the basic state flow is two-dimensional and independent of time. Consider a channel of width L with coordinates (x, y) along-channel and cross-channel, respectively, and ψ_n as the basic mean state $\Psi_n(y)$ plus a small perturbation $\gamma\,\phi_n(x, y, t)$, i.e. $\psi_n = \Psi_n(y) + \gamma\,\phi_n(x, y, t)$, where $\gamma \ll 1$. Linearize (5b) about the basic state in the usual way:

$$\begin{aligned}(\frac{\partial}{\partial t} + U_n\frac{\partial}{\partial x})\{\nabla^2\phi_n + \frac{H}{H_n}\ [F_n(\phi_{n+1} - \phi_n) - F_{n-1}(\phi_n - \phi_{n-1})]\}\\ - \phi_{nx}\{U_{nyy} + \frac{H}{H_n}\ [F_n(U_{n+1} - U_n) - F_{n-1}(U_n - U_{n-1})]\} = 0\ ,\end{aligned} \tag{6}$$

where $U_n = -\Psi_{ny}$. Equations (5a) and (5c) are linearized in similar fashion. In subsequent equations, the range of $n = 1, N$ and the simplified formulations for the $n = 1$ and $n = N$ cases will be implicit.

We consider solutions to (6) of the form

$$\phi_n = \mathrm{Re}[\hat{\phi}_n(y)e^{ik(x-ct)}] \,, \tag{7}$$

where the wavenumber k is taken to be real, but c and $\hat{\phi}_n$ are complex. Substitution into (6) yields

$$(U_n - c)\{\hat{\phi}_{nyy} - k^2\hat{\phi}_n + \frac{H}{H_n}[F_n(\hat{\phi}_{n+1} - \hat{\phi}_n) - F_{n-1}(\hat{\phi}_n - \hat{\phi}_{n-1})]\}$$

$$- \hat{\phi}_n\{U_{nyy} + \frac{H}{H_n}[F_n(U_{n+1} - U_n) - F_{n-1}(U_n - U_{n-1})]\} = 0 \,. \tag{8}$$

For the domain $0 < y < L$, the boundary conditions for (8) are $\hat{\phi}_n(0) = \hat{\phi}_n(L) = 0$, forming an eigenvalue problem for $\hat{\phi}_n$ with eigenvalue c. For $c = c_r + ic_i$, solutions with $c_i > 0$ indicate temporal instability with exponential growth rate kc_i.

Using a centered second-order finite difference approximation in y, we solve the above problem numerically. Defining $\hat{\phi}_{n,j}$ as $\hat{\phi}$ of the nth layer at the jth grid point in y, we form the generalized complex eigenvalue problem,

$$c\mathbf{A}\bar{\phi} = \mathbf{B}\bar{\phi} \,, \tag{9}$$

where $\bar{\phi}$ is the eigenvector composed of $\hat{\phi}_{n=1,\,N;\,j=1,\,M}$ and $\mathbf{A}$ and $\mathbf{B}$ are $NM \times NM$ matrices of coefficients. Equation (9) can be solved using an algorithm by Kaufman (1975), or a slightly modified IMSL version (routine *gvccg*). For a given basic state flow, we seek solutions for the eigenvalue c and eigenvector structure $\hat{\phi}$ over a range of wavenumbers k. The algorithm was verified through reproduction of stability results from Killworth (1980) and Holland and Haidvogel (1980)

Walstad *et al.* (1991) choose a six-layer scheme to resolve the vertical; we use the same for consistency, although we later investigate the effect of increasing the number of layers (see section 6). Both the May 22 and June 12 standard six-layer basic states use the same values for layer depths and reduced gravities (Table V.1 and Figure V.2). The model N^2 profile is also

shown (Figure V.2*a*), $N^2 = g'_{n+1/2}/(z_n - z_{n+1})$, where z_n is the mid-depth of layer n. The two basic states in Figure V.2 are similar, although the June 12 jet is more intense than the May 22 one, with maximum speeds ≈ 0.9 m s^{-1} rather than ≈ 0.5 m s^{-1}. The two cases provide a useful range within which most examples of a jet would probably lie. We concentrate on the results from the May 22 case since the smaller values of horizontal and vertical shear are less likely to give overestimates of instability processes for the jet in general.

Local Rossby numbers U_y/f calculated across the jet reach maximums of about 0.2; this is within the range where quasi-geostrophic dynamics remains a useful approximation. The first baroclinic Rossby radius of deformation calculated from the six-layer observed jet is $R_d = 24.6$ km. To estimate cross-jet length scales, we fit a Gaussian analytical form $U = U_0 \exp(-y^2/L^2)$ to the horizontal profiles (Figures V.2*b* and V.2*c*, dashed lines) and obtain an estimate of $L = 29 \pm 1$ km (half width). Since the ratio R_d/L ~ O(1), parameter studies such as Killworth (1980) predict the possibility of mixed instability.

The linear stability analysis uses 175 km for the model channel width. Figures V.2, V.12, and V.14 indicate this 175-km-wide channel. Figures V.6-V.9 show a jet centered within a wider 350-km region. The wider channel is shown for clarity and for consistency with the presentation of some of the finite amplitude results of part 2; all of our results in part 1 are calculated using a 175-km channel width. Model grid spacing across the channel is 5 km, resulting in 36 grid points in the across-channel coordinate y. The tails of the velocity profiles (10-15 km in length) at the y boundaries were smoothed exponentially to zero. Experimentation with doubling the horizontal resolution in y did not change the results substantially; results for the maximum growth rate of the fluctuation were within 1% of the basic case. We also investigated the effects of using a full 350-km-wide channel for selected cases, and the results were not

Fig. V.2. Standard six-layer basic state profiles: (*a*) layer thicknesses and N^2 profile, which are the same for both cases; (*b*) May 22 and (*c*) June 12 velocity profiles versus cross-jet distance y for layers 1-6; and (*d*) velocity profiles vs. depth at the core of the jet ($y = 85$ km). The dashed lines which nearly coincide with the layer 1 profiles in Figures V.2*b* and V.2*c* are Gaussian fits to the horizontal jet. These are examples of the fits used to estimate a cross-jet length scale (half width) of $L = 29 \pm 1$ km.

Table V.1. Six-Layer Basic State Characteristics

Layer	Thickness, m	$g\Delta\rho/\rho_0$, m s^{-2}
1 (surface)	100	
		1.0655×10^{-2}
2	100	
		3.3704×10^{-3}
3	100	
		3.6904×10^{-3}
4	400	
		4.6926×10^{-3}
5	800	
		3.9488×10^{-3}
6 (bottom)	1672	

The Rossby radius for the first baroclinic mode, $R_d = 24.6$ km.

qualitatively different. As expected [e.g Beckmann (1988).], the increased cross-jet scale allowed for slightly (≈5%) larger growth rates. For simplicity and computational efficiency, we retain our choice of the 175-km-wide region.

V.3.2 Energetics

The energetics governing the growth of a perturbation in a current with both vertical and horizontal shear, as in the present case, are especially interesting. The energy transformations of both barotropic and baroclinic instability processes are occurring simultaneously; even the signs of the energy terms will be uncertain a priori, as discussed by Pedlosky (1987).

We derive the quasi-geostrophic kinetic energy balance for the perturbations by multiplying (6) by $-\phi_n H_n$ and rearranging terms to yield

$$\frac{1}{2} H_n(\nabla\phi_n \cdot \nabla\phi_n)_t = H_n\nabla\cdot(\phi_n\nabla\phi_{nt}) + H_n\Psi_{ny}\frac{1}{2}(\nabla\phi_n\cdot\nabla\phi_n)_x$$

$$- H_n\phi_{nx}\phi_{ny}\Psi_{nyy} + H_n\nabla\cdot[-\phi_n\Psi_{ny}(\nabla\phi_n)_x + \phi_n\phi_{nx}\Psi_{nyy}\hat{j}]$$

$$- f_0\, w_{n-1/2}\,\phi_{n-1/2} + f_0\, w_{n+1/2}\,\phi_{n+1/2}$$

$$+\left[f_0 \frac{H_n}{H_n+H_{n+1}} w_{n+1/2}(\phi_n - \phi_{n+1}) + f_0 \frac{H_n}{H_n+H_{n-1}} w_{n-1/2}(\phi_{n-1} - \phi_n)\right] . \tag{10}$$

The potential energy equation is derived in a similar fashion. Multiplying (3) by $f_0(\phi_n - \phi_{n+1})$ and rearranging terms, at the $n + 1/2$th interface we obtain

$$\left[\frac{1}{2} \frac{f_0^2}{g'_{n+1/2}} (\phi_n - \phi_{n+1})^2\right]_t = \left[\frac{1}{2} \frac{f_0^2}{g'_{n+1/2}} (\phi_n - \phi_{n+1})^2\right]_x \Psi_{n+1/2\ y}$$

$$- \frac{f_0^2}{g'_{n+1/2}} (\phi_n - \phi_{n+1})(\Psi_n - \Psi_{n+1})_y \phi_{n+1/2\ x} - f_0 w_{n+1/2}(\phi_n - \phi_{n+1}) . \tag{11}$$

In Table V.2 we briefly interpret and label symbolically the terms in the energy balances (10) and (11), following for the most part the notation of Pinardi and Robinson (1986). If we consider an integral over a wavelength $2\pi/k$ in x and the width of the channel L in y, several terms in the energy balance taken together integrate to zero (these are denoted with asterisks in Table V.2). These terms represent redistribution of energy in the field but do not contribute to the growth of the perturbation.

The remaining terms represent either advective or pressure work processes which reveal interactions between the growing perturbation and either the horizontal or vertical shear of the basic state (Table V.2). These terms indicate the relative sizes and characteristic structure of the energy transformations leading to the growth of the perturbation. The spatial patterns of these terms will develop asymmetries. Integration over $2\pi/k$ in x and the channel width L in y provides a box model type summary of energy transformations (e.g. Haidvogel and Holland, 1978).

We will later find it convenient to use the following notation for integration and summation operations:

$$< KP_n > = \int_0^L \int_0^{2\pi/k} KP_n \, dx dy , \tag{12}$$

Table V.2. Perturbation Energy Equation Terms

Symbol	Physical Meaning	Term
$\hat{K}_{nt}$	time rate of change of kinetic energy	$\frac{1}{2} H_n(\nabla\phi_n \cdot \nabla\phi_n)_t$
$\Delta F^t_{\pi n}$*	horizontal pressure work divergence involving acceleration	$H_n \nabla \cdot (\phi_n \nabla \phi_{nt})$
KP_n	conversion from basic state K_n to perturbation $\hat{K}_n$	$-H_n \phi_{nx} \phi_{ny} \Psi_{nyy}$
$\Delta_x F_{\kappa n}$ *	horizontal advection of kinetic energy	$H_n \Psi_{ny} \frac{1}{2} (\nabla\phi_n \cdot \nabla\phi_n)_x$
$\Delta F^a_{\pi n}$ *	horizontal pressure work divergence involving momentum transport	$H_n \nabla \cdot [-\phi_n \Psi_{ny} (\nabla\phi_n)_x + \phi_n \phi_{nx} \Psi_{nyy} \hat{j}]$
$\delta \hat{f}_{\pi n}$	transfer of $\hat{K}_n$ out of layer n into layers $n-1$ and $n+1$	$-f_0 w_{n-1/2} \phi_{n-1/2} + f_0 w_{n+1/2} \phi_{n+1/2}$
$-\hat{b}_n$	conversion from $\hat{A}_{n+1/2}$ and $\hat{A}_{n-1/2}$ to $\hat{K}_n$	$f_0 \frac{H_n}{H_n + H_{n+1}} w_{n+1/2}(\phi_n - \phi_{n+1}) + f_0 \frac{H_n}{H_n + H_{n-1}} w_{n-1/2}(\phi_{n-1} - \phi_n)$
$\hat{A}_{n+1/2t}$	time rate of change of available potential energy	$[\frac{1}{2} \frac{f_0^2}{g'_{n+1/2}} (\phi_n - \phi_{n+1})^2]_t$
$AP_{n+1/2}$	conversion from basic state $A_{n+1/2}$ to perturbation $\hat{A}_{n+1/2}$	$-\frac{f_0^2}{g'_{n+1/2}} (\phi_n - \phi_{n+1})(\Psi_n - \Psi_{n+1})_y \phi_{n+1/2\ x}$
$\Delta_x F_{An+1/2}$ *	horizontal advection of available potential energy	$[\frac{1}{2} \frac{f_0^2}{g'_{n+1/2}} (\phi_n - \phi_{n+1})^2]_x \Psi_{n+1/2\ y}$
$\hat{b}_{n+1/2}$	conversion from $\hat{K}_n$ and $\hat{K}_{n+1}$ to $\hat{A}_{n+1/2}$	$-f_0 w_{n+1/2}(\phi_n - \phi_{n+1})$

*does not contribute to a net energy conversion when integrated over a wavelength $2\pi/k$ and the width of the channel in y.

$$\{KP\} = \sum_{n=1}^{N} < KP_n > , \tag{13a}$$

$$\{AP\} = \sum_{n=1}^{N-1} < AP_{n+1/2} > . \qquad (13b)$$

V.4 Basic stability results

Before presenting the results of the stability analysis, we consider the relevant necessary conditions for instability given our basic state flow. One of the necessary conditions for the instability of an inviscid, zonal flow *U(y, z)* is that the potential vorticity gradient must be positive within some subregion of the (*y, z*) plane and negative in others. We define the quasi-geostrophic potential vorticity of the basic state

$$Q_n = -U_{ny} + \frac{H}{H_n}[F_n(\Psi_n - \Psi_{n+1}) - F_{n-1}(\Psi_{n-1} - \Psi_n)] \qquad (14)$$

The first term on the right-hand side of (14) is the portion of Q_n due to the horizontal shear alone, while the remaining terms of (14) are referred to as the vortex stretching terms. An examination of the potential vorticity and potential vorticity gradient (Q_{ny}) of the basic state (shown for the May 22 jet in Figure V.3) indicates ripe possibilities for both barotropic and baroclinic instability processes. The components of Q_n and Q_{ny} due to horizontal shear alone and those due to vortex stretching alone are also plotted in Figure V.3. Q_{ny} within each layer changes sign at least twice across the jet, raising the possibility of barotropic instability. Q_{ny} also changes sign along most vertical profiles through the jet, indicative of possible baroclinic instability. The complexity of the structure of Q_{ny} for this mixed instability case with *U(y, z)* from observations makes prediction of the details of the stability characteristics difficult, prior to actually carrying out the calculation.

We turn now to our primary stability results using the standard six-layer basic state profiles (Figure V.2). Equation (9) is solved over a range of values for the wavenumber k. We find

Fig. V.3. Potential vorticity Q (left) and potential vorticity gradient Q_y (right) for the May 22 basic state; top panels are for layer 1, second row for layer 2, etc. The bold line is the total Q and Q_y for each layer, the lighter line is the Q and Q_y due solely to the horizontal shear, and the dashed line is the Q and Q_y from the vertical vortex stretching terms.

both the May 22 and June 12 profiles to be unstable to perturbations across a wide spectrum of along-jet wavelengths (Figure V.4). Although the magnitudes of the growth rates (kc_i) differ, the two profiles taken from different locations and at separate times are surprisingly similar in their kc_i versus $2\pi/k$ structure. We note a prominent maximum in kc_i at wavelengths of 260 km for May 22 and 265 km for June 12, with *e*-folding growth periods of 11 days and 7 days respectively. Local maximums in the kc_i versus $2\pi/k$ curve also occur at about 70, 130, and 180 km. The growth rates diminish gradually for scales larger than the maximum at 260-265 km. The calculations were continued out to a maximum wavelength of 800 km (not shown). The maximum growth rate decreases smoothly for the May 22 case from 0.067 d^{-1} at 400 km to 0.023 d^{-1} at 800 km.

Growing perturbations propagate with phase speeds c_r which are almost always positive, i.e., downstream (Figure V.4). The June 12 case exhibits the largest phase speeds (0.34-0.35 m s^{-1}) between 110 and 130 km wavelengths. The May 22 case has a similar region of maximum phase speed (0.12-0.13 m s^{-1}) from 105-150 km. In general the phase speed results seem organized into distinct regions, with steps between them. These same regions can be identified in the kc_i plots with the local maximums mentioned previously. At the wavelengths corresponding to the most unstable modes for June 12 and May 22 (260-265 km), phase speeds are 0.09 and 0.05 m s^{-1} respectively. With increasing wavelength from this point, c_r gradually decreases. The only substantial region where we see negative phase speeds is from 50 to 85 km in the May 22 case. The June 12 case, however, exhibits moderate positive values (0.22 m s^{-1}) within this same range of wavelengths. Note that all of the phase speed results, both positive and negative, lie within the velocity range of the basic state (Figure V.2), as expected. For the reasons stated in section 3, we concentrate on the May 22 profile and present additional results for this case. The June 12 results are similar.

The wavelength $2\pi/k$ for which kc_i is a maximum yields the along-jet scale of the most unstable mode. In this normal mode approximation, the implication is that this mode will probably be the first one to emerge from a background mixture of small-amplitude disturbances. It is plausible, however, that prominent modes other than the most unstable one will be seen as well (see part 2). For this reason we seek to better understand the nature of the instability not only for the growth rate maximum at 260 km but also for large local maxima at 135 and 185 km for the May 22 case. Figure V.5 presents kc_i results for the six most unstable modes at each $2\pi/k$ value rather than only the most unstable mode. It is apparent that the shape of the kc_i curve in Figure V.4 is a result of the superposition of several different growth rate curves which are present throughout a wide range of wavenumbers but take turns in being the most unstable mode. The suspicion that these modes of instability are qualitatively different from one another will be confirmed shortly upon examination of the eigenvector structure.

The solution to the linear stability problem provides no information regarding the actual magnitude of the perturbation velocities. Nevertheless, it is helpful to impose an arbitrary size for a perturbation velocity in order to illustrate the structure of the instability and in anticipation of the move to finite amplitude. For this reason we arbitrarily set a size for the perturbation, choosing the maximum velocity of u_1 in the surface layer perturbation to be 1/3 of the corresponding basic state velocity U_1 at the same y value. The same scaling is used throughout; the relative structure of the perturbation in different parts of the flow is unchanged. This arbitrary scaling of the perturbation will remain constant for all results presented in this study.

The maps of perturbation stream function $\phi_n(x, y)$ (Figure V.6*a*) show a characteristic shape where the center of the disturbance is displaced upstream relative to the flanks (termed the "banana" shape by Holland and Haidvogel [1980]). This slant of the perturbation streamlines into the horizontal shear of the basic state (Figure V.2), giving the impression that it is

Fig. V.4. Phase speeds c_r (top) and growth rates kc_i (bottom) versus along-jet wavelength $2\pi/k$ of the perturbation for the May 22 (bold line) and June 12 (lighter line) cases.

Fig. V.5. Growth rates versus along-jet wavelength for the six fastest growing modes at each $2\pi/k$ value, May 22 case.

attempting to decelerate it, is indicative of a barotropic instability process [Pedlosky (1987), section 7.3]. Figure V.6*b* shows $\gamma\phi_n(x, y)$ added back into the basic state $\Psi_n(y)$. This presentation is somewhat artificial, since the maps will change depending on how we choose the strength of the perturbation. It is useful, however, to gain some understanding of what form the complete flow field might take and to easily see where the peaks and troughs of the meander occur.

The perturbation vertical velocities $w_{n+1/2}$ (Figure V.7*a*) are most intense at the core of the jet, with the largest magnitudes found about halfway between the locations of the crests and troughs in the flow field of Figure V.6*b*. The vertical velocities exhibit a characteristic structure that involves positive(negative) $w_{n+1/2}$ for fluid motion from(to) troughs and to(from) crests. This structure of the $w_{n+1/2}$ field is consistent with the form of the perturbation vorticity field $\nabla^2\phi_n$ (Figure V.7*b*). The vortex stretching term in equation (2) implies the development of positive vorticity in the troughs of the perturbation and negative vorticity in the crests, as seen in the center of the jet in the perturbation vorticity field. The oppositely signed vorticity at the flanks of the jet reflects perturbations in vorticity associated with growth in amplitude of the unstable wave.

We also extract vertical sections from our results and plot contours of modal structure (Figure V.8) in the (*y, z*) plane, as Beckmann (1988) and others do. This presentation helps clarify the vertical structure of the different modes corresponding to the local maxima in kc_i seen at along-jet wavelengths of about 140, 180, and 260 km. We show both the fastest and the second-fastest growing modes at these three wavelengths. Referring to Figure V.5, note that the second mode at 180 km appears to be part of the same branch that becomes the first mode at 260 km, and vice-versa. Examination of the structure of the modes at many different wavelengths verifies this crossover. The effect can be seen in Figure V.8; mode 1 at 180 km is similar to mode 2 at 260 km, while mode 2 at 180 km is similar to mode 1 at 260 km. The

Fig. V.6. Maps of (*a*) perturbation stream function and (*b*) basic state + perturbation stream function, for the May 22 case (260 km along-jet wavelength). Solid/bold/dashed lines indicate positive/zero/negative contours.

former pair shows a surface-intensified amplitude field while the phase has more depth independence and a maximum value at depth. The latter pair exhibits more depth independence in amplitude. Mode 2 at 140 km and mode 1 at 180 km are also similar. The structure of the phase of mode 1 at 260 km has the largest vertical change of those presented; the perturbation leads from the bottom (also apparent in Figure V.7*a*), indicating baroclinic conversion of energy from the basic state to the perturbation.

V.5 Energetics

Examination of the variation of kc_i with along-jet wavelength and the modal structure of the perturbation does not by itself reveal the balance of energy sources for the mixed instability, although we have noted indications of both barotropic and baroclinic instability processes. We now investigate the relative sizes and structure of these energy transformations. From the development in section 3, we are able to calculate maps of the relevant terms in the kinetic and potential energy balances. The characteristic patterns seen in the maps of the energetics can be usefully compared to similar maps from the nonlinear finite amplitude studies of part 2.

We focus initially on the May 22 case for the wavelength of maximum kc_i (260 km). Figure V.9 displays maps of all the terms from the kinetic and potential energy equations which represent net transformations of perturbation energy from one form to another, rather than simply a redistribution of energy within the same field (refer to Table V.2). The time rate of change of both perturbation kinetic energy and available potential energy is positive (columns 1 and 2 of Figure V.9). The complexity of the structure of $\hat{K}_{nt}$ and $\hat{A}_{n+1/2t}$ is due to the combination of different energy transformation processes taking place, displayed in the remaining five columns of Figure V.9.

Fig. V.7. Maps of (*a*) perturbation vertical velocity *w* and (*b*) perturbation vorticity, for the fastest growing mode from the May 22 case (260 km along-jet wavelength). Solid/bold/dashed lines indicate positive/zero/negative contours.

The term KP_n is the Reynolds stress source term for barotropic instability, representing the cross-jet component of the divergence in the advection of kinetic energy. It contains the perturbation momentum flux $u_n v_n$ which interacts with the horizontal shear of the basic state, yielding a measure of the transformation of basic state kinetic energy (K_n) to perturbation kinetic energy ($\hat{K}_n$). KP_n develops into cross-jet pairs, periodic with x-wavelength half of $2\pi/k$, concentrated where $|U_{ny}|$ is greatest (column 3 of Figure V.9). The asymmetries in values of highs and lows, with the high values dominating, indicates a net transformation of K_n to $\hat{K}_n$. A small asymmetry is also apparent in the cross-jet sense; the more intense patterns along the bottom flank of the jet correspond with the asymmetry of the basic state, which has larger horizontal shear on this side. Layers 1 and 4 exhibit the most intense KP_n activity.

The $AP_{n+1/2}$ is the analogous source term for baroclinic instability, indicating the transformation of basic state available potential energy ($A_{n+1/2}$) to perturbation available potential energy ($\hat{A}_{n+1/2}$). $AP_{n+1/2}$ represents the rate of work accomplished by the Reynolds heat flux $(\phi_n - \phi_{n+1})\phi_{n+1/2\,x}$ against the cross-jet gradient of basic state density. $AP_{n+1/2}$ (column 4 of Figure V.9) is centered along the jet axis where the basic state vertical shear is greatest. The asymmetries which develop imply a net conversion of $A_{n+1/2}$ to $\hat{A}_{n+1/2}$. The asymmetries and thus conversions at interfaces 1.5 and 4.5 are particularly strong.

Columns 5 and 6 of Figure V.9 present two views of the buoyancy work energy flux. This is the conversion process internal to the perturbation which allows its kinetic energy to increase at the expense of its available potential energy, or vice-versa. The $\hat{b}_{n+1/2}$ fields at interfaces 4.5 and 5.5 indicate the largest amounts of $\hat{A}_{n+1/2}$ being lost to $\hat{K}_n$. The maps of $-\hat{b}_n$ in turn indicate that layers 4, 5, and 6 are the beneficiaries of the largest amounts of $\hat{K}_n$ from this conversion process. The patterns of buoyancy work seem to exhibit a less symmetrical cross-jet structure among the lower layers as opposed to the upper ones.

Fig. V.8. Vertical sections of perturbation stream function amplitude and phase at three selected along-jet wavelengths, showing the modal structure of the two fastest growing modes, all for the May 22 case. Contour interval for amplitude plots is arbitrary but does not change. Contour interval for phase plots is 15° (solid/bold/dashed lines indicate positive/zero/negative contours).

Fig. V.9. Maps of the energy transformation terms (see text and Table V.2 for definitions) for the 260-km along-jet wavelength May 22 case (solid/bold/dashed lines indicate positive/zero/negative contours).

The rightmost column of Figure V.9 maps the vertical pressure work term $\delta \hat{f}_{\pi n}$. This represents the conversion of $\hat{K}_n$ from one layer to another. The patterns of $\delta \hat{f}_{\pi n}$ are periodic at half of $2\pi/k$ rather than a full wavelength. Layer 1 exhibits the most intense highs and lows, although it is not clear that much net transfer in or out of layer 1 occurs.

By integrating each of these terms across the channel and over a perturbation wavelength $2\pi/k$, we obtain a sense of the overall importance of different energy transformations. The absolute values of the resulting numbers will have no meaning but their relative sizes provide a convenient summary of the relative importance of the different energy transformations. Figures V.10*a*-10*c* follow in the tradition dating back to Phillips (1956) in presenting a box model view of the integrated energy fluxes $< KP_n >$, $< AP_{n+1/2} >$, $< \hat{b}_{n+1/2} >$, and $< \delta \hat{f}_{\pi n} >$. The values are arbitrarily normalized such that the conversion $KP_1 = 1.00$. The thickness of an arrow is proportional to the indicated energy transfer. Capital letters inside rectangles are used to represent the basic state, while lowercase letters within ovals symbolize the perturbation.

The energy summary for the maximum growth rate (Figure V.10*c*), confirms at a glance what we have already guessed at; both barotropic and baroclinic energy transformations are important to the growth of the perturbation. Figure V.10*c* provides a synopsis of the same information contained in Figure V.9. Both the $< KP_n >$ and the $< AP_{n+1/2} >$ terms are feeding the perturbation at all levels. The dominant transfers are from the mean to perturbation kinetic energy in layers 1 and 4 and the mean to perturbation potential energy at interfaces 4.5 and 5.5; the other energy fluxes are insignificant.

From the kc_i versus wavelength characteristics (Figures V.4 and V.5), the phase speed behavior (Figure V.4), as well as the modal structure (Figure V.8), it appears as if the local growth rate maximums observed at about 130 and 180 km are associated with perturbations that are distinct features, different in nature from those at 260 km. We present the global energetics

Fig. V.10. Graphical presentation of the integrated energy fluxes at (a) 130 km, (b) 180 km, and (c) 260 km along-jet wavelength ($2\pi/k$) for May 22 case. The thickness of the shaft of an arrow is proportional to the relative size of the indicated energy transfer, which is also given a numerical value. The energy fluxes are normalized such that the transformation of basic state kinetic energy to perturbation kinetic energy in layer 1 is 1.00. Capital labels inside rectangles symbolize the basic state; lowercase labels inside ovals symbolize the perturbation.

at 130 and 180 km in Figures V.10*a* and V.10*b*, and the qualitative differences between these features are again clear.

At 130 km (Figure V.10*a*), the barotropic instability processes are dominant, especially within layers 1 and 4. Interestingly, the potential energy of the perturbation is actually flowing in the "wrong" sense, back into the mean. Haidvogel and Holland (1978) also present such a case in one of their linear stability analyses. They suggest that as the perturbation grows to finite amplitude, the sign of this transfer will change back to the "right" direction [also discussed by Veronis (1981)]. Finite amplitude results involving this behavior are found in part 2. The other notable feature of the global energetics at 130 km is the tendency for kinetic energy in the perturbation to be transferred down into the lower layers through the $< \delta \hat{f}_{\pi n} >$ terms, especially within layers 1-4. Much of the energy coming from the KP_1 process is actually flowing down the water column and supplying lower layers.

At 180 km (Figure V.10*b*), barotropic instability processes are still dominant within layers 1 and 4. The conversion in layer 4 is now the largest, rather than that in layer 1. The baroclinic processes are nearly neutral, contributing little in either sense. The vertical transfer of kinetic energy downward via $< \delta \hat{f}_{\pi n} >$ is even stronger in this case than at 130 km.

As a measure of the overall volume-integrated importance of baroclinic versus barotropic instability processes for the perturbation we consider the ratio $\{AP\}/\{KP\}$, using the notation of (13). Figure V.11 shows the ratio $\{AP\}/\{KP\}$ over the range of along-jet wavelengths. For wavelengths less than ≈90 km, the instabilities are almost entirely barotropic in nature. From ≈110-190 km, barotropic instability processes still dominate; the negative values of $\{AP\}/\{KP\}$ are due to $\{AP\} < 0$ and $\{KP\} > 0$. The flow of potential energy is from perturbation to mean, but the barotropic conversion process is large enough to maintain the instability. Both the 130 and 180-km cases discussed previously fall into this category.

Fig. V.11. The ratio of the relative importance of baroclinic/barotropic instability processes ($\{AP\}/\{KP\}$) for the standard May 22 case, as a function of along-jet wavelength. Negative values of $\{AP\}/\{KP\}$ are due to $\{AP\} < 0$ (energy flow from perturbation to mean) and $\{KP\} > 0$.

With wavelength increasing from ≈200 km, both baroclinic and barotropic instability processes contribute significantly to the growth of the perturbation. A gradual tendency toward a more baroclinic instability occurs with increasing wavelength. The most unstable mode (at 260 km) is characterized by $\{AP\}/\{KP\} = 0.90$. Thus baroclinic and barotropic instability processes are of nearly equal importance for the fastest growing mode.

V.6. Variations

V.6.1 Increased vertical resolution

One of the points made by Beckmann (1988) as well as others is the importance of using sufficient layers in the vertical to avoid the well-known short-wavelength cutoff often noted in idealized studies. This effect is seen, for example, among the two-layer idealized jet linear stability results of Holland and Haidvogel (1980); their growth rates go rapidly to zero with decreasing wavelength from about 200 km. Walstad *et al.* (1991) investigate the use of a 12-layer model and conclude that the six-layer model is sufficient for this region. We test the use of the same 12-layer model, which is equivalent to our six-layer May 22 basic case (Figure V.2*b*) except for the increased vertical resolution. The 12-layer basic state is described in Table V.3 and Figure V.12*b*. In addition, we create a nine-layer equivalent case by combining the bottom six layers of the 12-layer model into three layers. The nine-layer basic state is described by Table V.4 and Figure V.12*a*.

Table V.3. Nine-Layer Basic State Characteristics

Layer	Thickness, m	$g\Delta\rho/\rho_0$, m s^{-2}
1 (surface)	48	
		6.0443×10^{-3}
2	60	
		7.0874×10^{-3}
3	84	
		3.2294×10^{-3}
4	102	
		2.0391×10^{-3}
5	138	
		2.0421×10^{-3}
6	176	
		3.0625×10^{-3}
7	528	
		3.2539×10^{-3}
8	896	
		2.5541×10^{-3}
9 (bottom)	1138	

Table V.4. Twelve-Layer Basic State Characteristics

Layer	Thickness, m	$g\Delta\rho/\rho_0$, m s^{-2}
1 (surface)	48	
		6.0443×10^{-3}
2	60	
		7.0874×10^{-3}
3	84	
		3.2294×10^{-3}
4	102	
		2.0391×10^{-3}
5	138	
		2.0422×10^{-3}
6	176	
		2.0965×10^{-3}
7	232	
		1.7234×10^{-3}
8	296	
		1.6041×10^{-3}
9	392	
		1.5863×10^{-3}
10	504	
		1.3437×10^{-3}
11	572	
		1.0390×10^{-3}
12 (bottom)	566	

Table V.5. Pure Baroclinic Model

Layer	Basic State Velocities, m s^{-1}
1 (surface)	0.24
2	0.17
3	0.14
4	0.10
5	0.04
6 (bottom)	-0.01

Layer thicknesses and g' values are listed in Table V.1.

The growth rates and phase speeds for the equivalent six, nine, and 12 layer models are quite similar (Figure V.13). The kc_i maximum for the 12-layer case now occurs at 250 km rather than 260 km for the six-layer case. The nine-layer case splits the difference between them fairly neatly. From roughly 170 to 250 km, notice that with decreasing numbers of layers, the kc_i curve shifts slightly to the right. This is the extent of the short-wavelength cutoff phenomenon in this case, and the differences are minor. In the 12-layer case, the local maximum in growth rate at ≈180 km is no longer present, but the magnitude of the growth rate here is comparable to the six-layer case. The differences among the curves for $2\pi/k$ < 170 km are not too substantial but more difficult to interpret. In the 130-km region, the 12-layer local maximum in kc_i is about 30% smaller than the six-layer case. The three curves converge again with decreasing wavelength from this point. For simplicity and for consistency with Walstad *et al.* (1991) and part 2, we use the six-layer model for our primary results and interpretation.

V.6.2 One-dimensional cases

As another approach to the question of the importance of barotropic versus baroclinic processes in this region, we thought it would be instructive to investigate the corresponding one-dimensional cases. We create a pure baroclinic model, with strictly vertical shear, by averaging the May 22 horizontal jet profile over y while retaining the same layer structure in the vertical (resulting velocity profile listed in Table V.5). Similarly, we create a pure barotropic case, with only horizontal shear, by averaging (weighted by layer thickness) all six layers vertically into a single layer model (Figure V.14). The asymmetry of the basic state (which has always been present) is particularly evident in Figure V.14. The stability analysis is accomplished using almost exactly the same methods as previously outlined, with straightforward simplifications of the formulas.

Fig. V.12. Basic state profiles for the (*a*) nine-layer case and (*b*) 12-layer case, both from May 22.

Fig. V.13. Phase speeds and growth rates for the 12-layer case (bold line), nine-layer case (normal line), and standard six-layer case (dashed line), all from May 22.

The results (Figure V.15) are satisfying in that they offer additional clues as to the structure of the mixed stability case. The pure barotropic case exhibits a kc_i maximum at 110 km, while the pure baroclinic has maximum kc_i at 285 km. Results for c_r are similar for all cases except for a 105-195 km region where the mixed case perturbation propagates roughly twice as fast as the others. For wavelengths smaller than ≈170 km, the pure barotropic and the fully mixed cases are similar, although the mixed case is usually more unstable. For wavelengths larger than ≈170 km, the pure baroclinic results are close to the mixed ones, although less unstable for shorter wavelengths and more unstable for longer ones. The mixed case is substantially more unstable than the pure barotropic one at larger wavelengths. These results are consistent with some findings of Song (1971), who performs similar comparisons for a variety of idealized situations. From the point of view of a barotropic jet, the addition of vertical shear tends to destabilize at all wavelengths. If horizontal shear is added to a pure baroclinic problem, on the other hand, it has a destabilizing effect for shorter wavelengths but a stabilizing effect at longer ones. Note, in general, that the multiple peaks in growth rate seen in the mixed stability case are not present in the one-dimensional cases; the complexity of the mixed case is evidently related to the combination of different instability mechanisms occurring simultaneously.

The one-dimensional results are consistent with our analysis of the energetics of the mixed case (section 5). We found that the instability at 260 km was characterized by nearly equal contributions from barotropic and baroclinic processes. Figure V.15 indicates that purely barotropic and baroclinic instability mechanisms produce roughly comparable growth rates. The dominance of barotropic energy transformations around the secondary maximum at 180 km (Figure V.11) also agrees with these results, since at this wavelength the pure baroclinic case has very small kc_i. The pure baroclinic case illustrates well the cutoff at short wavelengths mentioned above. In Figure V.15, the increasing relative importance of baroclinic processes as we move to

Fig. V.14. Basic state profile for the May 22 pure barotropic, single-layer case.

Fig. V.15. Phase speeds and growth rates for the pure baroclinic instability case (bold line), the pure barotropic instability case (normal line), and the standard six-layer mixed instability case (dashed line), all from May 22.

longer wavelengths is also consistent with the energy analysis of the mixed case; at 260 km the *{AP}/{KP}* ratio from the global energetics is 0.90, while at 400 km this ratio has increased to 1.18 (Figure V.11).

V.6.3 Non-zonal cases and the beta effect

The linear stability model was developed on an *f* plane, for simplicity and also for consistency with part 2 of the study. We calculate for layer 1 the dimensionless parameter $\beta^* = \beta L^2 U_0^{-1} \approx 0.029$ ($\beta = 1.8 \times 10^{-11}$ m^{-1} s^{-1}, $U_0 = 0.53$ m s^{-1}, $L = 29$ km), which is small, so the beta effect is probably minor. For this type of analysis, however, the extension to the beta plane and to arbitrary basic state orientation (for the two-dimensional parallel mean flow which we consider here) turns out to be straightforward numerically (Robinson and McWilliams, 1974). While maintaining the coordinate system aligned with the mean state orientation, we now define both a $\beta^{(x)} = f_x$ and a $\beta^{(y)} = f_y$. Adding these terms to our development, (8) now takes the form (dimensional)

$$(U_n - c)\{\hat{\phi}_{nyy} - k^2\hat{\phi}_n + \frac{H}{H_n}[F_n(\hat{\phi}_{n+1} - \hat{\phi}_n) - F_{n-1}(\hat{\phi}_n - \hat{\phi}_{n-1})]\}$$

$$-\hat{\phi}_n\{U_{nyy} - \beta^{(y)} + \frac{H}{H_n}[F_n(U_{n+1} - U_n) - F_{n-1}(U_n - U_{n-1})]\}$$

$$+\frac{i}{k}\hat{\phi}_{ny}\beta^{(x)} = 0 \quad , \tag{15}$$

and may be solved as before. The resulting differences in growth rates and phase speeds for our standard May 22 case are shown for three choices of basic state orientation (Figure V.16): eastward ($\beta^{(x)} = 0$, $\beta^{(y)} = \beta$), equatorward ($\beta^{(x)} = \beta$, $\beta^{(y)} = 0$), and westward ($\beta^{(x)} = 0$, $\beta^{(y)} = -\beta$), where $\beta = 1.8 \times 10^{-11}$ m^{-1} s^{-1}. For an equatorward flow, which is the general orientation of the CTZ jet, the most unstable mode has an inverse growth rate of 11.4 days rather than the 11.0 days in the case without the beta effect. The beta effect is slightly stabilizing in all cases except

for a westward tending mean flow, where it is slightly destabilizing. If we choose a mean flow aimed directly to the west, the inverse growth rate of the most unstable wave is 10.0 days rather than the 11.0 days of the case without the beta effect. The results for all of the cases in Figure V.16 are qualitatively similar. We conclude that the beta effect has a relatively minor influence on the linear stability of the jet profiles.

V.7 Summary

We take advantage of the combined hydrographic and ADCP data from the 1987 CTZ experiment to perform a quasi-geostrophic linear stability analysis of a CTZ jet using observed profiles. The basic state flow fields are somewhat idealized, but they retain much of the complexity of the real ocean and yield richly structured results. We primarily apply well-tested linear stability analysis techniques to the coastal transition zone region. Additional motivation for the linear analysis is to provide necessary information for the finite amplitude nonlinear study in part 2.

We treat the fully mixed linear stability problem (with both horizontal and vertical shear), with relatively fine resolution in both y and z, using basic state profiles from objectively analyzed data. We examine the behavior of the growth rates, phase speeds, and eigenvector structure as a function of along-jet wavelength. We also analyze the energetics to determine the degree to which baroclinic and barotropic instability processes are important and the structure of the energy transfers. The application of similar techniques to the extensive 1988 CTZ data set is currently being explored.

One of our major results is the identification of the fastest growing instability with an along-jet wavelength of ≈260 km. The characteristic inverse growth rate of this meander is 7-11

Fig. V.16. Phase speeds and growth rates for the May 22 case with the beta effect for a westward flowing jet (bold line), eastward flowing jet (big dashes), and southward flowing jet (normal line), compared to the standard f plane case (small dashes).

Fig. V.17. $\Delta D_{0/500}/g$ (m), the dynamic height of the sea surface relative to 500 dbars, normalized by g, over the complete survey grid for the 1987 summer cruise (Kosro *et al.*, 1991). The dashed line is drawn to help make a rough estimate of a meander wavelength, which is ≈250 km.

days, and the propagation speed of the perturbation is 0.05-0.09 m s^{-1} downstream, using the differences between our May 22 and June 12 results as a measure of uncertainty. The comparison of these results to actual meanders seen in either modeling or observations will always be problematic; the linearized theory is only valid for infinitesimally small-amplitude perturbations. It is remarkable how fruitful the linear theory has been, however, and even mature fluctuations will often be approximately explained well past the formal limits of the theory [Pedlosky (1987) section 7.3].

With the preceding caveat, then, consider the flow field of Figure V.17 from Kosro *et al.* (1991). This is the complete June survey dynamic height field. We only considered the southern half of the array previously (Figure V.1), following Walstad *et al.* (1991). A look now at the full survey reveals a large meander extending from about 38°40′N to 41°N. Although irregular in shape, the length of this feature is still fairly well defined. If we consider the $\Delta D = 0.9$ contour and draw a straight line such that the line is bisected by the contour, we obtain a rough estimate of 250 ± 20 km for the wavelength. The persistent maximum seen at a wavelength of ≈260 km throughout our linear stability results is consistent with the size of this observed meander.

The phase speed results of the model imply a 4-8 km/d propagation of a perturbation downstream. This propagation of the jet meander is difficult to identify even qualitatively from the observations, given the available data and the complexity of the flow field. In the northern region of the 1987 CTZ experiment, off of Cape Mendocino, phase propagation is not clearly evident (see e.g., Kosro *et al.* [1991]). In the southern region of the Walstad *et al.* (1991) grid (south of about 38° N, our Figure V.1), the jet features do appear to translate roughly 50 km downstream from May 22 to June 12. The linear stability results predict a larger shift of 80-160 km over this same time period. The results from part 2, however, indicate that the propagation

velocities of finite amplitude meanders are, in fact, generally smaller than the linear stability values.

Finally, our analysis of the energetics of the meander growth verifies that the instability is a mixed one, with conversions from both the basic state kinetic energy and basic state potential energy. We go on to provide detailed energy balance information. The primary result is that unstable solutions over a range of wavelengths from 200 to 400 km are all characterized by substantial contributions from both barotropic and baroclinic instability processes, and these two sources of energy are of nearly equal importance for the fastest growing fluctuation.

V.8 Acknowledgments

S.D.P. was supported by Office of Naval Research (ONR) Coastal Sciences grant N00014-90-J-1211, ONR Mesoscale Physical Oceanography grant N00014-90-J-1177, and National Science Foundation grant OCE-8709930. J.S.A. and L.J.W. were supported by ONR Coastal Sciences grants N00014-90-J-1051 and N00014-87-K-0009. Thanks to Priscilla Newberger for assistance with the basic state profiles and to P. M. Kosro and A. Huyer for the high quality of the data. S.D.P. thanks Robert L. Smith for support and encouragement during this study.

(Received January 14, 1991; accepted March 21, 1991.)

V.8 References

Allen, J. S., L. J. Walstad, and P. A. Newberger, 1991: Dynamics of the coastal transition zone jet, 2. nonlinear finite amplitude behavior. *J. Geophys. Res.*, **96**, 14995-15016.

Beckmann, A., 1988: Vertical structure of midlatitude mesoscale instabilities. *J. Phys. Oceanogr.*, **18**, 1354-1371.

CTZ Group, 1988: The Coastal Transition Zone Program. *EOS, Trans. Am. Geophys. Union*, **69**, 698-699, 704, 707.

Haidvogel, D. B. and W. R. Holland, 1978: The stability of ocean currents in eddy-resolving general circulation models. *J. Phys. Oceanogr.*, **8**, 393-413.

Hart, J. E., 1974: On the Mixed Stability Problem for Quasi-geostrophic Ocean Currents. *J. Phys. Oceanogr.*, **4**, 349-356.

Holland, W. R. and D. B. Haidvogel, 1980: A parameter study of the mixed instability of idealized ocean currents. *Dyn. Atmos. Oceans*, **4**, 185-215.

Huyer, A., P. M. Kosro, J. Fleischbein, S. R. Ramp, T. Stanton, L. Washburn, F. P. Chavez, T. J. Cowles, S. D. Pierce, and R. L. Smith, 1991: Currents and water masses of the coastal transition zone off northern California, June to August 1988. *J. Geophys. Res.*, **96**, 14809-14831.

Johns, W. E., 1988: One-dimensional baroclinically unstable waves on the Gulf Stream potential vorticity gradient near Cape Hatteras. *Dyn. Atmos. Oceans*, **11**, 323-350.

Kaufman, L. C., 1975: The LZ algorithm to solve the generalized eigenvalue problem for complex matrices. *ACM Trans. Math. Software*, **1**, 271-281.

Killworth, P. D., 1980: On determination of absolute velocities and density gradients in the ocean from a single hydrographic section. *Deep-Sea Res.*, **27**, 901-929.

Kosro, P. M., A. Huyer, S. R. Ramp, R. L. Smith, F. P. Chavez, T. J. Cowles, M. R. Abbott, P. T. Strub, R. T. Barber, P. Jessen, and L. F. Small, 1991: The structure of the transition zone between coastal waters and the open ocean off northern California, winter and spring 1987. *J. Geophys. Res.*, **96**, 14707-14730.

Pedlosky, J., 1987: *Geophysical fluid dynamics*, p. 710 pp., Springer-Verlag, New York.

Phillips, N. A., 1956: The general circulation of the atmosphere: a numerical experiment. *Q. J. R. Meteorol. Soc.*, **82**, 123-164.

Pinardi, N. and A. R. Robinson, 1986: Quasigeostrophic energetics of open ocean regions. *Dyn. Atmos. Oceans*, **10**, 185-219.

Robinson, A. R. and J. C. McWilliams, 1974: The baroclinic instability of the open ocean. *J. Phys. Oceanogr.*, **4**, 281-294.

Song, R. T., 1971: A numerical study of the three-dimensional structure and energetics of unstable disturbances in zonal currents: part II. *J. Atmos. Sci.*, **28**, 565-586.

Strub, P. Ted, P. Michael Kosro, and Adriana Huyer, 1991: The nature of the cold filaments in the California current system. *J. Geophys. Res.*, **96**, 14743-14768.

Veronis, G., 1981: Dynamics of the large-scale ocean circulation, in *Evolution of physical oceanography*, ed. B. A. Warren and C. Wunsch, 140-183, M.I.T. Press, Cambridge MA.

Walstad, L. J., J. S. Allen, P. M. Kosro, and A. Huyer, 1991: Dynamics of the coastal transition zone jet through data assimilation studies. *J. Geophys. Res.*, **96**, 14959-14977.

VI. Continuity of the Poleward Undercurrent Along the Eastern Boundary of the Mid-Latitude North Pacific

Stephen D. Pierce, Robert L. Smith, P. Michael Kosro, John A. Barth
College of Oceanic and Atmospheric Sciences
104 Ocean Admin Bldg, Oregon State University, Corvallis, OR, 97331-5503

Chris D. Wilson
NOAA-NMFS, Seattle, WA

Submitted 1/21/98 for publication to: *Deep-Sea Research*, California Current Special Issue

VI.1 Abstract

Several recent data sets improve our view of the poleward undercurrent of the California Current system. As part of a triennial National Marine Fisheries Service (NMFS) survey of Pacific whiting, a series of shipboard acoustic Doppler current profiler (ADCP) velocity sections across the shelf break from 33−51°N at about 18 km meridional spacing were collected July-August 1995. Significant (> 0.05 ms^{-1}) subsurface poleward flow occurred in 91% of the sections, with a mean poleward undercurrent core velocity of 0.17±0.01 ms^{-1}. A mean cross-shelf section using the entire data set has statistical significance, revealing an undercurrent core >0.1 ms^{-1} from 175−320 m depth 20−25 km off the shelf break. The mean poleward volume transport in a 140−325 m layer is $0.9\pm0.2 \times 10^6 m^3 s^{-1}$. We focus particular attention on the Cape Blanco to Cape Mendocino region, and we compare with shipboard ADCP results three weeks later from a study of coastal upwelling processes near Cape Blanco. ADCP streamfunction maps are derived and strongly suggest one portion of flow is continuous over the 440 km meridional extent of the analysis region. Other portions of the flow show evidence of offshore turning, separation, and the formation of anti-cyclonic eddies. We also note that isopycnic potential vorticity from alongslope CTD stations during the NMFS survey is a good tracer for the poleward flow, providing additional indirect evidence of the undercurrent's meridional continuity.

VI.2 Introduction

Subsurface poleward flow occurs along all five major oceanic eastern boundaries. At mid-latitudes, this poleward flow opposes the equatorward subtropical eastern boundary current flow at the surface. During the coastal upwelling season, the poleward flow also opposes intense equatorward surface-intensified upwelling jets. These undercurrents are usually found over the continental slope and have typical alongshore speeds of 0.1−0.3 ms^{-1} and depth range 100−300 m (Neshyba *et al.*, 1989; Warren, 1990). Since they have volume transports of O(1) $\times 10^6 m^3 s^{-1}$, they may be significant oceanic features in a global circulation context, besides being important aspects of eastern boundary regions.

Although the poleward undercurrent in the California Current system has been the best-observed and most studied of any, several basic dynamic and kinematic issues remain unresolved (eg. Warren, 1990). Some of the outstanding kinematic questions concern the undercurrent's continuity in both space and time. Most historical observations have consisted of individual cross-shore hydrographic sections and relatively short current meter records. Some of the most interesting recent observations of the poleward undercurrent have been Lagrangian measurements using subsurface RAFOS drifters (Collins *et al.*, 1996b). These measurements unambiguously demonstrate the continuity of the poleward flow at about 140 m depth over a 500 km path from 37.8−41.8°N.

The 1995 triennial survey by the National Marine Fisheries Service (NMFS), to assess the abundance and distribution of Pacific whiting, included shipboard acoustic Doppler current profiler (ADCP) velocities which we examine here. The survey sampled the entire mid-latitude eastern Pacific slope in July-August 1995, with cross-slope transects running nominally from 50 m to 1500 m isobaths at 18 km meridional spacing (Figure VI.1). Although the cruise plan was largely determined from fisheries considerations, the data set is also well-suited to studying the

poleward undercurrent.

Significant quantities of Pacific whiting were detected from 38°N to 51°N. Relatively dense aggregations of fish were located near Pt. Arena, Cape Mendocino, central Oregon, and off southern and northern Vancouver Island. As in previous surveys, the size composition of Pacific whiting generally increased with latitude. The mean daytime fish depth was 195 m, and fish were found within poleward flow about 80% of the time (Wilson and Guttormsen, 1997). We do not discuss the biological results here.

The meridional extent of the NMFS ADCP data allows us to address issues of spatial continuity and latitudinal variation. Also in August 1995, three weeks after the NMFS survey passed Oregon, an intensive SeaSoar/ADCP survey studied upwelling processes at Cape Blanco (Barth *et al.*, 1998; Barth and Smith, 1998). We present some results from this survey, which observed strong interaction between the poleward undercurrent and a separating coastal upwelling jet above.

In the presence of tidal currents and inertial oscillations, and with little concurrent cross-shore hydrographic data, we seek to detect the subtidal and relatively stable and geostrophic poleward undercurrent. We accomplish this primarily using two methods: averaging together many cross-shore sections to reduce the "noise", and deriving streamfunction and thus revealing the divergenceless geostrophic velocity field.

VI.3 Data and methods

Surveys to assess the abundance and distribution of Pacific whiting have been conducted every 3 years since 1977 by the NMFS. The survey in 1995 was by the *R/V Miller Freeman* and included acoustic echo measurements at two frequencies (38 and 120 kHz) using a Simrad

EK500 system, as well as trawl work. The complete 1 July − 1 September 1995 survey included a fast run down to the southern end from Seattle at the beginning and additional transects from 52−55°N off the Queen Charlotte Islands at the end. Results here use data from 7 July − 28 August between 33−51°N (Figure VI.1). Nominal meridional spacing of these 105 mostly east-west lines was 18 km, and the mean length of a transect was 52 km. Transects generally ran mid-shelf to mid-slope, between the 50 m and 1500 m isobaths, sometimes extending to deeper water depending on real-time biological scattering results. CTD casts were made at selected trawl sites and at two or three locations along every second or third transect, down to depths of about 500 m. For the first time, this Pacific whiting survey also included acoustic Doppler current profiler (ADCP) velocity measurements.

The CTD data are used to compute "spiciness" as defined by Flament (1986). Spiciness is approximately perpendicular to σ_θ in a T-S diagram and works well in the California Current system because average T-S curves lie roughly orthogonal to isopycnals (Tibby, 1941). High spiciness corresponds to high temperature or high salinity while low spiciness corresponds to low temperature or low salinity. Temperature and salinity, hence spiciness, on subsurface isopycnals can be assumed to be conservative.

An RD Instruments 153.6-kHz narrow-band, hull-mounted ADCP measured currents throughout the survey. We used a vertical bin width of 8 m, pulse length of 8 m, and an ensemble averaging time of 2.5 min. Pings per ensemble varied from 66−101, and the depth range of good data (good pings >30%) was typically 22−326 m. Details of ADCP data processing generally follow the methods used for the *R/V Wecoma* Cape Blanco study (Barth *et al.*, 1998), which are contained in the data report Pierce *et al.* (1997a); we summarize here. Data were required to pass tests of sufficient return signal, acceptable second derivatives of u, v, and w with respect to depth, and reasonable error velocities, as recommended by Firing *et al.* (1995) and Zedel and

Church (1987). The ADCP was slaved to the EK500 biological instrument to avoid interference. Pre-cruise tests revealed no interference between the two instruments when the ADCP obtained ship velocity from navigation alone. The ADCP bottom-tracking feature, however, which puts more energy into the water, was found to cause an artificial signal on the EK500. For this reason, bottom-tracking was never enabled throughout the survey. GPS P-code (military-type) navigation was used for position and gyrocompass for heading, to determine absolute velocities. The ADCP/navigation/gyrocompass system was calibrated by covariability between currents and ship velocity (Kosro, 1985; Pollard and Read, 1989). A scale factor of ˜2% and a calibration error which varied linearly in time from 0.1-0.5° were detected and removed. Remaining calibration uncertainty implies an unknown bias of ˜0.02 ms^{-1} in absolute velocities. Raw reference layer velocities were low-pass filtered with a 20-min Blackman window (Firing *et al.*, 1995). Short-term inherent random errors for an ensemble are at most 0.02 ms^{-1}, and the estimated rms error in absolute reference layer velocity was 0.04 ms^{-1}.

Vertical sections of ADCP were contoured using a Barnes objective analysis (OA) scheme (eg. Daley, 1991) with successive horizontal(vertical) smoothing scales of 15(50), 10.6(35.4), and 7.5(25) km(m). We define the alongshore direction to be 330°T in the region south of Cape Mendocino and 0°T north of Cape Mendocino. For maps of ADCP vectors, component values and locations are 5 km spatial averages, and in cases where the cruise track overlays itself, measurements from different times are averaged together.

To derive streamfunction from the ADCP velocities, the divergent portion of the velocity field must be removed. First, the two components of velocity are gridded using a four-pass Barnes OA (Barnes, 1994). The initial smoothing length scale is 30 km, while the 4th pass one is 10 km. In the case of the Cape Blanco study (Figure VI.7), with its better spatial resolution, we used an initial scale of 15 km. We determine streamfunction over this gridded velocity field

using the version III method of Hawkins and Rosenthal (1965), introduced to the oceanographic community by Carter and Robinson (1987). A Poisson equation for the velocity potential, forced by the observed field of divergence (calculated for each grid box), is solved with a boundary condition of zero on all sides. The resulting velocity potential is then used to add a correction to the boundary conditions for the Poisson equation for the streamfunction, forced by the relative vorticity field. This approach has the effect of maximizing the amount of kinetic energy in the resulting streamfunction field. We use the MUDPACK (Adams, 1989) routine to solve the Poisson equations, subject to the condition of no normal flow into the coast. Attempting to use the observed velocity field directly as a boundary condition for the streamfunction calculation, the simplest approach (eg. Pollard and Regier, 1992; Allen and Smeed, 1996), implicitly assumes that the observed field along the boundary is nondivergent, which may not be true given measurement noise. Divergenceless vectors are derived from the gridded streamfunction and then interpolated back to their original locations using improved Akima bivariate interpolation (Akima, 1996).

VI.4 Results

The full set of 105 alongshore velocity sections from the NMFS survey are available for viewing in an on-line data report (Pierce, 1997b). Here we present a representative sample of 16 sections (Figure VI.2). As expected during the summer upwelling season, surface equatorward flow is frequently present. Significant surface-intensified equatorward jets associated with upwelling can be seen at 48.3°N, 42.97°N, 42.14°N, and 40.14°. Consistent with historical observations and satellite imagery (Smith, 1995), the upwelling jets to the north of 42.8°N (Cape Blanco, Oregon) appear to be confined inshore of the continental shelf break. In sections to the south of 42.8°N, the upwelling flows are found seaward of the shelf break. The

separation which occurs as an upwelling jet passes through this region can be seen by comparing the 42.97°N and 42.14°N sections. Observation of the details of this separation process was the motivation for the Cape Blanco study (Figure VI.7; Barth *et al.* (1998)). Outside of this region, the absence of many cross-shore hydrographic observations to complement the NMFS ADCP makes further interpretation of the surface flows difficult. In this paper we focus on the subsurface poleward flow.

The ubiquity of poleward flow throughout the 5400 km of cross-shore trackline is striking. Individual sections show complex poleward current patterns (Figure VI.2). Barotropic tidal currents, baroclinic tidal currents, and inertial oscillations are probably all present in any particular section, a 0.05−0.10 ms^{-1} contribution (Torgrimson and Hickey, 1979) which confuses the view of the subtidal signal.

As one method of summarizing this large data set, we consider a subsurface depth-averaged layer (Figure VI.1). The upper limit of this layer is an estimated depth of the $\sigma_\theta = 26.4$ surface, and the lower limit is at 325 m, the typical range of good ADCP data. We determine the depth of the $\sigma_\theta = 26.4$ level using selected NMFS CTDs, and it varies from 120−161 m with a mean of 138 m (Figure 8a contours). We chose this layer definition as a reasonable one to focus our attention on the subsurface poleward undercurrent. The definition is particularly useful in the southern California bight region, to separate the undercurrent signal from a surface-intensified poleward flow which blends with it (eg. 34.12°N Figure VI.2), sometimes called the Southern California countercurrent (Hickey, 1979).

Depth-averaged poleward flow within this subsurface layer appears as black shading in Figure VI.1. In 96 out of 105 sections, maximum poleward layer velocity is at least 0.05 ms^{-1} over a 5 km width. The mean of these core layer velocities seen at each section is 0.17±0.01 ms^{-1}.

VI.4.1 Mean structure

One approach to the problem of separating out the undercurrent signal from other processes is to form averages. The effects of tides, inertial oscillations, and other phenomenon will decrease as sections are averaged. We have sufficient realizations and the undercurrent core is stable enough to render meaningful such a meridional mean section (Figure VI.3a). The entire NMFS ADCP data set (including connecting legs between transects) is regridded (using 5 km grid spacing) onto an off-shelf-break coordinate system, then contoured (Figure VI.3a). Standard errors (assuming $N = 105$ independent points) are figured for each grid point, and these are at most about 0.02 ms^{-1}. Values less than the standard error are omitted from the plot. The mean cross-shelf section reveals a poleward undercurrent core > 0.10 ms^{-1} with thickness 175−320 m, 20−25 km off the shelf break (Figure VI.3a). The mean poleward volume transport below $\sigma_\theta = 26.4$ is $0.9 \pm 0.2 \times 10^6 m^3 s^{-1}$.

In addition to this evidence of the alongshore continuity of the undercurrent, recent results from an array of moorings provide evidence of its continuity in time: the Eastern Boundary Current moored array at 38.5°N measured currents for 22 months at 5 cross-shore locations extending from the inner slope (410 m) to the abyssal plane (3650 m), at 14 km spacing (Kosro *et al.*, 1994). Mean poleward flow was observed at depths > 100 m, with the maximum poleward flow at the innermost mooring at about 175 m (Figure VI.3b). Using the 3 slope moorings and integrating from about 100−600 m (the shaded region of Figure VI.3b) yields a poleward transport of $0.8 \times 10^6 m^3 s^{-1}$, consistent with the Figure VI.3a spatial mean transport of $0.9 \pm 0.2 \times 10^6 m^3 s^{-1}$. The two views of the undercurrent are also similar in that the > 0.10 ms^{-1} core is centered roughly above the 800 m isobath in both cases. The spatial mean has maximum

poleward flow away from the slope (Figure VI.3a), while the moored array shows maximum flow hugging the slope (Figure VI.3b), but this difference is probably due to the coarser cross-slope resolution of the moored array.

From a single current meter at 350 m depth located over the 800 m isobath off Pt. Sur, a relatively long (6 year) time series is available (Collins *et al.*, 1996a). Again, the 0.08 ms^{-1} poleward flow from the moored instrument at 350 m agrees well with our 0.09 ms^{-1} mean at 325 m.

VI.4.2 Latitudinal trends

Both the subsurface poleward maximum layer velocities and the layer transports for individual sections show significant scatter (Figure VI.4). This is not surprising, given the presence of unresolved tidal, inertial, and other contaminants. We initially determined a statistically significant large-scale trend with latitude in both characteristics, by classical least-squares fits (dashed lines of Figure VI.4), as in Pierce *et al.* (1996). Both the core velocities and the transports decrease moving poleward.

Although these fits are significant, they are not necessarily the appropriate model in this case. We noticed first by eye, particularly in the transport, a region 43−47°N with reduced values. We then experimented with the variable block averaging (VBA) filter of, Howell (1995) a type of adaptive filter specifically designed to identify sharp boundaries in geophysical data. The VBA algorithm uses information obtained by applying the Haar transform (a primitive wavelet) on a fixed scale and at all possible positions within the data record. The solution is the one with the greatest skill, among all possible solutions which could be constructed using any number of blocks of size $n = 18$ or greater.

The VBA confirms a transition located just north of Cape Blanco, in both core velocity and transport. The location of this transition is consistent with the location of the equatorward surface jet separation in the Cape Blanco region (Barth *et al.*, 1998). Anticipating the results of the next section as seen in Figure VI.7, and discussed in detail in, (Barth *et al.*, 1998) a separating coastal jet can strengthen and deepen to the point where it interacts significantly with the poleward undercurrent. During the NMFS survey three weeks prior to the intensive Cape Blanco study, the poleward flow appears to bifurcate off of Coos Bay (Figure VI.6), perhaps as a result of a small upwelling jet above (43.47°N Figure VI.2). With the aid of the VBA method, however, we do know that to the north of 47°N, core velocity and transport are similar to what they were to the south of Cape Blanco. Excluding 43−47°N, we see only a small decrease in the core velocity and transport of about 1% per degree of latitude.

The characteristic width of the undercurrent (defined as the width at half-maximum velocity) and its change with latitude are revealed by forming three mean sections (Figure VI.5). Using two 5° latitudinal bands to the south of Cape Blanco and one 4° band to the north, a narrowing of the undercurrent to poleward is evident. Consistent with the undercurrent hugging the slope, the core moves closer to the slope as it narrows. The first-baroclinic Rossby radii of deformation for these latitude bands, as calculated by Chelton *et al.* (1998) from climatological 1° gridded hydrographic data, are 24.3, 21.8, and 15.5 km (Figure VI.5, horizontal lines). The widths of the poleward flow are consistent with the Rossby radii, which has also been noted in the case of the Peru undercurrent (Huyer, 1980). The change in width is not connected with a change in bottom slope, which does not change systematically with latitude.

VI.5 Cape Mendocino to Cape Blanco

We focus now on the Cape Mendocino to Cape Blanco region (Figure VI.6a). We choose this area to apply our method of deriving streamfunction from the ADCP data. This area is of particular interest since Cape Blanco appears to be the northernmost point where a surface equatorward jet separates from the coast. (Barth *et al.*, 1998) It is also a region where the NMFS transects fortunately extended further offshore than usual (Figure VI.1), beyond the 2000 m isobath, allowing us to resolve some of the flow field along the offshore edge of the undercurrent.

The original 5 km NMFS ADCP vectors for the subsurface layer (below $\sigma_\theta = 26.4$ down to 325 m) clearly show poleward flow, but the presence of other oceanic phenomena is also obvious (Figure VI.6a). The Barnes OA smoothing and the enforcement of nondivergence reduces the aliasing effects of tidal and inertial signals, retaining the poleward undercurrent (Figure VI.6b). The streamfunction plotted underneath has contour intervals corresponding to $0.1 \times 10^6 \mathrm{m}^3\mathrm{s}^{-1}$ in transport.

At least $0.2 \times 10^6 \mathrm{m}^3\mathrm{s}^{-1}$ of the transport unambiguously transits the 440 km length of our region, entering close to the inshore end of our southernmost transect and exiting close to the offshore end of the northernmost one. Additional transport is probably continuous throughout the region, but not quite resolved by our tracklines. Although a portion of the flow is continuous, we also see meandering and eddy formation. At 41°N, for example, part of the undercurrent is turning offshore, and this appears to be part of an anticyclonic eddy which is just about to break away. Just to the north of St. George Reef (42°N) is a large westward meander, which might be an early stage an eddy formation process. At 43.5°N off of Coos Bay, the veering offshore of $0.3 \times 10^6 \mathrm{m}^3\mathrm{s}^{-1}$ is consistent with the general decrease of transport in the 43.6−47°N region seen in Figure VI.4.

This view of the undercurrent, as a combination of some continuous flow inshore and another portion offshore prone to instabilities and anticylconic eddy formation, is consistent with recent Lagrangian measurements using subsurface RAFOS drifters (Collins *et al.*, 1996b; Garfield *et al.*, 1998). Both their floats #5 and #19 experience an acceleration and a veering offshore in the vicinity of Cape Mendocino, followed by a deceleration and gradual return onshore to the north, similar to our streamlines. Float #19 then drifts westward to the north of Cape Mendocino in similar fashion to the flow we see at 41°N. Float #5 traces a path through most of the region quite similar to our continuous streamlines, remaining in the undercurrent hugging the coast until just south of St. George Reef. At this point it heads offshore and gets caught in an anticyclonic eddy of about 35 km diameter, centered at about 125.2°W, 42.3°N. The meander which we see just north of St. George Reef could easily be a different stage of a process leading to such an eddy. Huyer *et al.* (1998) in the Eastern Boundary Current experiment also describe offshore subsurface anticyclonic lenses of relatively spicy (warm and salty) water mass which were presumed to form from the undercurrent in this manner and then drift to the west.

The deceleration to the north of Cape Mendocino is also evident from moored data. The two bold arrows at 39.6°N and 40.85°N in Figure VI.6b represent 150-300 m, mean currents from moorings Feb-Oct 1989 at the 400 m isobath. (Largier *et al.*, 1993) The speeds of 0.13 ms^{-1} to the south of the Cape and 0.05 ms^{-1} to the north are quite consistent with our measurements.

About three weeks after the large-scale survey (17-27 August 1995), an intensive Sea-Soar/ADCP survey of the Cape Blanco region took place (Figure VI.7a; Barth *et al.* (1998)). Again there appears to be about $0.2 \times 10^6 m^3 s^{-1}$ which is continuous poleward through the region (Figure VI.7b). A significant difference, however, is that a large portion of the undercurrent which enters from the south turns offshore. This is due to interaction with a strong equatorward

upwelling jet which separates from the coast off Cape Blanco, strengthens, and deepens to the point where it is interacting with the top of the poleward undercurrent. Barth *et al.* (1998) examine this interaction in detail. Relatively spicy undercurrent water can be seen interacting with and becoming part of the equatorward surface jet (their Figure VI.9). Three weeks previously (the NMFS survey passed through the region 25-30 July 1995), a smaller separated upwelling jet existed (Figure VI.2, 42.14°N), but this did not interact significantly with the undercurrent. The interaction with a strong separating surface jet above is another mechanism for a portion of the undercurrent to be torn away from the slope.

VI.6 Alongslope hydrography

As part of the NMFS survey, CTD casts were made at two or three locations along every second or third transect, down to depths of about 500 m. We selected the 31 stations out of the total of 65 which were over the slope (bottom depths 245−1830 m) to characterize the meridional water mass properties of the undercurrent. The core of spicy water at 100-250 m at the southern end of the survey spreads to poleward and is still detectable as a spiciness maximum in the vertical at the northern end of the survey, at 150-225 m depth (Figure VI.8a). Several examples of this type of indirect evidence for poleward undercurrent flow can be found in Neshyba *et al.* (1989).

The Cape Blanco study made a cross-slope CTD section at 43.2°N, the FM line (Figure VI.9a). Here the down-warped isopycnals below $\sigma_\theta = 26.4$ close to the slope indicate the presence of poleward geostrophic flow, and the spiciness maximum confirms the southern source of this undercurrent flow. Our choice of the $\sigma_\theta = 26.4$ surface as the upper boundary for the poleward undercurrent layer was guided by inspection of sections such as this.

Also shown on Figure VI.8a (small triangles) is the depth of the center of mass of poleward flow from ADCP. This is calculated as $z_{cm} = \sum vz / \sum v$ over the subsurface layer, where v is a raw poleward ADCP velocity and z is the depth of that measurement, providing a good indication of the core undercurrent depth. We note that z_{cm} ranges from 150−250 m, consistent with historical estimates of undercurrent depth (Neshyba *et al.*, 1989). In Pierce *et al.* (1996), we noted a slight poleward deepening of z_{cm}, but in that case we included poleward flow shallower than the $\sigma_\theta = 26.4$ level. In particular, the southern California bight region has significant poleward flow shallower than 26.4, sometimes called the Southern California countercurrent, which led to the conclusion of poleward deepening. Excluding this flow which is probably a different dynamical phenomenon, z_{cm} has no apparent trend with latitude (Figure VI.8a). Given the expected poleward shallowing of isopycnals, we note a general trend of the undercurrent core from σ_θ ~26.6 water at 35°N to σ_θ ~26.7 at 50°N. This is consistent with an undercurrent which mixes with slightly denser water downslope and offshore.

Isopycnic potential vorticity defined as $q = \rho^{-1} f \partial\rho/\partial z$, where f is the Coriolis parameter, calculated from hydrographic data in the manner of Talley (1988), can be a useful tracer of oceanic circulation. We calculate q using $\Delta\rho$ increments of 0.05 (Figures VI.8b and VI.9b). Shallower than the $\sigma_\theta = 26.3$ level, we note strong meridional variability in q (Figure VI.8c). At the $\sigma_\theta = 26.6$ level and deeper, the variance of q drops dramatically close to zero, and we note a broad region of reduced q variability centered about $q = 1.5 \times 10^{-12} \mathrm{cm}^{-1}\mathrm{s}^{-1}$. This level of q is at $\sigma_\theta = 26.6$ at the southern end and $\sigma_\theta = 26.7$ at the northern end, consistent with z_{cm} as well as the spreading core of spiciness (Figure VI.8a). Thus q appears to be a good tracer for the poleward undercurrent flow. In our cross-slope section as well (Figure VI.9b), we see that the poleward undercurrent flow coincides with the broad region of $q = 1.5 \times 10^{-12} \mathrm{cm}^{-1}\mathrm{s}^{-1}$ between 26.6−26.7.

This should not be surprising, since if we believe some part of the undercurrent to be continuous over this great a range of latitude, it must have some mechanism for conserving its potential vorticity in the face of the significant change in planetary vorticity f. The way the undercurrent conserves q is by a slight thickening, a poleward increase in Δz between isopycnals, to counteract increasing f. Although we have neglected the effects of relative vorticity, we expect this to be a possibly important term in the undercurrent only in a local sense (thus perhaps explaining the small undulations in the $q = 1.5$ contour), not affecting the utility of q as a tracer of undercurrent flow.

VI.7 Summary

From this extensive set of NMFS ADCP data, with supporting evidence from the intensive Cape Blanco study, an improved view of the poleward undercurrent emerges. The undercurrent is present along almost the entire mid-latitude eastern boundary of the North Pacific, with mean core velocity of 0.17 ms^{-1}, core depth 150−250 m, location 20−25 km off the shelf break, width of about a Rossby radius, and transport down to 325 m of $0.9 \pm 0.2 \times 10^6 m^3 s^{-1}$. ADCP streamfunction maps derived from velocity observations between Cape Blanco, Oregon and Cape Mendocino, California show some continuity of the undercurrent over this 440 km long region. In other portions of the flow, undercurrent water appears to leave the slope, thus breaking continuity on scales greater than about 300 km, in the form of anticyclonic eddies or as a portion of a separated equatorward jet in the vicinity of Cape Blanco. Analysis of alongshore hydrographic data provides additional evidence of continuity, particularly at levels below $\sigma_\theta = 26.6-26.7$. Potential vorticity in the range $1-2 \times 10^{-12} cm^{-1} s^{-1}$ appears to be a good tracer of the poleward flow.

VI.8 Acknowledgments

This work was supported by the Office of Naval Research grants N00014-9610039, -9810026, and -92J1357, with additional support from National Science Foundation grant OCE-9314370.

Fig. VI.1 ADCP transects across the shelf break during the NMFS Pacific whiting survey, July-August 1995. Depth-averaged subsurface alongshore flow between $\sigma_\theta = 26.4$ (about 140 m) and 325 m is plotted normal to the ship track, with poleward flow shaded. The 200 m isobath is shown.

Fig. VI.2 Selected ADCP vertical sections of alongshore flow (cm/s). Poleward flow is shaded.

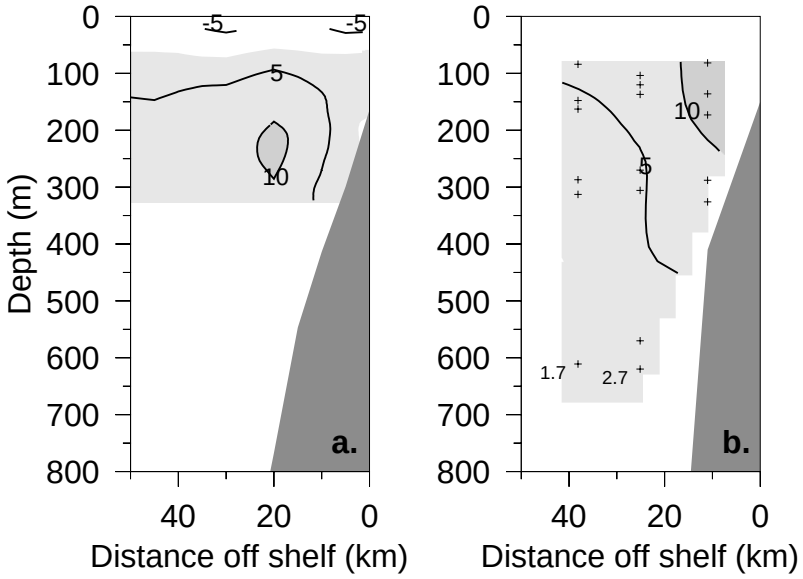

Fig. VI.3 (a) Spatial mean section of alongshore flow using all NMFS ADCP data, after transformation into an off-shelf coordinate system, using distance from the 150 m isobath. (b) 22 month temporal mean section of alongshore flow from the three innermost moorings of the Eastern Boundary Current moored slope array at 38.5°N.

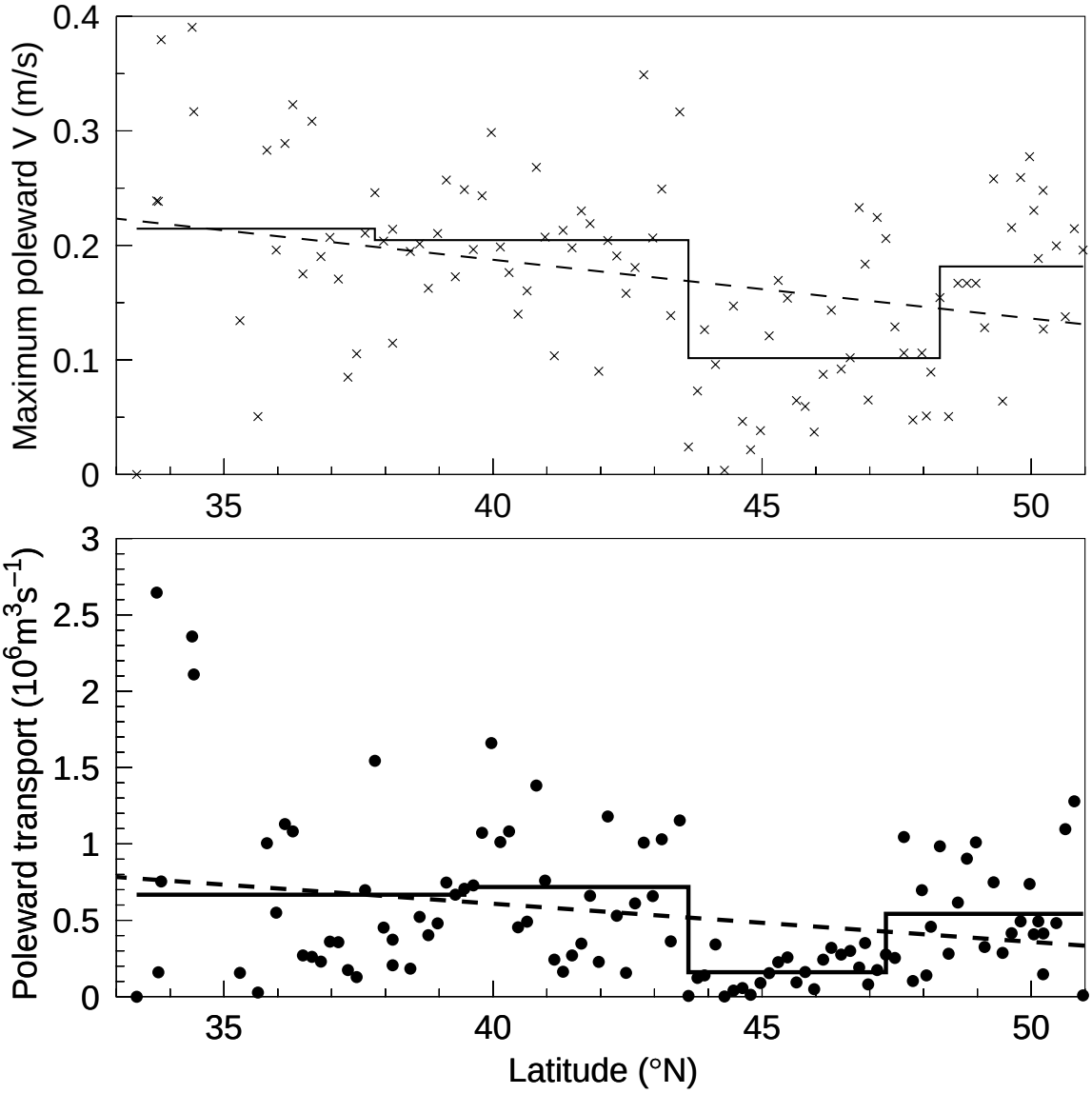

Fig. VI.4 Maximum poleward *V* (x) and the total subsurface layer transport (•), for each NMFS ADCP section. Light and bold solid lines show variable block averages for the maximum *V* and transport respectively. Light and bold dashed lines are least squares fits.

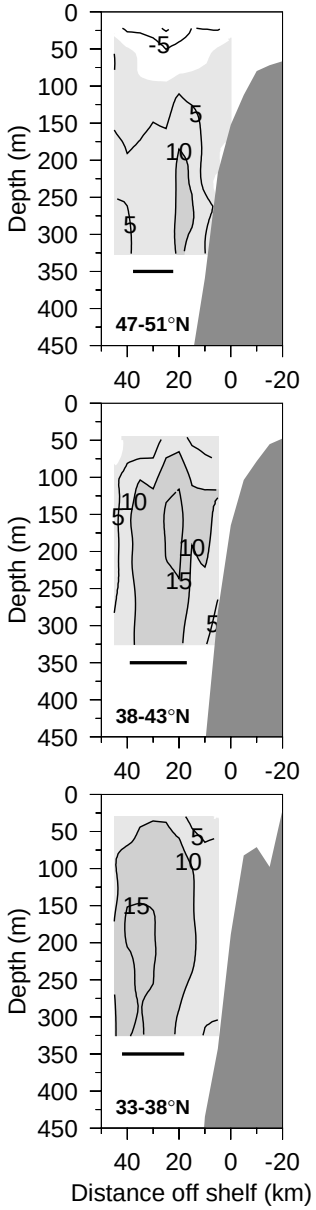

Fig. VI.5 Spatial mean sections for three different latitudinal bands. Values less than the standard error of the mean are blanked out. The horizontal line just below each section indicates the first baroclinic Rossby radius of deformation length, calculated from climatology within the same latitudinal band (from Chelton *et al.*, 1998).

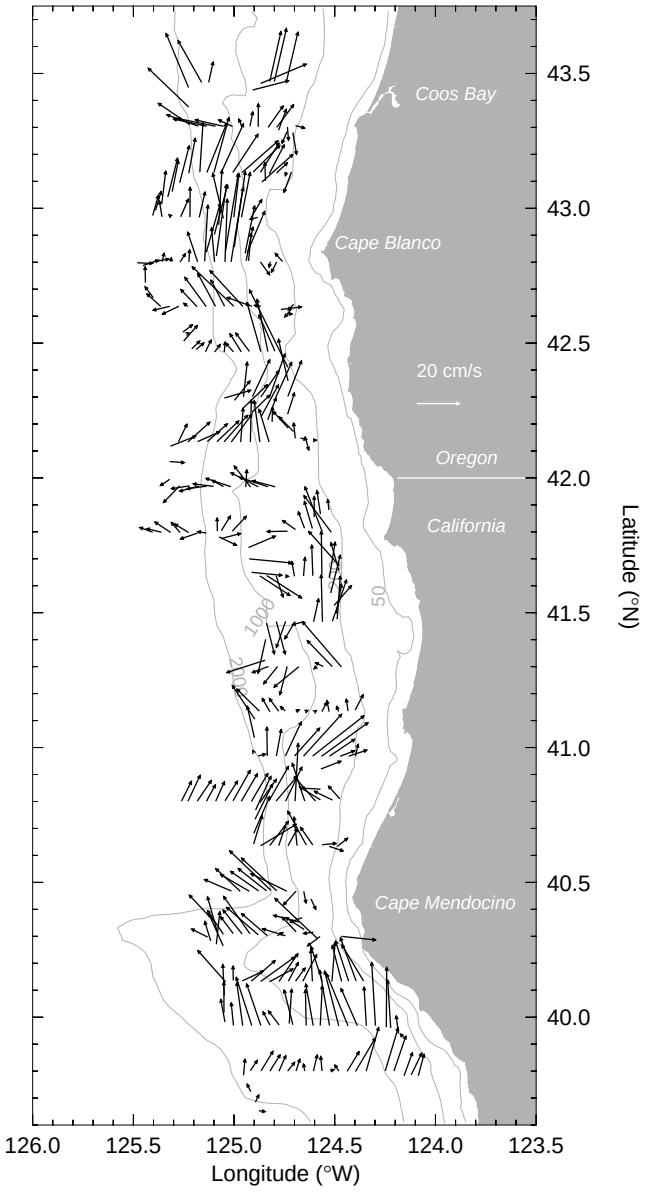

Fig. VI.6a Observed ADCP velocity vectors (depth-averaged below σ_θ = 26.4) from the NMFS survey, obtained 21−29 July 1995.

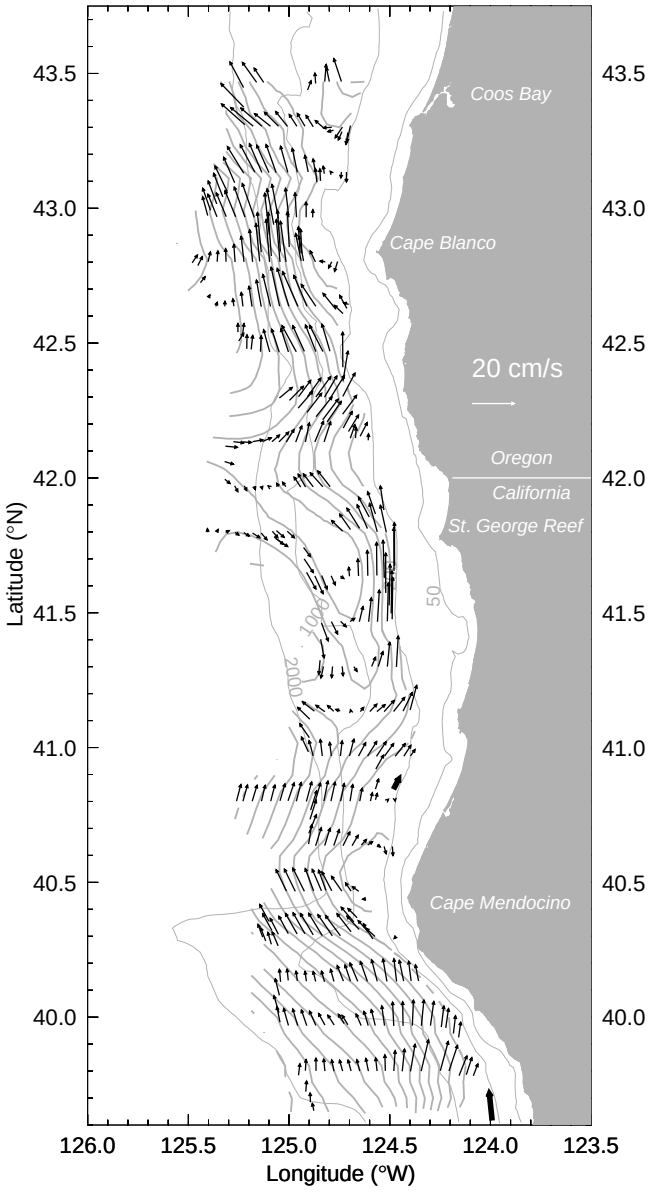

Fig. VI.6b Divergenceless ADCP velocity vectors for the same subsurface layer. The gray shade lines underneath are the corresponding transport streamfunction contours, with a 0.1 $\times 10^6 m^3 s^{-1}$ contour interval. The two bold arrows represent 150−300 m mean vectors from moorings (Largier *et al.*, 1993).

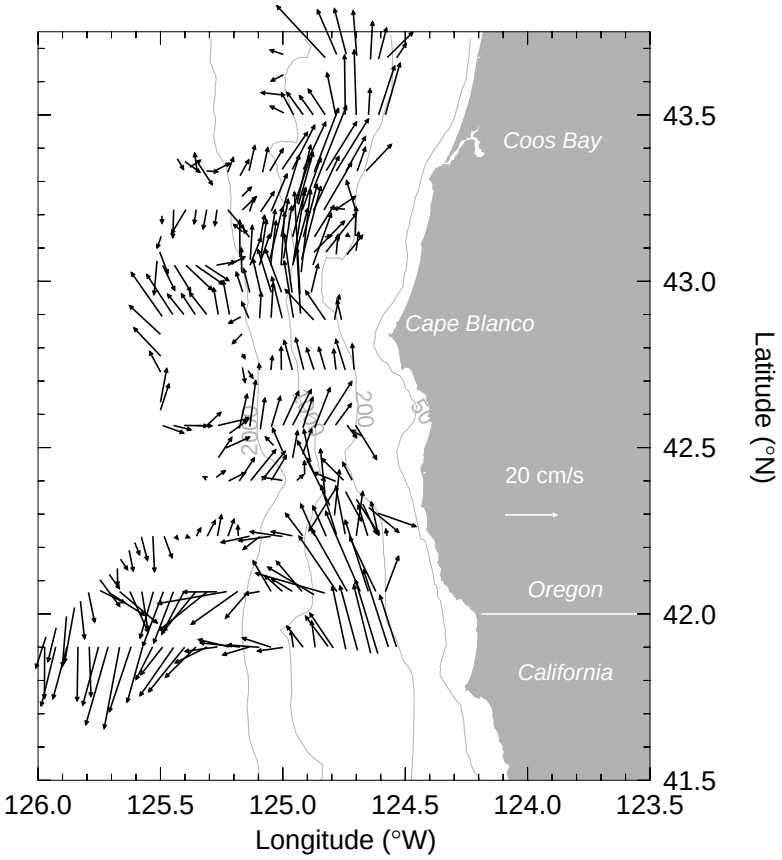

Fig. VI.7a Observed ADCP velocity vectors (depth-averaged below $\sigma_\theta = 26.4$) from the Coastal Jet Separation 17−27 August 1995 cruise.

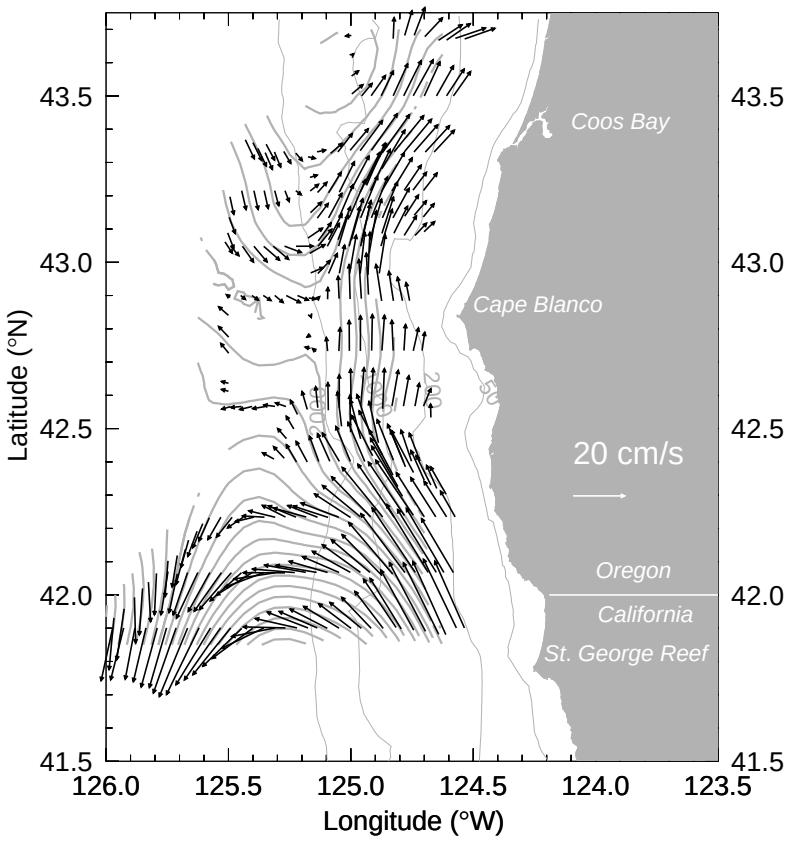

Fig. VI.7b Divergenceless ADCP velocity vectors for the same subsurface layer. The gray shade lines underneath are the corresponding transport streamfunction contours, with a $0.1 \times 10^6 \mathrm{m}^3\mathrm{s}^{-1}$ contour interval.

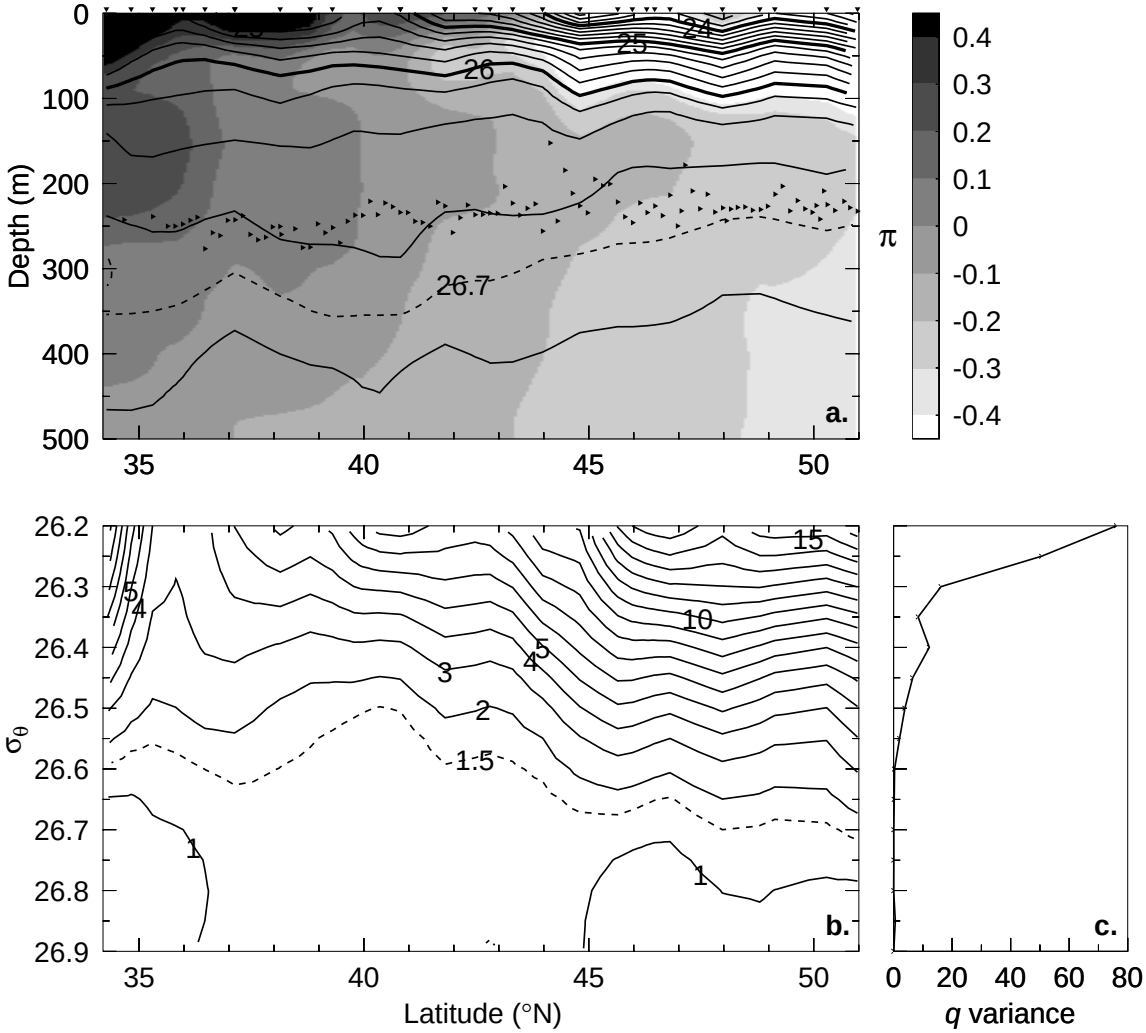

Fig. VI.8 (a) Vertical along-slope section using NMFS CTDs (station locations indicated at top). Contours are σ_θ, gray shade is spiciness π. The small triangles indicate the depth of the center of mass of poleward flow for each NMFS ADCP section. (b) Isopycnic potential vorticity $q = \rho^{-1} f \partial\rho/\partial z$ (10^{-12}cm^{-1}s^{-1}) at σ_θ levels, calculated from the CTD data. (c) Variance of q over the whole latitudinal range, for each σ_θ level.

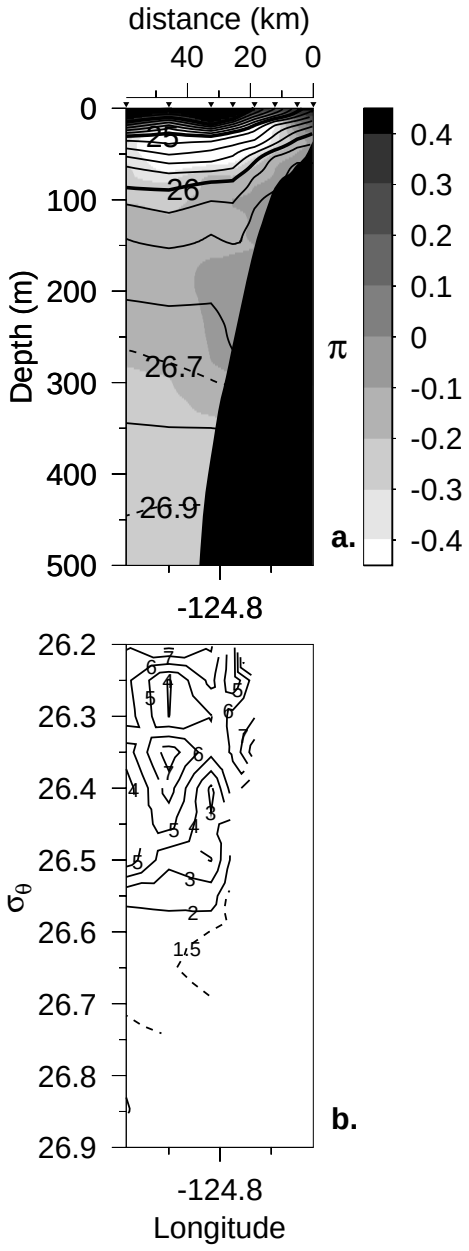

Fig. VI.9 (a) Cross-slope section at 43.2°N (the FM line) during the Cape Blanco study, CTD station locations indicated at top. Contours are σ_θ, gray shade is spiciness π. (b) Isopycnic potential vorticity $q = \rho^{-1} f \partial\rho/\partial z$ (10^{-12}cm^{-1}s^{-1}) at σ_θ levels, calculated from the CTD data.

VI.8 References

Adams, J., 1989: MUDPACK: Multi-grid Fortran software for the efficient solution of linear elliptic partial differential equations. *Applied Math. Comp.*, **34**, 113-146.

Akima, H., 1996: Rectangular-grid-data surface fitting that has the accuracy of a bicubic polynomial. *ACM Trans. Math. Software*, **22**, 357-361.

Allen, J. T. and D. A. Smeed, 1996: Potential vorticity and vertical velocity at the Iceland-Faeroes front. *J. Phys. Oceanogr.*, **26**, 2611-2634.

Barnes, S. L., 1994: Applications of the Barnes objective analysis scheme, part III: tuning for minimum error. *J. Atmos. Oceanic Tech.*, **11**, 1459-1479.

Barth, J. A., S. D. Pierce, and R. L. Smith, 1998: A separating coastal upwelling jet at Cape Blanco, Oregon and its connection to the California Current system. *Deep-Sea Res.*. [in press.]

Barth, J. A. and R. L. Smith, 1998: Separation of a coastal upwelling jet at Cape Blanco, Oregon, USA. *South Afr. J. Mar. Sci.*. [in press.]

Carter, E. F. and A. R. Robinson, 1987: Analysis models for the estimation of oceanic fields. *J. Atmos. Oceanic Technol.*, **4**, 49-74.

Chelton, D. B., R. A. deSzoeke, and M. G. Schlax, 1998: Geographical variability of the first baroclinic Rossby radius of deformation. *J. Phys. Oceanogr.*, **28**, 433-460.

Collins, C. A., N. Garfield, R. G. Paquette, and E. Carter, 1996b: Lagrangian measurement of subsurface poleward flow between 38N and 43N along the west coast of the United States during summer, 1993. *Geophys. Res. Letters*, **23**, 2461-2464.

Collins, C. A., R. G. Paquette, and S. R. Ramp, 1996a: Annual variability of ocean currents at 350-m depth over the continental slope off of Pt. Sur, California. *CalCOFI Reports*, **37**, 257-263.

Daley, R., 1991: *Atmospheric data analysis*, Cambridge.

Firing, E., J. Ranada, and P. Caldwell, *Processing ADCP data with the CODAS software system version 3.1, user's manual*, 1995. Manual and software available electronically at ftp://noio.soest.hawaii.edu/pub/codas3

Flament, P., 1986: Finestructure and subduction associated with upwelling filaments, UCSD Ph.D. thesis, University of California, La Jolla, CA.

Garfield, N., C. A. Collins, R. G. Paquette, and A. Carter, 1998: Lagrangian exploration of the California undercurrent, 1992-1995. *J. Phys. Oceanogr.*. [in press.]

Hawkins, H. F. and S. L. Rosenthal, 1965: On the computation of streamfunctions from the wind field. *Mon. Wea. Rev.*, **93**, 245-252.

Hickey, B. M., 1979: The California Current system - hypotheses and facts. *Prog. Oceanog.*, **8**, 191-279.

Howell, J. F., 1995: Identifying sudden changes in data. *Mon. Wea. Rev.*, **123**, 1207-1212.

Huyer, A., 1980: The offshore structure and subsurface expression of sea level variations off Peru, 1976-1977. *J. Phys. Oceanogr.*, **10**, 1755-1768.

Huyer, A., J. A. Barth, P. M. Kosro, R. K. Shearman, and R. L. Smith, 1998: Upper-ocean water mass characteristics of the California current, summer 1993. *Deep-Sea Res.*. [in press.]

Kosro, P. M., 1985: Shipboard acoustic current profiling during the Coastal Ocean Dynamics Experiment., UCSD Ph.D. thesis, SIO Ref. No. 85-8, University of California, La Jolla, Ca..

Kosro, P. M., S. R. Ramp, and R. L. Smith, 1994: Moored current measurements over the continental slope in EBC: a first look. *EOS Trans. AGU*, **75(44)**, p. 345. [abstract.]

Largier, J. L., B. A. Magnell, and C. D. Winant, 1993: Subtidal circulation over the northern California shelf. *J. Geophys. Res.*, **98**, 18147-18179.

Neshyba, S. J., C. N. K. Mooers, R. L. Smith, and R. T. Barber (eds), 1989: in *Poleward flows along eastern ocean boundaries*, Springer-Verlag, New York.

Pierce, S. D., R. L. Smith, and P. M. Kosro, 1996: Observations of the poleward undercurrent along the eastern boundary of the mid-latitude Pacific. *EOS Trans. AGU*, **77(46)**, p. F345. [abstract.]

Pierce, S. D., J. A. Barth, and R. L. Smith, 1997a: Acoustic doppler current profiler observations during the Coastal Jet Separation project on R/V *Wecoma*, 17−27 August 1995, Data Rep. 166, Ref. 97-4, p. 123 pp., Coll. of Oceanic and Atm. Sci., Oregon State Univ.

Pierce, S. D., 1997b: Observations of the poleward undercurrent along the eastern boundary of the mid-latitude Pacific, Data Rep., Coll. of Oceanic and Atm. Sci., Oregon State Univ. available on-line from http://diana.oce.orst.edu

Pollard, R. and J. Read, 1989: A method for calibrating ship mounted acoustic Doppler profilers and the limitations of gyro compasses. *J. Atmos. Oceanic Tech.*, **6**, 859-865.

Pollard, R. T. and L. A. Regier, 1992: Vorticity and vertical circulation at an ocean front. *J. Phys. Oceanogr.*, **22**, 609-625.

Smith, R. L., 1995: The physical processes of coastal upwelling systems, in *Upwelling in the ocean: modern processes and ancient records*, ed. C. P. Summerhayes, K.-C. Emeis, M. V. Angel, R. L. Smith, and B. Zeitzschel, 39-64, Wiley & Sons Ltd..

Talley, L. D., 1988: Potential vorticity distribution in the North Pacific. *J. Phys. Oceanogr.*, **18**, 89-106.

Tibby, R. B., 1941: The water masses off the west coast of North America. *J. Mar. Res.*, **4**, 112-121.

Torgrimson, G. M. and B. M. Hickey, 1979: Barotropic and baroclinic tides over the continental slope and shelf off Oregon. *J. Phys. Oceanogr.*, **9**, 945-961.

Warren, B. A., 1990: Book review of *Poleward flow along eastern ocean boundaries*. *Limn. Ocean.*, **35**, 1219-1220.

Wilson, C. D. and M. A. Guttormsen, 1997: Echo integration-trawl survey of Pacific Whiting, *Merluccius productus*, off the west coasts of the United States and Canada during July-September 1995, NOAA Tech. Memo NMFS-AFSC-74, NOAA-NMFS U.S. Dept. of Commerce.

Zedel, L. J. and J. A. Church, 1987: Real-time screening techniques for Doppler current profiler data. *J. Atmos. Oceanic Tech.*, **4**, 572-581.

VII. Summary

We sharpen our view of an eastern boundary current region during the upwelling season through the analysis of several data sets. We focus on providing an improved description of the mesoscale flow field off of northern California, observed during the Coastal Transition Zone (CTZ) experiment of 1988. First, we estimate tidal currents in the region by least-squares harmonic analysis of both shipboard acoustic Doppler current profiler (ADCP) and moored data. The tide is predominantly M_2 and varies from 1-4 cm/s across the region, consistent with previous tidal studies. Next, we use detided ADCP together with CTD data to infer absolute geostrophic velocities during each of the five surveys in July-August 1988. Referencing geostrophy with the ADCP reveals a stronger equatorward jet than previously reported; southward volume transport from 0-500 m through a 200 km onshore-offshore line is as high as 8.0 $\times 10^6 m^3 s^{-1}$, with a mean over the five surveys of $6.3 \pm 1.3 \times 10^6 m^3 s^{-1}$. Vertical velocities are O(10) m/d and regions of upward or downward flow tend to occur in patches of 20-30 km in diameter. The jet was about 50 km wide, with core velocities > 0.7 m/s. During a two-week period in July 1988, horizontal velocity shears were sufficient to shift the effective local inertial frequency 10% higher on the cold (inshore) side and 5% lower on the warm (offshore) side of the jet. Observed near-inertial currents have amplified energy in the region with lower effective inertial frequency, consistent with theoretical predictions. Next, the basic instability mechanism leading to a meandering CTZ jet is analyzed using a linear quasi-geostrophic model applied to observed snapshots of the jet. The jet is subject to both barotropic and baroclinic instability processes, and meander wavelengths of 260-265 km are the fastest growing. Growth periods of 7-11 days and along-jet phase speeds of 4-8 km/d are also predicted. Finally, the poleward undercurrent which was observed during the 1988 CTZ experiment is also investigated with a

series of shipboard ADCP sections collected from 33-51°N during July-August 1995. Subsurface poleward flow occurred in 91% of the sections, with a mean undercurrent core velocity of 17±1 cm/s and transport in a 140-325 m layer of $0.9\pm0.1\times10^{6}m^{3}s^{-1}$. One portion of the undercurrent flow is continuous over a 440 km length.

The five separate studies which comprise the thesis focus on different aspects of the mid-latitude north Pacific eastern boundary current system during the upwelling season, when winds blow alongshore toward the equator. Our results contribute to an increasing body of evidence that the classical view of an equatorward California Current which is quite broad (>1000 km) and weak (10 cm/s) is misleading (Huyer *et al.*, 1998). Although the classical view probably remains correct in a large-scale and annual mean sense, during the upwelling season the flow field is qualitatively different. Intense mesoscale equatorward-tending surface jets can form along the boundary between freshly upwelled near-shore and warmer offshore water. Nearly ubiquitous subsurface poleward flow close to the slope is another important feature in this revised view of eastern boundary current systems. Most studies contributing to the new paradigm have focused on the north Pacific example, since this is the best-observed, but these results are also relevant to the eastern boundary current systems off the west coast of South America, the coasts of northwest and southwest Africa, and the western edge of the Iberian peninsula.

Bibliography

Table of contents

Table of contents (continued)

Table of contents (continued)

List of figures

List of figures (continued)

List of figures (continued)

List of tables

Huyer, A., J. A. Barth, P. M. Kosro, R. K. Shearman, and R. L. Smith, 1998: Upper-ocean water mass characteristics of the California current, summer 1993. *Deep-Sea Res.*. [in press.]

Bibliography

Adams, J., 1989: MUDPACK: Multi-grid Fortran software for the efficient solution of linear elliptic partial differential equations. *Applied Math. Comp.*, **34**, 113-146.

Akima, H., 1996: Rectangular-grid-data surface fitting that has the accuracy of a bicubic polynomial. *ACM Trans. Math. Software*, **22**, 357-361.

Allen, J. S., L. J. Walstad, and P. A. Newberger, 1991: Dynamics of the coastal transition zone jet, 2. nonlinear finite amplitude behavior. *J. Geophys. Res.*, **96**, 14995-15016.

Allen, J. T. and D. A. Smeed, 1996: Potential vorticity and vertical velocity at the Iceland-Faeroes front. *J. Phys. Oceanogr.*, **26**, 2611-2634.

Bacon, S., 1994: Skill in an inversion solution: CONVEX-91 hydrographic results compared with ADCP measurements. *J. Atmos. Oceanic Technol.*, **11**, 1569-1591.

Barnes, S. L., 1994: Applications of the Barnes objective analysis scheme, part III: tuning for minimum error. *J. Atmos. Oceanic Tech.*, **11**, 1459-1479.

Barth, J. A., 1994: Short-wavelength instabilities on coastal jets and fronts. *J. Geophys. Res.*, **99**, 16095-16115.

Barth, J. A., S. D. Pierce, and R. L. Smith, 1998: A separating coastal upwelling jet at Cape Blanco, Oregon and its connection to the California Current system. *Deep-Sea Res.*. [in press.]

Barth, J. A. and R. L. Smith, 1998: Separation of a coastal upwelling jet at Cape Blanco, Oregon, USA. *South Afr. J. Mar. Sci.*. [in press.]

Battisti, D. S. and A. J. Clarke, 1982: A simple method for estimating barotropic tidal currents on continental margins with specific application to the M2 tide off the Atlantic and Pacific coasts of the United States. *J. Phys. Oceanogr.*, **12**, 8-16.

Beckmann, A., 1988: Vertical structure of midlatitude mesoscale instabilities. *J. Phys. Oceanogr.*, **18**, 1354-1371.

Bernstein, R. L., L. Breaker, and R. Whritner, 1977: California Current eddy formation: ship, air and satellite results. *Science*, **195**, 353-359.

Brink, K. H. and T. J. Cowles, 1991: The coastal transition zone program. *J. Geophys. Res.*, **96**, 14637-14647.

Candela, J., R. C. Beardsley, and R. Limeburner, 1992: Separation of tidal and subtidal currents in ship-mounted acoustic doppler current profiler observations. *J. Geophys. Res.*, **97**, 769-788.

Carter, E. F. and A. R. Robinson, 1987: Analysis models for the estimation of oceanic fields. *J. Atmos. Oceanic Technol.*, **4**, 49-74.

Chelton, D. B., R. A. deSzoeke, and M. G. Schlax, 1998: Geographical variability of the first baroclinic Rossby radius of deformation. *J. Phys. Oceanogr.*, **28**, 433-460.

Chereskin, T. K. and M. Trunnell, 1996: Correlation scales, objective mapping, and absolute geostrophic flow in the California current. *J. Geophys. Res.*, **101**, 22619-22629.

Collins, C. A., N. Garfield, R. G. Paquette, and E. Carter, 1996b: Lagrangian measurement of subsurface poleward flow between 38N and 43N along the west coast of the United States during summer, 1993. *Geophys. Res. Letters*, **23**, 2461-2464.

Collins, C. A., R. G. Paquette, and S. R. Ramp, 1996a: Annual variability of ocean currents at 350-m depth over the continental slope off of Pt. Sur, California. *CalCOFI Reports*, **37**, 257-263.

CTZ Group, 1988: The Coastal Transition Zone Program. *EOS, Trans. Am. Geophys. Union*, **69**, 698-699, 704, 707.

Cummins, P. F. and G. K. Vallis, 1994: Algorithm 732: solvers for self-adjoint elliptic problem in irregular two-dimensional domains. *ACM Trans. Math. Soft.*, **20**, 247-261.

Daley, R., 1991: *Atmospheric data analysis*, Cambridge.

Dewey, R. K., J. N. Moum, C. A. Paulson, D. R. Caldwell, and S. D. Pierce, 1991: *J. Geophys. Res.*, 14885-14907.

Firing, E., J. Ranada, and P. Caldwell, *Processing ADCP data with the CODAS software system version 3.1, user's manual*, 1995. Manual and software available electronically at ftp://noio.soest.hawaii.edu/pub/codas3

Flament, P., L. Armi, and L. Washburn, 1985: The evolving structure of an upwelling filament. *J. Geophys. Res.*, **90**, 11765-11778.

Flament, P., 1986: Finestructure and subduction associated with upwelling filaments, UCSD Ph.D. thesis, University of California, La Jolla, CA.

Fliegel, M. and A. A. Nowroozi, 1970: Tides and bottom currents off the coast of northern California. *Limnol. Oceanogr.*, **15**, 615-624.

Garfield, N., C. A. Collins, R. G. Paquette, and A. Carter, 1998: Lagrangian exploration of the California undercurrent, 1992-1995. *J. Phys. Oceanogr.*. [in press.]

Haidvogel, D. B. and W. R. Holland, 1978: The stability of ocean currents in eddy-resolving general circulation models. *J. Phys. Oceanogr.*, **8**, 393-413.

Haidvogel, D. B., A. Beckmann, and K. S. Hedstrom, 1991: Dynamical simulations of filament formation and evolution in the coastal transition zone. *J. Geophys. Res.*, **96**, 15017-15040.

Hart, J. E., 1974: On the Mixed Stability Problem for Quasi-geostrophic Ocean Currents. *J. Phys. Oceanogr.*, **4**, 349-356.

Hawkins, H. F. and S. L. Rosenthal, 1965: On the computation of streamfunctions from the wind field. *Mon. Wea. Rev.*, **93**, 245-252.

Heath, G. R., D. K. Rea, G. Ness, R. D. Pillsbury, T. M. Beasley, C. Lopez, and D. M. Talbert, 1984: Oceanographic studies supporting the assessment of deep-sea disposal of defueled decommissioned nuclear submarines. *Environ. Geol. Water Sci.*, **6**, 189-199.

Hickey, B. M., 1979: The California Current system - hypotheses and facts. *Prog. Oceanog.*, **8**, 191-279.

Hofmann, E. E., K. S. Hedstrom, J. R. Moisan, D. B. Haidvogel, and D. L. Mackas, 1991: Use of simulated drifter tracks to investigate general transport patterns and residence times in the coastal transition zone. *J. Geophys. Res.*, **96**, 15041-15052.

Holland, W. R. and D. B. Haidvogel, 1980: A parameter study of the mixed instability of idealized ocean currents. *Dyn. Atmos. Oceans*, **4**, 185-215.

Horn, W., 1960: Some recent approaches to tidal problems. *Int. Hydrogr. Rev.*, **38**, 28-105.

Howell, J. F., 1995: Identifying sudden changes in data. *Mon. Wea. Rev.*, **123**, 1207-1212.

Huyer, A., 1980: The offshore structure and subsurface expression of sea level variations off Peru, 1976-1977. *J. Phys. Oceanogr.*, **10**, 1755-1768.

Huyer, A., P. M. Kosro, J. Fleischbein, S. R. Ramp, T. Stanton, L. Washburn, F. P. Chavez, T. J. Cowles, S. D. Pierce, and R. L. Smith, 1991: Currents and water masses of the coastal transition zone off northern California, June to August 1988. *J. Geophys. Res.*, **96**, 14809-14831.

Huyer, A., J. A. Barth, P. M. Kosro, R. K. Shearman, and R. L. Smith, 1998: Upper-ocean water mass characteristics of the California current, summer 1993. *Deep-Sea Res.*. [in press.]

Ikeda, M. and W. J. Emery, 1984: Satellite observations and modeling of meanders in the California Current system off Oregon and northern California. *J. Phys. Oceanogr.*, **14**, 1434-1450.

Irish, J., W. Munk, and F. Snodgrass, 1971: M2 amphidrome in the northeast Pacific. *Geophys. Fluid. Dyn.*, **2**, 355-360.

Johns, W. E., 1988: One-dimensional baroclinically unstable waves on the Gulf Stream potential vorticity gradient near Cape Hatteras. *Dyn. Atmos. Oceans*, **11**, 323-350.

Kadko, D. C., L. Washburn, and B. Jones, 1991: Evidence of subduction within cold filaments of the northern California coastal transition zone. *J. Geophys. Res.*, **96**, 14909-14926.

Kaufman, L. C., 1975: The LZ algorithm to solve the generalized eigenvalue problem for complex matrices. *ACM Trans. Math. Software*, **1**, 271-281.

Killworth, P. D., 1980: On determination of absolute velocities and density gradients in the ocean from a single hydrographic section. *Deep-Sea Res.*, **27**, 901-929.

Koch, S. E., M. DesJardins, and P. J. Kocin, 1983: An interactive Barnes objective map anlaysis scheme for use with satellite and conventional data. *J. Climate Appl. Met.*, **22**, 1487-1503.

Kosro, P. M., 1985: Shipboard acoustic current profiling during the Coastal Ocean Dynamics Experiment., UCSD Ph.D. thesis, SIO Ref. No. 85-8, University of California, La Jolla, Ca..

Kosro, P. M. and A. Huyer, 1986: CTD and velocity surveys of seaward jets off northern California., July 1981 and 1982. *J. Geophys. Res.*, **91**, 7680-7690.

Kosro, P. M., A. Huyer, S. R. Ramp, R. L. Smith, F. P. Chavez, T. J. Cowles, M. R. Abbott, P. T. Strub, R. T. Barber, P. Jessen, and L. F. Small, 1991: The structure of the transition zone between coastal waters and the open ocean off northern California, winter and spring 1987. *J. Geophys. Res.*, **96**, 14707-14730.

Kosro, P. M., S. R. Ramp, and R. L. Smith, 1994: Moored current measurements over the continental slope in EBC: a first look. *EOS Trans. AGU*, **75(44)**, p. 345. [abstract.]

Kunze, E., 1985: Near-inertial wave propagation in geostrophic shear. *J. Phys. Oceanogr.*, **15**, 544-565.

Large, W. G. and S. Pond, 1981: Open ocean momentum flux measurements in moderate to strong winds. *J. Phys. Oceanogr.*, **11**, 324-336.

Largier, J. L., B. A. Magnell, and C. D. Winant, 1993: Subtidal circulation over the northern California shelf. *J. Geophys. Res.*, **98**, 18147-18179.

Leach, H., 1987: The diagnosis of synoptic-scale vertical motion in the seasonal thermocline. *Deep-Sea Res.*, **34**, 2005-2017.

Limeburner, R., (ed), 1985: Code-2: moored array and large-scale data report, WHOI Tech. Rep. 85-35, p. 234, Woods Hole Oceanographic Institution.

Magnell, B. A., C. D. Winant, N. A. Bray, C. L. Greengrove, J. F. Borchardt, J. M. Federiuk, C. E. Dorman, R. L. Bernstein, and J. Largier, 1991: Circulation on the northern California shelf and slope: final report of the northern California coastal circulation study, OCS Study MMS 91-0023, p. 543, Miner. Manage. Serv., U.S. Dept. of the Inter..

Munk, W., F. Snodgrass, and M. Wimbush, 1970: Tides offshore, transition from California coastal to deep-sea waters. *Geophys. Fluid Dyn.*, **1**, 161-235.

Neshyba, S. J., C. N. K. Mooers, R. L. Smith, and R. T. Barber (eds), 1989: in *Poleward flows along eastern ocean boundaries*, Springer-Verlag, New York.

Noble, M., L. K. Rosenfeld, R. L. Smith, J. V. Gardner, and R. C. Beardsley, 1987: Tidal currents seaward of the northern California continental shelf. *J. Geophys. Res.*, **92**, 1733-1744.

Parks, T. W. and C. S. Burrus, 1987: *Digital filter design*, Wiley, New York.

Pedlosky, J., 1987: *Geophysical fluid dynamics*, p. 710 pp., Springer-Verlag, New York.

Phillips, N. A., 1956: The general circulation of the atmosphere: a numerical experiment. *Q. J. R. Meteorol. Soc.*, **82**, 123-164.

Pierce, S. D., J. S. Allen, and L. J. Walstad, 1991: Dynamics of the coastal transition zone jet: 1. linear stability analysis. *J. Geophys. Res.*, **96**, 14979-14993.

Pierce, S. D., R. L. Smith, and P. M. Kosro, 1996: Observations of the poleward undercurrent along the eastern boundary of the mid-latitude Pacific. *EOS Trans. AGU*, **77(46)**, p. F345. [abstract.]

Pierce, S. D., J. A. Barth, and R. L. Smith, 1997a: Acoustic doppler current profiler observations during the Coastal Jet Separation project on R/V *Wecoma*, 17−27 August 1995, Data Rep. 166, Ref. 97-4, p. 123 pp., Coll. of Oceanic and Atm. Sci., Oregon State Univ.

Pierce, S. D., 1997b: Observations of the poleward undercurrent along the eastern boundary of the mid-latitude Pacific, Data Rep., Coll. of Oceanic and Atm. Sci., Oregon State Univ. available on-line from http://diana.oce.orst.edu

Pinardi, N. and A. R. Robinson, 1986: Quasigeostrophic energetics of open ocean regions. *Dyn. Atmos. Oceans*, **10**, 185-219.

Pollard, R. and J. Read, 1989: A method for calibrating ship mounted acoustic Doppler profilers and the limitations of gyro compasses. *J. Atmos. Oceanic Tech.*, **6**, 859-865.

Pollard, R. T. and L. A. Regier, 1992: Vorticity and vertical circulation at an ocean front. *J. Phys. Oceanogr.*, **22**, 609-625.

Press, W. H., S. A. Teukolsky, W. T. Vetterling, and B. P. Flannery, 1992: *Numerical Recipes, 2nd edition*, Cambridge, Cambridge.

Rienecker, M. M., C. N. K. Mooers, D. E. Hagan, and A. R. Robinson, 1985: A cool anomaly off northern California: an investigation using IR imagery and in situ data. *J. Geophys. Res.*, **90**, 4807-4818.

Rienecker, M. M. and C. N. K. Mooers, 1989: Mesoscale eddies, jets, and fronts off Point Arena, California, July 1986. *J. Geophys. Res.*, **94**, C9, 12555-12569.

Robinson, A. R. and J. C. McWilliams, 1974: The baroclinic instability of the open ocean. *J. Phys. Oceanogr.*, **4**, 281-294.

Rosenfeld, L. K. and R. C. Beardsley, 1987: Barotropic and semidiurnal tidal currents off northern California during the Coastal Ocean Dynamics Experiment (CODE). *J. Geophys. Res.*, 1721-1732.

Rosenfeld, L. K., 1987: Tidal Band Current Variability Over the Northern California Continental Shelf. *WHOI Tech. Report*, **87-11**.

Rudnick, D. L., 1996: Intensive surveys of the Azores front, 2. inferring the geostrophic and vertical velocity fields. *J. Geophys. Res.*, **101**, 16291-16303.

Shearman, R. K., J. A. Barth, and P. M. Kosro, 1998: Diagnosis of the three-dimensional circulation associated with mesoscale motion in the California current. *J. Phys. Oceanogr.*. [in press.]

Smith, R. L., G. Pittock, J. Fleischbein, and R. Still, 1986: Current measurements from moorings off northern California: September 1984 - July 1985, 121, p. 211, College of Oceanography - Oregon State University.

Smith, R. L., 1995: The physical processes of coastal upwelling systems, in *Upwelling in the ocean: modern processes and ancient records*, ed. C. P. Summerhayes, K.-C. Emeis, M. V. Angel, R. L. Smith, and B. Zeitzschel, 39-64, Wiley & Sons Ltd..

Song, R. T., 1971: A numerical study of the three-dimensional structure and energetics of unstable disturbances in zonal currents: part II. *J. Atmos. Sci.*, **28**, 565-586.

Strub, P. Ted, P. Michael Kosro, and Adriana Huyer, 1991: The nature of the cold filaments in the California current system. *J. Geophys. Res.*, **96**, 14743-14768.

Talley, L. D., 1988: Potential vorticity distribution in the North Pacific. *J. Phys. Oceanogr.*, **18**, 89-106.

Tibby, R. B., 1941: The water masses off the west coast of North America. *J. Mar. Res.*, **4**, 112-121.

Torgrimson, G. M. and B. M. Hickey, 1979: Barotropic and baroclinic tides over the continental slope and shelf off Oregon. *J. Phys. Oceanogr.*, **9**, 945-961.

Veronis, G., 1981: Dynamics of the large-scale ocean circulation, in *Evolution of physical oceanography*, ed. B. A. Warren and C. Wunsch, 140-183, M.I.T. Press, Cambridge MA.

Walstad, L. J., J. S. Allen, P. M. Kosro, and A. Huyer, 1991: Dynamics of the coastal transition zone jet through data assimilation studies. *J. Geophys. Res.*, **96**, 14959-14977.

Warren, B. A., 1990: Book review of *Poleward flow along eastern ocean boundaries*. *Limn. Ocean.*, **35**, 1219-1220.

Washburn, L., D. C. Kadko, B. H. Jones, T. Hayward, P. M. Kosro, T. P. Stanton, S. Ramp, and T. Cowles, 1991: Water mass subduction and the transport of phytoplankton in a coastal upwelling system. *J. Geophys. Res.*, **96**, 14927-14946.

Wilson, C. D. and M. A. Guttormsen, 1997: Echo integration-trawl survey of Pacific Whiting, *Merluccius productus*, off the west coasts of the United States and Canada during July-September 1995, NOAA Tech. Memo NMFS-AFSC-74, NOAA-NMFS U.S. Dept. of Commerce.

Wooster, W. S. and J. L. Reid, 1963: Eastern boundary currents, in *The Sea*, ed. M. N. Hill, **2**, 253-280, Interscience Publishers, New York.

Zedel, L. J. and J. A. Church, 1987: Real-time screening techniques for Doppler current profiler data. *J. Atmos. Oceanic Tech.*, **4**, 572-581.